Universität
Wuppertal

JÜLICH
FORSCHUNGSZENTRUM

Impact of different vertical transport representations on simulating processes in the tropical tropopause layer (TTL)

Dissertation

zur Erlangung des Grades

Doktor der Naturwissenschaften (Dr. rer. nat.)

vorgelegt der

Bergischen Universität

Wuppertal

Fachbereich C – Mathematik und Naturwissenschaften

von

Felix Plöger

Wuppertal 2010

Die Dissertation kann wie folgt zitiert werden:

Dissertation zur Erlangung des Grades Doktor der Naturwissenschaften (Dr. rer. nat.), vorgelegt der Bergischen Universität Wuppertal (Fachbereich C – Mathematik und Naturwissenschaften).

Referent: Prof. Dr. Martin Riese
Korreferent :   Prof. Dr. Michael Volk
Tag der Abgabe: 30. September 2010

Abstract

The chemical and dynamical processes in the tropical tropopause layer (TTL) control the amount of radiatively active species like water vapour and ozone in the stratosphere, and hence turn out to be crucial for atmospheric trends and climate change. Chemistry transport models and chemistry climate models are suitable tools to understand these processes. But model results are subject to uncertainties arising from the parametrization of model physics. In this thesis the sensitivity of model predictions to the choice of the vertical transport representation will be analysed.

Therefore, backtrajectories are calculated in the TTL, based on different diabatic and kinematic transport representations using ERA-Interim and operational ECMWF data. For diabatic transport on potential temperature levels, the vertical velocity is deduced from the ERA-Interim diabatic heat budget. For kinematic transport on pressure levels, the vertical wind is used as vertical velocity. It is found that all terms in the diabatic heat budget are necessary to cause transport from the troposphere to the stratosphere. In particular, clear-sky heating rates alone miss very important processes. Many characteristics of transport in the TTL turn out to depend very sensitively on the choice of the vertical transport representation. Timescales for tropical troposphere-to-stratosphere transport vary between one and three months, with respect to the chosen representation. Moreover, for diabatic transport ascent is found throughout the upper TTL, whereas for kinematic transport regions of mean subsidence occur, particularly above the maritime continent. To investigate the sensitivity of simulated trace gas distributions in the TTL to the transport representation, a conceptual approach is presented to predict water vapour and ozone concentrations from backtrajectories, based on instantaneous freeze-drying and photochemical ozone production. It turns out that ozone predictions and vertical dispersion of the trajectories are highly correlated, rendering ozone an interesting tracer for aspects of transport in the TTL where water vapour is not sensitive. Consequently, dispersion and mean upwelling have similar effects on ozone profles, with slower upwelling and larger dispersion both leading to higher ozone concentrations. Analyses of tropical upwelling based on mean transport characteristics (e.g., mean ascent rates) and model validation have to take into account this ambiguity. Predicted ozone concentrations for kinematic transport are robustly higher than for diabatic transport, due to larger trajectory dispersion caused by the larger inhomogeneity in the kinematic vertical velocity f eld. During the tropical SCOUT-O3 campaign, kinematic ozone predictions show an extreme high bias compared to in-situ observations.

The high sensitivity of many characteristics of transport to the choice of the transport representation, demonstrates the need to better constrain transport in the TTL. Consequently, estimates of exact numbers from models, e.g., for timescales of transport, are not reliable and only a range of values can be given. However, there are robust features of tropical transport, not depending on the transport representation, as for example, a signif cant impact of monsoon driven horizontal in-mixing from the extratropics on the composition of the TTL. In fact, the annual cycle of ozone above the tropical tropopause is attributed, at least in 'ECMWF-world', to in-mixing of ozone-rich extratropical air during summer.

Zusammenfassung

Chemische und dynamische Prozesse in der tropischen Tropopausenschicht (TTL) kontrollieren die stratosphärischen Konzentrationen strahlungswirksamer Spurengase, wie Wasserdampf und Ozon und wirken sich dadurch auf atmosphärische Trends und den Klimawandel aus. Zum Verständnis dieser Prozesse werden Chemietransport- und Klimamodelle eingesetzt. Die Modellresultate können jedoch von den gewählten Parametrisierungen der Modell-Physik abhängen. In der vorliegenden Arbeit wird die Empfndlichkeit der Modellresultate auf die Wahl der Darstellung des Vertikaltransports untersucht.

Dazu werden Rückwärtstrajektorien in der TTL gerechnet, basierend auf verschiedenen diabatischen und kinematischen Transport-Darstellungen. Für diabatischen Transport (isentrope Vertikalkoordinate) wird die Vertikalgeschwindigkeit aus dem ERA-Interim Wärmebudget berechnet. Für kinematischen Transport (Vertikalkoordinate Druck) ist die Vertikalgeschwindigkeit durch den Vertikalwind gegeben. Es stellt sich heraus, dass für tropischen Aufwärtstransport in die Stratosphäre alle Beiträge zum Wärmebudget (Strahlung mit Wolken, latente Wärme) notwendig sind. Des weiteren hängen viele Transportcharakteristiken stark von der Wahl der Transport-Darstellung ab. So variieren Zeitskalen für tropischen Transport aus der Tropo- in die Stratosphäre zwischen einem und drei Monaten, abhängig von der Wahl der Darstellung. Außerdem existieren für kinematischen Transport Regionen mittleren Absinkens in der oberen TTL, insbesondere über dem maritimen Kontinent, für diabatischen Transport nicht.

Zur Untersuchung der Empfndlichkeit simulierter Spurengasverteilungen auf die Transport-Darstellung, wird ein konzeptionelles Trajektorien-Modell zur Vorhersage von Wasserdampf- und Ozon in der TTL entwickelt, basierend auf instantanem Ausfrieren und photochemischer Ozonproduktion. Ein wichtiges Ergebnis ist die starke Korrelation zwischen vorhergesagter Ozonkonzentration und der vertikalen Streuung der Trajektorien. Deshalb reagiert Ozon auf viele Transportunsicherheiten empfndlicher als Wasserdampf. Einerseits können höhere Ozonkonzentrationen somit durch eine langsamere Aufstiegsgeschwindigkeit, andererseits durch stärkere Inhomogenitäten im Windfeld verursacht werden. Diese Zweideutigkeit muss in Ozon-basierten Analysen von Aufstiegsgeschwindigkeiten, wie auch bei der Validierung von Modelltransport berücksichtigt werden. Berechnete Ozonkonzentrationen sind generell höher für kinematischen als für diabatischen Transport, aufgrund stärkerer Trajektorien-Streuung im inhomogeneren kinematischen Windfeld. Für die tropische SCOUT-O3 Kampagne führt die kinematische Ozonvorhersage zu extrem hohen Konzentrationen im Vergleich zu Messungen.

Aufgrund der starken Sensitivität vieler Modellresultate auf die Wahl der Transport-Darstellung, ist es notwendig Transportunsicherheiten in der TTL zu reduzieren. Bis dahin müssen simulierte Transportgrössen, wie Aufstiegszeiten, mit einer transportbedingten Unsicherheit angegeben werden. Gewisse Transportmuster allerdings zeigen sich robust gegenüber Unsicherheiten in der Transport-Darstellung, wie ein signifkanter Einfuss Monsun-bedingter horizontaler Einmischung auf die Zusammensetzung der TTL. Zumindest in der 'ECMWF-Welt' wird der Ozon-Jahresgang oberhalb der tropischen Tropopause durch Einmischung Ozon-reicher extratropischer Luftmassen im Sommer bewirkt.

Contents

1 Introduction

The tropical tropopause layer (TTL), the transition region between troposphere and stratosphere in the tropics, where tropospheric air enters the stratosphere (*Tuck et al.*, 1997; *Highwood and Hoskins*, 1998; *Folkins et al.*, 1999), is a region crucial for atmospheric trends and climate change (*Fueglistaler et al.*, 2009a). Tropospheric air reaches the TTL from below carried upward by deep tropical convection. In the TTL, the ascending branch of the Brewer-Dobson circulation causes further ascent into the stratosphere. Consequently, the TTL can be viewed as the 'gate to the stratosphere'. However, the details of transport in the TTL, like the impact of overshooting convection, turbulent mixing and, in particular, meridional (quasi-isentropic) exchange with the extratropical stratosphere, remain a matter of debate.

The TTL provides the main pathway of tropospheric source gases (e.g., water vapour, anthropogenic pollutants) into the stratosphere. Therefore, trace gas concentrations at entry into the stratosphere are controlled by processes in the TTL. As an example, seasonal and interannual variability as well as long-term trends of stratospheric water vapour have been linked to the variability of the extremely low tropical tropopause temperatures (*Brewer*, 1949; *Randel et al.*, 2004, 2006).

Consequences of climate change, like the potential acceleration of the Brewer-Dobson circulation (*Butchart et al.*, 2006) (see also *Engel et al.*, 2008, for a complementary view from an observational perspective) or a widening of the tropical belt (*Seidel et al.*, 2008), may severely affect processes in the TTL. In particular, changes in the TTL due to increasing greenhouse gas concentrations in the atmosphere are likely to impact troposphere-stratosphere exchange of radiatively active trace gases, and may cause changes in the Earth's radiation budget. Hence, for understanding climate change it is crucial to understand the processes and mechanisms controlling trace gas concentrations in the TTL.

Chemical Transport Models (CTMs) and Chemistry Climate Models (CCMs) are suitable tools to quantify these processes. Contrasting the model results with observations, allows the understanding of these processes to be improved. There are different representations of the transport of trace gases in models, based on regular grids (*Eulerian*) or fuid motion (*Lagrangian*), and on different coordinate systems with differently deduced vertical velocities. It is still an open question, how differences in the transport representation impact the model transport and the simulated distributions of trace gases, like water vapour and ozone. In this work, the impact of the choice of the transport representation on both model transport characteristics and trace gas distributions will be analysed. It will be shown that uncertainties in the transport representation may crucially

impact model predictions.

Consequently, there is the need to validate transport in models. For that purpose, in general, trace gas distributions are simulated using different transport representations and are compared to atmospheric observations. However, validation results might depend on the validation method and, in particular, as will be shown, on the considered trace gas species.

The focus here is on vertical transport, which is generally represented as *diabatic* or *kinematic* transport (e.g., *Kasahara*, 1974; *Schoeberl et al.*, 2003). Diabatic denotes transport calculations in an isentropic (potential temperature) coordinate system with vertical (cross-isentropic) motion determined from diabatic heating rates. Kinematic stands for horizontal transport along surfaces of constant pressure (isobars) with the pressure tendency $\omega = \mathrm{d}p/\mathrm{d}t$ as the vertical velocity. Recent studies indicate a rather large noise in the kinematic wind f eld (*Schoeberl et al.*, 2003; *Krüger et al.*, 2008; *Wohltmann and Rex*, 2008). But it is, so far, an unanswered question whether a diabatic or kinematic transport representation is better suited to model atmospheric transport.

This work aims to shed new light on the subjects touched above. The following main questions regarding transport uncertainties and their impact on model predictions will be addressed:

- *What is the relative importance of the various terms in the diabatic heat budget (e.g., radiation, latent heat release) for tropical troposphere-to-stratosphere transport?*

- *Is there a significant impact of the choice of the transport representation on estimates of transport characteristics (e.g., timescales and pathways) in the TTL?*

- *Is there a significant impact of the choice of the transport representation on model predictions of water vapour and ozone in the TTL?*

- *What can be learnt from the answers to the previous questions regarding the validation of transport in models?*

- *What can be learnt regarding the deduction of atmospheric parameters (e.g., mean ascent rates, descent) from ozone profiles?*

- *Does diabatic or kinematic transport provide a more realistic view of the atmosphere?*

The above def ned main objectives will be broken down into more specif c questions at the beginning of each chapter.

Outline

The introductory chapter (Chapt. 2) presents a brief overview of the TTL, including the main transport processes, as well as water vapour and ozone control mechanisms in this region. To answer the above raised questions, simulations of transport in the TTL are carried out, based both

on backtrajectories and on a full CTM (CLaMS, see *McKenna et al.*, 2002b,a), using various diabatic and kinematic transport representations. The method is described in detail in Chapt. 3.

In Chapt. 4, transport characteristics (e.g., timescales, pathways) are deduced from backtrajectory ensembles based on seven different transport representations, f ve diabatic and two kinematic representations (see also *Ploeger et al.*, 2010). By comparing the f ve diabatic transport calculations (with the vertical velocity deduced from clear-sky and all-sky radiation, clear-sky radiation with latent heat release added, total diabatic heating and total diabatic heating with assimilation increments added) the importance of the different contributions to the diabatic heat budget (radiation, latent heat release) for upward transport from the troposphere to the stratosphere is analysed. Comparison of all seven transport calculations provides a guideline for assessing the sensitivity of trajectory and CTM results to the choice of the transport representation. Therefore, transport characteristics are classif ed into *sensitive* and *robust*, with respect to the choice of the transport representation.

In Chapt. 5, a conceptual backtrajectory approach is presented to predict tropical mean water vapour and ozone concentrations in the upper TTL, based on instantaneous freeze-drying and photochemical production (see also *Ploeger et al.*, 2011). Tropical mean concentrations in the TTL and in-situ measured concentrations during the tropical SCOUT-O3 campaign (see *Brunner et al.*, 2009) are predicted using both diabatic and kinematic transport representations, to study the impact of the choice of the transport representation on simulations of trace gases in the TTL. The different sensitivities of water vapour and ozone as tracers of transport in the TTL and tropical lower stratosphere have considerable consequences for validation of transport in models and for deduction of atmospheric parameters (e.g., mean ascent velocity) from ozone prof les. Furthermore, the backtrajectory analysis allows important insight on processes controlling ozone in the TTL.

Finally, in Chapt. 6, the developed backtrajectory method is applied to analyse the impact of meridional (quasi-isentropic) transport (*in-mixing*) on the seasonality of water vapour and ozone in the TTL. In particular, the link between the annual cycle of ozone and either the annual cycle in Brewer-Dobson circulation driven upwelling (*Randel et al.*, 2007) or the annual cycle in monsoon driven in-mixing will be discussed.

For the diabatic transport simulations discussed in this study, the transport representation in the CLaMS trajectory module (and in the full CLaMS model) was improved compared to earlier work (for vertical transport in CLaMS, see *Konopka et al.*, 2007). The new CLaMS vertical coordinate is orography following in the lowest layer and purely isentropic above 300 hPa, hence throughout the stratosphere, and even in the TTL. The last chapter (Chapt. 7) presents f rst results of full CLaMS simulations, using the new vertical coordinate, and demonstrates that the new diabatic vertical transport representation leads to results in good agreement with respective satellite observations.

Each chapter starts with a brief introductory paragraph, in which the chapter specif c questions are formulated, and ends in a 'chapter conclusions' section, which aims to answer these

questions. The 'summary and conclusions' chapter at the end of this thesis provides both a brief summary of the thesis and answers to the above raised main questions.

This thesis is based on the following papers, all published in peer-reviewed journals:

- *F. Ploeger, S. Fueglistaler, G. Günther, J.-U. Grooß, P. Konopka, S. Liu, R. Müller, F. Ravegnani, C. Schiller, A. Ulanovsky and M. Riese: Insight from ozone and water vapour on transport in the tropical tropopause layer (TTL),* Atmos. Chem. Phys.*, 11, 407–419, 2011.*

- *F. Ploeger, P. Konopka, G. Günther, J.-U. Grooß and R. Müller: Impact of the vertical velocity scheme on modeling transport in the tropical tropopause layer,* J. Geophys. Res.*, 115, D03301, doi: 10.1029/2009JD012023, 2010.*

- *P. Konopka, J.-U. Grooß, G. Günther, F. Ploeger, R. Pommrich, R. Müller and N. Livesey: Annual cycle of ozone at and above the tropical tropopause: observations versus simulations with the Chemical Lagrangian Model of the Stratosphere (CLaMS),* Atmos. Chem. Phys.*, 10, 121–132, 2010.*

- *C. Schiller, J.-U. Grooß, P. Konopka, F. Ploeger, F. H. Silva dos Santos and N. Spelten: Hydration and dehydration at the tropical tropopause,* Atmos. Chem. Phys.*, 9, 17495–17529, 2009.*

- *P. Konopka, J.-U. Grooß, F. Ploeger, and R. Müller: Annual cycle of horizontal in-mixing into the lower tropical stratosphere,* J. Geophys. Res.*, 114, D19111, doi: 10.1029/2009JD011955, 2009.*

2 The tropical tropopause layer (TTL)

The tropical tropopause layer (TTL) is a key region for understanding the composition of the stratosphere, because it is a region of upwelling and transport into the stratosphere and acts as the 'gate to the stratosphere' (*Fueglistaler et al.*, 2009a). Consequently, trace gas mixing ratios at entry into the stratosphere are def ned in the TTL. Therefore, particularly regarding trends in a changing climate, it is crucial to understand the processes controlling trace gas distributions in the TTL.

The TTL is the transition region between the troposphere and the stratosphere in the tropics, where the upwelling air gradually changes characteristics from tropospheric to stratospheric (*Tuck et al.*, 1997; *Highwood and Hoskins*, 1998; *Folkins et al.*, 1999; *Marcy et al.*, 2007). Usually, tropical convection reaches up to around 350 K. Above this *level of main convective outflow*, increasing with altitude, frequent inf uence of stratospheric air is found, e.g., from ozone measurements (*Avallone and Prather*, 1996; *Folkins et al.*, 1999) and tracer–tracer correlations (*Volk et al.*, 1996).

The TTL extends from directly above the level of main convective outf ow to around the highest level which convection, and therefore tropospheric air, can reach. Here, the convention of *Fueglistaler et al.* (2009a) will be adopted, def ning the lower boundary of the TTL at 355 K (14 km / 150 hPa) and the upper boundary at 425 K (18.5 km / 70 hPa), as depicted in Fig. 2.1. It should be noted that there are slightly different def nitions of the TTL in the literature. For example, *Gettelman and Forster* (2002) def ned the TTL to extend vertically from the lapse rate minimum, indicating the level of main convective outf ow, to the cold point tropopause, the level of the temperature minimum at about 380 K in the tropics. A recent analysis of trends in TTL characteristics using different CCMs is given by *Gettelman et al.* (2009), who found a decreasing pressure of the cold point tropopause.

In this work, the terminology of *Holton et al.* (1995) will be frequently used and the tropical atmosphere above a potential temperature of about 380 K will be called *stratospheric overworld*, the stratosphere polewards of the subtropical jets and below about 380 K *extratropical lowermost stratosphere*.

Under clear-sky conditions, in the absence of clouds and convection, the tropical troposphere is dominated by radiative cooling (negative radiative heating rates). Thus, outside convective regions tropospheric air subsides and upward transport is only possible due to convection. Tropical convection causes net transport of tropospheric air up to the level of main convective outf ow, around 350 K. Further above, the Brewer-Dobson circulation (*Dobson et al.*, 1946) causes ascent
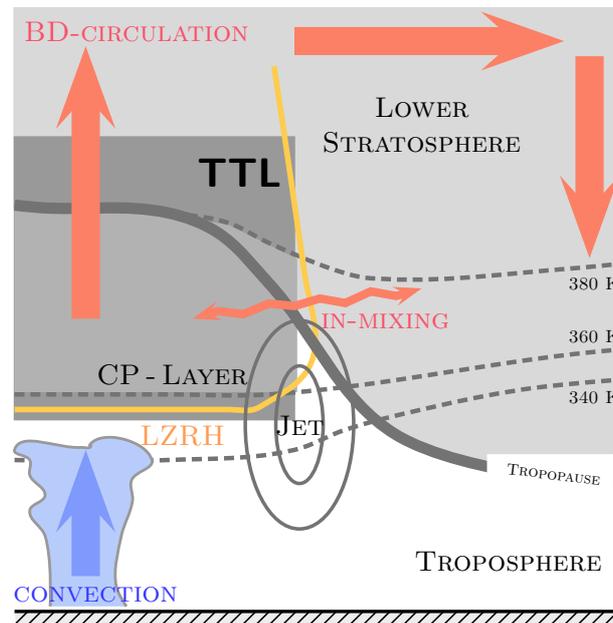
Figure 2.1: The tropical tropopause layer (TTL), illustrated as dark grey shaded region, with the Cold Point (CP) layer inside (light-grey shaded, between 360–380 K). Thick reddish arrows display the stratospheric Brewer-Dobson (BD) circulation, the blue arrow deep tropical convection, the wavy arrow horizontal transport from the extratropics to the tropics (in-mixing) and vice versa. The level of zero radiative heating (LZRH) is shown as an orange line. The tropopause is shown as thick grey, the 340, 360 and 380 K isentropes as dashed grey lines. The subtropical jet core is indicated by grey ellipses.

into the stratosphere, balanced by positive radiative heating (*Gettelman et al.*, 2004a). Therefore, radiative heating rates change sign at about 355 K, the *Level of Zero Radiative Heating* (LZRH), with heating above and cooling below (compare Fig. 2.1 and also Fig. 3.1). The Brewer-Dobson circulation is driven by extratropical wave-breaking via *downward control* (*Haynes et al.*, 1991), the so-called *extratropical pump* (*Holton et al.*, 1995), causing transport deep into the stratosphere. However, the importance of different mechanisms for transport from the main convective outf ow to the stratosphere, such as convective overshooting (*Danielsen*, 1982), in particular above continental areas (*Ricaud et al.*, 2007), lofting in thin cirrus clouds (*Corti et al.*, 2006), mixing (*Konopka et al.*, 2007) and horizontal advection (*Holton and Gettelman*, 2001), is still under debate.

Moreover, there is the question to what extent the upwelling air in the TTL is isolated from or exchanged with the extratropical lowermost stratosphere. Transport from the extratropics into the TTL will be termed *in-mixing* in the following. Overworld and lowermost stratosphere concentrations of trace gas species with tropospheric sources (e.g., very short-lived substances (VSLS), water vapour) largely depend on whether upwelling tropospheric air is mainly directed upward or meridionally transported out of the tropics (compare *Levine et al.*, 2007, 2008). Therefore,

transport in the TTL impacts stratospheric trends (e.g., water vapour) and stratospheric chemistry.

Of particular importance for water vapour transport (compare Sect. 2.3) is the region of minimum temperatures in the TTL, termed the *Cold Point layer* by *Bonazzola and Haynes* (2004). The Cold Point layer is def ned to extend from 360 K to 380 K (see Fig. 2.1).

The TTL is horizontally bounded by the subtropical jets, which are centred around $\pm 30°$ (*Fueglistaler et al.*, 2009a). The jet cores at about 350 K act as strong barriers, limiting horizontal transport between tropics and extratropics (*Haynes and Shuckburgh*, 2000). Above about 370 K, the barrier weakens and horizontal transport occurs more frequently. The subtropical horizontal transport barrier is strongly modulated by monsoonal f ow patterns, namely the Asian and North American ('Mexican') monsoons during boreal summer (June to August) and the Australian and South American ('Bolivian high') monsoons during austral summer (for general references about monsoons see e.g., *Webster et al.*, 1998; *Wang*, 2006). The Asian summer monsoon is by far the strongest monsoon circulation.

Subtropical monsoon circulations were explained by *Gill* (1980) as a response to diabatic heating, which is slightly displaced from the equator. In the upper troposphere and lower stratosphere, monsoons are characterised by strong anticyclonic f ow with equatorward f ow penetrating deeply into the TTL. There is evidence for a strong impact of monsoon circulations on the TTL and lower stratosphere (*Dethof et al.*, 1999; *Gettelman et al.*, 2004b; *Park et al.*, 2006, 2008; *Randel and Park*, 2006) and of associated transport of extratropical air into the TTL (*Chen*, 1995; *Dunkerton*, 1995; *Konopka et al.*, 2009, 2010). However, the overall impact of monsoonal f ow to stratosphere-troposphere exchange is still under debate (e.g., *Randel et al.*, 2010).

Above about 450 K, horizontal transport between the tropics and extratropics is suppressed. This isolation of the inner tropics is termed the *tropical pipe* (*Plumb*, 1996).

2.1 Periodic variations of trace gases in the TTL

Trace gases, as for example water vapour, ozone and carbon monoxide, exhibit periodically varying mixing ratios in the TTL. The most prominent representative is water vapour, with concentrations at the tropical tropopause showing an annual oscillation. Minimum concentrations occur during boreal winter and maximum concentrations during summer. The minima and maxima propagate upwards into the stratosphere with the ascending branch of the Brewer-Dobson circulation and are still discernible at around 10 hPa, about 18 months later (compare Fig. 2.2). This feature of upward propagating water vapour anomalies was f rst observed by *Mote et al.* (1995) and termed the water vapour *tape recorder* (*Mote et al.*, 1996), resembling a tape which is marked at the tropical tropopause.

Generally, trace gas distributions and their variations are described by the transport equation

(compare e.g., *Andrews et al.*, 1987, Eq. (10A.4))

$$\partial_t \mu + v \cdot \nabla \mu = S, \tag{2.1}$$

for tracer mixing ratio μ with a net source (production − loss) term S. The second term on the left hand side of Eq. (2.1) describes tracer advection with the three dimensional velocity $v = (u, v, \dot{\theta})$, with u the zonal, v the meridional wind, ∇ the three dimensional gradient and the dot denoting the time derivative ($\dot{\theta} = d\theta/dt$). In general, the gradient has to be evaluated on the sphere with respect to $x = (\lambda, \varphi, \theta)$, where λ is longitude, φ latitude and θ potential temperature.

Thus, periodic trace gas variations can be forced by periodic variations of the chemical sources and sinks and by periodic variations of the f ow acting on the mixing ratio gradient. From a zonal mean point of view, the second case includes either variations of the meridional velocity v or the upwelling velocity $\dot{\theta}$, or a combination of both.

The wave-driven Brewer-Dobson circulation upwelling in the TTL above the LZRH exhibits an annual cycle with strongest upwelling during boreal winter and weakest upwelling during summer, due to periodic variations in extratropical wave activity (*Haynes et al.*, 1991; *Holton et al.*, 1995). As a result, the vertical velocity $\dot{\theta}$ exhibits a strong annual variation, with stronger upwelling during winter and weaker upwelling during summer. Associated to the annual cycle in upwelling is an annual cycle in upper TTL temperatures, with minimum temperatures in winter and maximum temperatures in summer (*Yulaeva et al.*, 1994). The temperature variations are likely to cause variations in the tracer sources and sinks S. Furthermore, there is also an annual variation in the meridional velocity component v, e.g., due to the above discussed monsoon anticyclonic motions. The stronger Asian and American monsoon systems during boreal summer, compared to the Australian monsoon, cause enhanced meridional transport for boreal summer compared to winter (*Chen*, 1995; *Dunkerton*, 1995). Thus, when analysing trace gas variations all potential contributions to the terms in the transport equation Eq. (2.1) have to be taken into account. Their relative strengths depend on the strengths of sources and sinks as well as on the vertical and meridional gradients of mixing ratio and will differ for different species.

In the following, the two trace gas species water vapour and ozone and their variations in the TTL are discussed in more detail.

2.2 Annual cycle of ozone above the tropical tropopause

In Fig. 2.2/left tropical ozone from the Microwave Limb sounder (MLS) onboard the Aura satellite is shown (averaged between $\pm 10°$ latitude). Evident is the steep vertical ozone gradient in the TTL and lower stratosphere, with concentrations increasing with altitude. Throughout the TTL, ozone mixing ratios increase by about a factor of four. Also horizontal ozone gradients are rather steep.
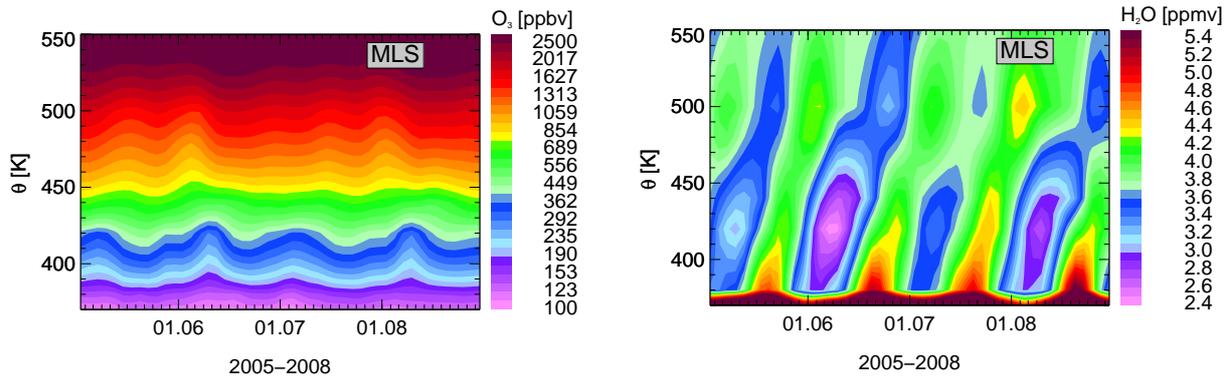
Figure 2.2: Periodic variations of ozone (left) and water vapour (right) in the tropics between $\pm 10°$ latitude from Microwave Limb Sounder (MLS) onboard the Aura satellite. Note the non-linear colour code for ozone.

Avallone and Prather (1996) argued that the main mechanism controlling ozone mixing ratios in the upper TTL and lower tropical stratosphere is photochemical production in slowly rising air masses, due to photodissociation of molecular oxygen (see e.g., *Dessler*, 2000, Chapt. 3)

$$3\,O_2 + h\nu\,(190-215\,\text{nm}) \quad \longrightarrow \quad 2\,O_3\,. \tag{2.2}$$

In addition, *Avallone and Prather* (1996) noticed that horizontal transport from the stratosphere into the TTL is necessary to explain the co-evolution of tropical ozone and odd-nitrogen.

Ozone loss processes due to catalytic reaction with radicals as e.g., HO_x, NO_x, ClO_x (compare *Dessler*, 2000), are slow in the lower tropical stratosphere (*Avallone and Prather*, 1996), but turn out to be crucial higher up. *Osterman et al.* (1997) showed that up to 22.5 km, ozone loss is dominated by reaction with HO_x radicals, displayed in Tab. 7.1 as (R9) and (R10).

An important feature of ozone concentrations in the upper TTL and lower tropical stratosphere is a large annual cycle (*Thompson et al.*, 2003; *Folkins et al.*, 2006; *Randel et al.*, 2007), with maximum concentrations during boreal summer and minimum values during winter. This annual cycle is evident from Fig. 2.2/left in a vertical layer around 420 K. The annual cycle vanishes in the lower TTL and is largest in the upper TTL. In contrast to the water vapour tape recorder (Fig. 2.2/right and Sect. 2.3), there is no obvious upward phase propagation (compare discussion of *Schoeberl et al.*, 2008).

Randel et al. (2007) suggested that the annual ozone cycle is forced by the annual cycle in tropical Brewer-Dobson circulation upwelling, acting on the steep vertical ozone gradient. Slower upwelling during boreal summer implies longer timescales for air masses to rise, hence longer residence times for photochemical ozone production, resulting in larger concentrations compared to winter when tropical upwelling is stronger.

Konopka et al. (2009) further emphasised that also the horizontal gradients are large and therefore the meridional transport terms in Eq. (2.1) are important as well. The neglect of meridional

transport in the simple conceptual one dimensional model of *Konopka et al.* (2009) resulted in a large ozone def cit compared to HALOE and SHADOZ observations of about 40% during boreal summer. Furthermore, three dimensional CLaMS simulations revealed large horizontal transport of ozone from the northern hemisphere (NH, southern hemisphere will be denoted SH in the following) extratropics into the TTL during the months June, July and August, with the same transport pattern evident from HALOE observations (*Konopka et al.*, 2010). *Konopka et al.* (2010) attributed the enhanced in-mixing of ozone rich extratropical air to the Asian monsoon anticyclone and proposed that the Asian monsoon strongly contributes to the annual ozone cycle.

Thus, for the annual variation of ozone all advective terms in Eq. (2.1) seem to be important. On the one hand, the annual cycle in upwelling results in larger ozone production for slower upwelling during boreal summer. On the other hand, the (monsoon induced) annual cycle in horizontal transport causes larger transport of ozone rich air from the extratropical lower stratosphere into the TTL, also during summer. Therefore, ozone concentrations in the upper TTL and tropical lower stratosphere are controlled by a rather complex interplay of horizontal and vertical transport and photochemical production, which will be further investigated in Chapt. 5.

2.3 Hydration and dehydration in the TTL

Figure 2.2/right presents tropical water vapour from MLS (10°S–10°N latitude). Obviously, there is a distinct minimum of water vapour concentrations around 380 K, approximately at the cold point tropopause. Compared to the much higher concentrations of water vapour below, the stratosphere turns out to be rather dry. The extreme dryness above the tropopause is evident not only in the tropics, but is a key feature of the whole stratosphere and led Brewer in 1949 to deduce the stratospheric circulation (*Brewer*, 1949). Essentially, air has to rise in the tropics and to enter the stratosphere across the extremely cold tropical tropopause, with temperatures frequently below 190 K, where freeze-drying and dehydration down to low saturation mixing ratios occurs.

But the observed mean stratospheric entry water vapour is drier than the saturation mixing ratio at the tropical tropopause for mean tropical tropopause temperatures. Consequently, the dryness of the stratosphere cannot be explained from a zonal mean perspective. For this reason, *Newell and Gould-Stewart* (1981) proposed so-called *fountain regions* for entry into the stratosphere, where tropopause temperatures are coldest. As fountain regions they identif ed the tropical Western Pacif c during boreal winter and the Bay of Bengal during summer. *Holton and Gettelman* (2001) modif ed this idea of dedicated regions of effective freeze-drying and proposed that horizontal advection through the cold tropopause above the fountain regions, rather than enhanced upwelling in these regions, is causing the dryness of air before entering the stratosphere.

The most signif cant feature of water vapour above the tropopause is the tape recorder, already mentioned at the beginning of Sect. 2.1, which is clearly evident from Fig. 2.2/right. The tape
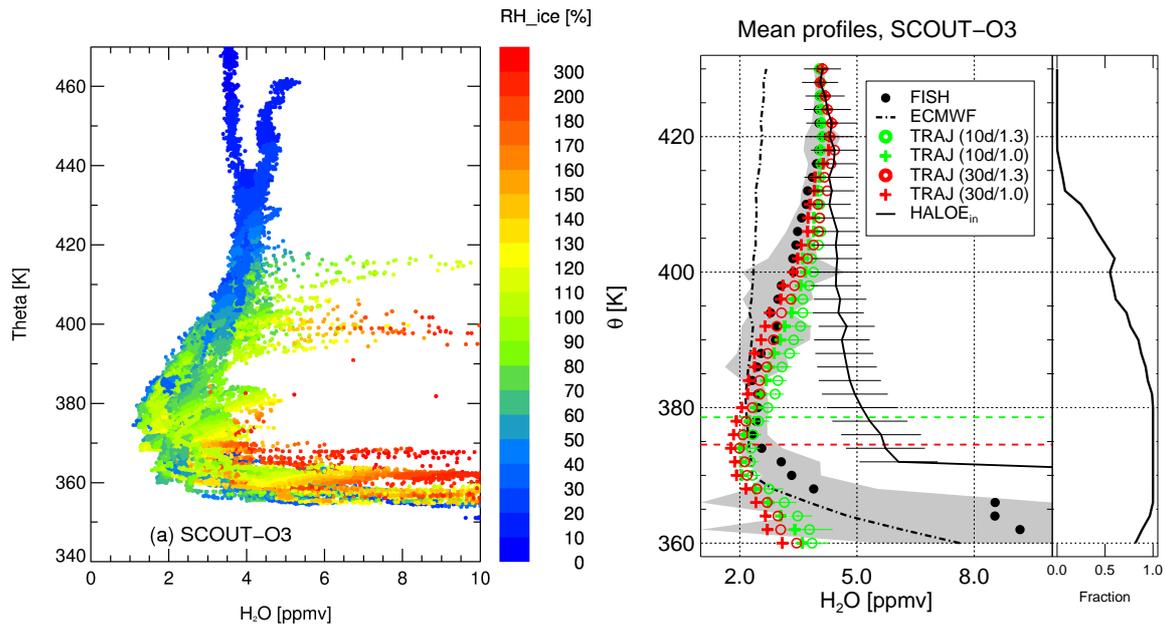
Figure 2.3: (left) Total water prof les during the tropical SCOUT-O3 aircraft campaign in Northern Australia (November/December 2005), measured by the Fast In-situ Stratospheric Hygrometer (FISH). Colour code denotes relative humidity with respect to ice, deduced from total water measurements, hence from the total of gas phase and ice water. (right) Comparison between mean observed and trajectory predicted H_2O prof les (see Sect. 5.1 for details). Backtrajectories started along the f ight tracks, are initialised with climatological HALOE water vapour and calculated backwards for 10 days (green) and 30 days (red). Freeze-drying along the trajectories occurs either at 100% (crosses) or 130% (circles) relative humidity. The black prof le shows the mean HALOE prof le and its standard deviation used for initialisation. The dash-dotted prof le is the ECMWF water vapour interpolated to the f ight tracks. The right subpanel shows the fraction of trajectories along which a cold point below the HALOE initial value is encountered. (Figure adapted from *Schiller et al.*, 2009).

recorder phases of minimum concentration each winter and maximum concentration each summer propagate upwards into the lower stratosphere. These tape recorder phases are caused by the annually varying temperatures at the tropical tropopause with lower temperatures and more eff cient freeze-drying during winter and higher temperatures and less eff cient freeze-drying during summer. While transported upwards, the phases are effaced by in-mixing of extratropical air. Above about 450 K, in the tropical pipe, in-mixing is reduced and the phase propagation continues rather undisturbed.

However, many questions concerning the water vapour entry into the stratosphere, as the microphysics of freeze-drying or the role of convection for stratospheric water vapour, still remain unanswered. *Schiller et al.* (2009) analysed in-situ airborne water vapour measurements from three tropical research campaigns (SCOUT-O3 in Northern Australia, November/December 2005; TroCCiNOx in Brazil, January/February 2005; AMMA/SCOUT-O3 in Burkina Faso, Au-

gust 2006) to investigate the mechanisms of hydration and dehydration at the tropical tropopause.

Figure 2.3/left shows total water measurements of the Fast In-situ Stratospheric Hygrometer (FISH) (*Zöger et al.*, 1999) during SCOUT-O3. The colour code denotes the relative humidity with respect to ice. The high relative humidity values indicate that freeze-drying had occurred near-by and not long ago in the backward history of air, the *Lagrangian temperature/saturation history*. Figure 2.3 clearly shows how the water vapour minimum (hygropause) is caused at the tropical tropopause due to eff cient freeze-drying. Above about 420 K the regional signal in the in situ observations (minimum) is strongly effaced, and the in situ observations are close to the zonal mean HALOE observations (black solid line).

The results of a trajectory reconstruction (exact method described in Sect. 3.3.1 and Sect. 5.1) in Fig. 2.3/right show that the observations are consistent with freeze-drying down to saturation at the minimum temperatures in the Lagrangian temperature history. The difference of about 3 ppmv (concentration in parts per million by volume) between the trajectory reconstructed and the zonal mean HALOE mixing ratios (black solid) emphasises the importance of the Western Pacif c as a region of effective freeze-drying.

The difference between reconstruction and observation below the tropopause, with the observation exceeding the reconstruction, is attributed to convection. The f ights took place in regions of frequent convection. The trajectory reconstruction neglects convection, as it is based on large-scale meteorological data. Thus, *Schiller et al.* (2009) interpreted the fact that observed water vapour exceeds reconstructed water vapour as a moistening effect of convection, which is absent in the trajectory calculation. Also other authors (e.g., *Corti et al.*, 2008) found that convection moistens its environment. Above the tropopause, around 380 K, the reconstruction agrees well with the observation. Therefore, *Schiller et al.* (2009) argued that although convection moistens its environment, the overall impact on stratospheric entry water vapour amounts to less than 10%, because convectively moistened air at or above the tropopause is still freeze-dried to lower mixing ratios.

To summarise, from global observations as well as from high-resolution in-situ observations it is found that the tropical water vapour entry into the stratosphere is a highly complex interplay between freeze-drying in the coldest regions of the TTL and fresh supply of water by convection. The Lagrangian saturation history on timescales of about one month appears to be appropriate and suff cient to describe the average water vapour distribution at the cold point tropopause and in the f rst kilometres above.

3 Data and method

In this work, trace gas distributions are simulated using both a conceptual backtrajectory and a full Chemical Transport Model (CTM) approach. For both approaches the *Chemical Lagrangian Model of the Stratosphere* (CLaMS) (see *McKenna et al.*, 2002b,a) is used (for the trajectory approach only the CLaMS trajectory module). For the results presented in this work, model transport is driven by European Centre for Medium-range Weather Forecasts (ECMWF) meteorological renanalysis data (ERA-Interim, see below), and operational analysis data for comparison. Simulations are carried out in different vertical coordinate systems with differently deduced vertical velocities (different vertical *transport representations*), as explained in Sect. 3.2.

3.1 ERA-Interim reanalysis

Data assimilation systems combine the results of CCMs with atmospheric observations to provide different types of assimilated meteorological datasets (e.g., winds, temperature), constituting a model atmosphere as realistic as possible. These meteorological datasets are the basis for CTM and trajectory studies.

Among other data products, the ECMWF provides reanalysis and operational meteorological data. The operational assimilation system produces the state of the atmosphere close to real time and is updated from time to time to improve physical parametrizations or to include new observations. On the contrary, the reanalysis assimilation system is run unchanged throughout the reanalysis period. Therefore, a main advantage of reanalysis compared to operational meteorological data is their suitability for studies of longer-term atmospheric variability.

To incorporate the advances of the further developed operational data assimilation system (compared to ERA-40 reanalysis, see *Uppala et al.*, 2005) into a reanalysis product, the ECMWF recently created the ERA-Interim reanalysis. ERA-Interim data covers the observation rich period from 1989 to present, and the generation of data will be continued near real time as an ECMWF Climate Data Assimilation System. ERA-Interim reanalysis are described in detail by *Simmons et al.* (2006) and *Uppala et al.* (2008).

ERA-Interim is based on a 4D variational assimilation scheme (4D–Var) with a 12 hour assimilation cycle. The data assimilation system uses a T255 horizontal resolution and 60 hybrid levels in the vertical, with the hybrid vertical coordinate combining an orography following coordinate at the lowest level with pressure above approximately the tropical tropopause (compare

Simmons and Burridge, 1981). Model physics has improved compared to ERA-40 reanalysis, including e.g., a supersaturation scheme for ice microphysics (*Tompkins et al.*, 2007).

In ERA-Interim many shortcomings of ERA-40 reanalysis seem signif cantly improved. The too strong precipitation above the tropical oceans in ERA-40 is reduced (*Simmons et al.*, 2006). Moreover, the unrealistic oscillatory structure in ERA-40 polar stratospheric temperature prof les appears much smaller in amplitude for ERA-Interim (*Simmons et al.*, 2006; *Fueglistaler et al.*, 2009b). Moreover, the stratospheric Brewer-Dobson circulation, which is much too strong in ERA-40, appears weaker in ERA-Interim, resulting in a more realistic stratospheric age of air (*Monge-Sanz et al.*, 2007) and a slower, more realistic, ascent of the water vapour tape recorder (*Simmons et al.*, 2006).

3.2 Diabatic versus kinematic transport

The primitive equations, describing atmospheric motion, can be expressed in different coordinate systems (compare e.g., *Kasahara*, 1974; *Andrews et al.*, 1987; *Holton*, 1992; *Salby*, 1996). A particular choice of coordinates usually simplif es certain aspects of the motion. Throughout this work isobaric and isentropic coordinate systems are used, with vertical coordinates pressure p and potential temperature θ, respectively. These coordinate systems constitute the framework for kinematic and diabatic transport calculations, as will be explained below. The full set of primitive equations in isobaric and isentropic coordinates can be looked up in (e.g., *Salby*, 1996, Chapt. 11).

Vertical velocity in isobaric coordinates is given by the pressure tendency $\omega = \dot{p}$, in isentropic coordinates by potential temperature tendency $\dot{\theta}$. Vertical velocity for synoptic scale motions is usually of the order of a few centimetres per second. Because routine meteorological soundings measure wind speed with an accuracy of about a meter per second, vertical velocity is not measured directly, but must be deduced from other meteorological f elds. Normally, the atmosphere is close to hydrostatic equilibrium and the vertical momentum balance reduces to the hydrostatic equation and is not adequate to determine vertical velocity. For this reason, vertical velocity has to be deduced from other equations. Two common methods to calculate vertical velocity are the kinematic and the diabatic method, based on the continuity equation and the energy balance equation, respectively.

The kinematic method is applied in isobaric coordinates. Vertical velocity ω at pressure p is calculated by vertically integrating the continuity equation from surface pressure p_s to p (e.g., *Holton*, 1992, Chapt. 3.5)

$$\omega = \omega_s - \int_{p_s}^{p} \nabla^h \cdot \mathbf{v}^h \, dp. \tag{3.1}$$

Here, $\mathbf{v}^h = (u, v)$ is the horizontal velocity and ∇^h the horizontal gradient. Because the middle atmosphere is dominated by horizontal motion, the horizontal velocity components turn out to

be much larger than ω. Therefore, small errors in u and v might induce large errors in ω via Eq. (3.1).

The diabatic method is applied in isentropic coordinates. Cross-isentropic vertical velocity $\dot{\theta}$ is calculated from the diabatic heating rate Q via the energy balance equation (compare *Andrews et al.*, 1987, Eq. (3.1.3e); note the slightly different defnition of Q)

$$\dot{\theta} = Q \frac{\theta}{T}, \tag{3.2}$$

with temperature T. In many textbooks the diabatic heating rate is denoted J. The Q defned in Eq. (3.2) is related to J via $Q = J/c_p$, with c_p the specifc heat capacity at constant pressure. The diabatic heating rate Q consists of the sum of radiative heating Q_{rad}, diffusive and turbulent heating Q_{diff} and latent heat release Q_{lat}

$$Q = Q_{\text{rad}} + Q_{\text{diff}} + Q_{\text{lat}}. \tag{3.3}$$

Above the tropopause and throughout the middle atmosphere radiative heating contributes the largest part to the diabatic heat budget. In the lower TTL below the tropopause and, in particular, in the troposphere latent heat release becomes important.

Of course, ideally the diabatic and kinematic methods should yield identical vertical motion, as the sets of governing equations are equivalent. But the vertical velocity calculations are based on different meteorological felds (diabatic: diabatic heating; kinematic: horizontal wind) and on different equations (diabatic: energy balance; kinematic: mass balance), involving different length- and timescales and different numerics. Hence, kinematic and diabatic vertical motion might differ. Therefore, results of transport simulations in diabatic and kinematic representations might differ as well.

3.2.1 The diabatic heat budget

Usually, the diabatic heating rate is further separated by dividing radiative heating into short- and long-wave, or into clear-sky and cloud radiative heating contributions. Because one aim of this study is to isolate the heating effects due to clear-sky and cloud radiation, the second separation is adopted here, hence

$$Q_{\text{rad}} = Q_{\text{clear-sky}} + Q_{\text{cloud}}. \tag{3.4}$$

With respect to this separation, Q_{rad} is termed all-sky radiative heating and denoted $Q_{\text{all-sky}}$, in the following.

In this study, ERA-Interim diabatic heating rates are used, which have a much better quality than heating rates from ERA-40. As explained in Sect. 3.1, ERA-40 heating rates exhibit a rather excessive tropical circulation (*Uppala et al.*, 2005; *Monge-Sanz et al.*, 2007) and unrealistic oscillations in the high latitude heating feld (*Fueglistaler et al.*, 2009b).

Table 3.1: Defnitions of the different vertical transport representations used for transport simulations in this study

representation	dataset	vertical coordinate	vertical velocity	
clear-sky	ERA-Int.	θ	$\sim Q_{\text{clear}-\text{sky}}$	clear-sky radiation
all-sky	ERA-Int.	θ	$\sim Q_{\text{all}-\text{sky}}$	all-sky radiation
latent	ERA-Int.	θ	$\sim Q_{\text{res}}$	residual heating
				= latent+mixing+clear-sky
diabatic	ERA-Int.	θ	$\sim Q$	total heating
assim	ERA-Int.	θ	$\sim Q_{\text{assim}}$	assimilation increment
				+ total heating
kinematic	ERA-Int.	p	$\omega = \mathrm{d}p/\mathrm{d}t$	
kin-OP	op.ECMWF	p	$\omega = \mathrm{d}p/\mathrm{d}t$	

The heating rate information is taken from ERA-Interim forecast data. Heating rates are mean quantities, integrated over the forecast time step. Therefore, the 6h forecasts at 00/12 UTC provide heating rates at 03/15 UTC. Likewise, the 12h forecasts at 00/12 UTC provide heating rates at 06/18 UTC. There are four reanalyses per day, at 00, 06, 12 and 18 UTC. Heating rates for the 06/18 UTC reanalyses are given by the 12h forecasts at 00/12 UTC. Heating rates for the 00 UTC reanalyses are linearly interpolated in time from the 12h forecast at 12 UTC and the 6h forecast at 00 UTC. Heating rates for the 12 UTC reanalysis are interpolated from the 12h forecast at 00 UTC and the 6h forecast at 12 UTC.

The forecasts include short-wave and long-wave radiative heating rates due to clear-sky radiation ($Q_{\text{clear}-\text{sky}}^{\text{sw}}$, $Q_{\text{clear}-\text{sky}}^{\text{lw}}$), all-sky radiation ($Q_{\text{all}-\text{sky}}^{\text{sw}}$, $Q_{\text{all}-\text{sky}}^{\text{lw}}$) and the total diabatic heating rate Q. From these heating rates the clear-sky and all-sky radiative heating rates are calculated according to

$$Q_{\text{clear}-\text{sky}} = Q_{\text{clear}-\text{sky}}^{\text{sw}} + Q_{\text{clear}-\text{sky}}^{\text{lw}}, \tag{3.5}$$

$$Q_{\text{all}-\text{sky}} = Q_{\text{all}-\text{sky}}^{\text{sw}} + Q_{\text{all}-\text{sky}}^{\text{lw}}. \tag{3.6}$$

Furthermore, the heating rate due to latent heat release, diffusive and turbulent heat transport is computed as a residual heating rate by subtracting the all-sky from the total diabatic heating rate, $\widetilde{Q}_{\text{res}} = Q - Q_{\text{all}-\text{sky}}$. *Fueglistaler et al.* (2009b) already mentioned that it is not possible to separate the latent heating rate alone from the forecasts, but only the term $\widetilde{Q}_{\text{res}}$, comprising the sum of latent heat release and diffusive and turbulent heat transport. For the further calculations in this work, the residual heating rate is redefned as $Q_{\text{res}} = \widetilde{Q}_{\text{res}} + Q_{\text{clear}-\text{sky}}$. Above about 360 K, clear-sky radiative heating contributes the largest term to the tropical diabatic heating budget (compare Fig. 3.1). Hence, in the TTL above the clear-sky level of zero radiative heating, clear-sky radiation may be viewed as a heating background, to which the radiative effects of clouds and of residual heating are added.

Further, a heating rate due to the assimilation (the assimilation increment) can be derived, as described in *Fueglistaler et al.* (2009b), and added to the total diabatic heating rate Q. In the following, assimilation increment denotes the total

$$Q_{\text{assim}} = c_p \frac{T_{\text{an}} - T_{\text{fc}}}{\Delta t_{\text{fc}}} + Q = \widetilde{Q}_{\text{assim}} + Q. \qquad (3.7)$$

Here, T_{an} denotes reanalysis, T_{fc} forecast temperature and Δt_{fc} the forecast time step. The assimilation increment is required to close the heat budget and is interesting to look at, as it represents that part of the heating resulting from disagreements between model and observations.

To summarise, this work is based on f ve diabatic transport representations from ERA-Interim with different diabatic heating rates. In the following, these are denoted *clear-sky* ($Q_{\text{clear-sky}}$), *all-sky* ($Q_{\text{all-sky}}$), *latent* (Q_{res}), *diabatic* (Q) and *assim* (assimilation, Q_{assim}). Moreover, two kinematic representations of ERA-Interim and operational ECMWF data on pressure levels together with the corresponding pressure tendency ω (denoted *kinematic* and *kin-OP*) will be considered. Table 3.1 summarises the seven different representations, which will allow to quantify the effects of various physical parameters (clear-sky heating rates, cloud and residual heat effects) on transport as well as to compare the diabatic to the kinematic approach and the interim to the operational ECMWF data.

With the above def ned heating rates, the ERA-Interim diabatic heat budget is written as

$$Q = Q_{\text{clear-sky}} + Q_{\text{cloud}} + \widetilde{Q}_{\text{res}}, \qquad (3.8)$$

with $Q_{\text{cloud}} = Q_{\text{all-sky}} - Q_{\text{clear-sky}}$ (compare Eq. (3.4)). The various contributions to the ERA-Interim diabatic heat budget for 2002 are shown in Fig. 3.1 as zonal means on pressure levels.

Evident from Fig. 3.1a, clear-sky radiation is heating the tropical atmosphere above about 360 K, the clear-sky LZRH (pink line). The troposphere, in contrast, is radiatively cooled. Thus, in a hypothetical atmosphere with clear-sky radiation as the only diabatic heating term, no upward transport from the troposphere into the stratosphere is possible. There are various studies estimating the LZRH altitude, based on trace gas observations and radiative transfer calculations (*Folkins et al.*, 1999; *Gettelman and Forster*, 2002; *Gettelman et al.*, 2004a). These studies all agree roughly with the LZRH at around 15 km (about 360 K), slightly higher for *Gettelman and Forster* (2002). *Gettelman et al.* (2004a) further assess the effect of different trace gases on the LZRH altitude. They f nd that both increasing O_3 and CO concentrations in the TTL lower the LZRH, due to enhanced absorption of short-wave radiance, whereas increasing H_2O concentrations elevate the LZRH, due to enhanced long-wave cooling.

Figure 3.1b shows that the radiative effect of clouds is strongest and positive (heating) in the tropics directly below the clear-sky LZRH. Therefore, clouds lower the LZRH and the all-sky LZRH is at about 355 K, slightly below the clear-sky LZRH.

However, Fig. 3.1 corresponds to 'ECMWF world' and the effect of clouds on the LZRH altitude is not without controversy. Various authors have recently analysed the radiative heating
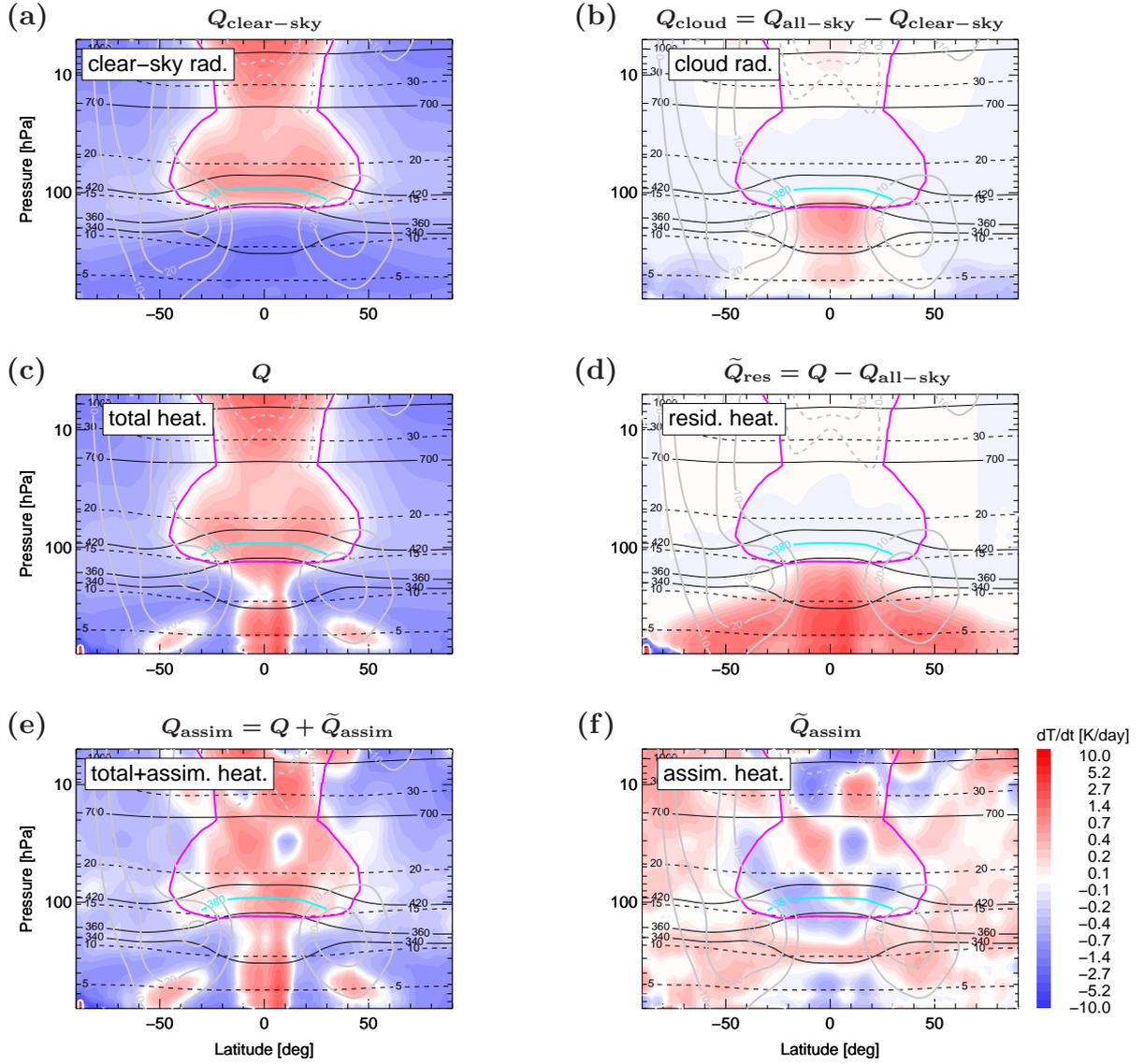
Figure 3.1: Zonal mean contributions to the diabatic heat budget (a: clear-sky radiation, b: radiative effects of clouds, c: total diabatic heating, d: residual heating, e: sum of total diabatic heating and assimilation increments, f: assimilation increments) from ERA-Interim for 2002. The clear-sky LZRH is in pink, zonal wind contours in grey, the tropical tropopause (380 K) in cyan. Isentropes are shown as black solid and lines of constant geopotential height as black dashed lines. Note the non-linear colour code.

contribution of clouds in the TTL (*Gettelman et al.*, 2004a; *Corti et al.*, 2006; *Fueglistaler and Fu*, 2006). Above the cloud layer, they f nd heating due to enhanced short-wave, compensated by cooling due to reduced long-wave upwelling f uxes, resulting in a net cooling. *Fueglistaler and Fu* (2006) estimate this cooling effect to be –0.2 K/day. In the cloud layer, *Fueglistaler and Fu* (2006) and *Corti et al.* (2006) f nd heating due to clouds. The change of the LZRH altitude due to clouds results from heating in the cloud layer and cooling above. The sensitive balance of these
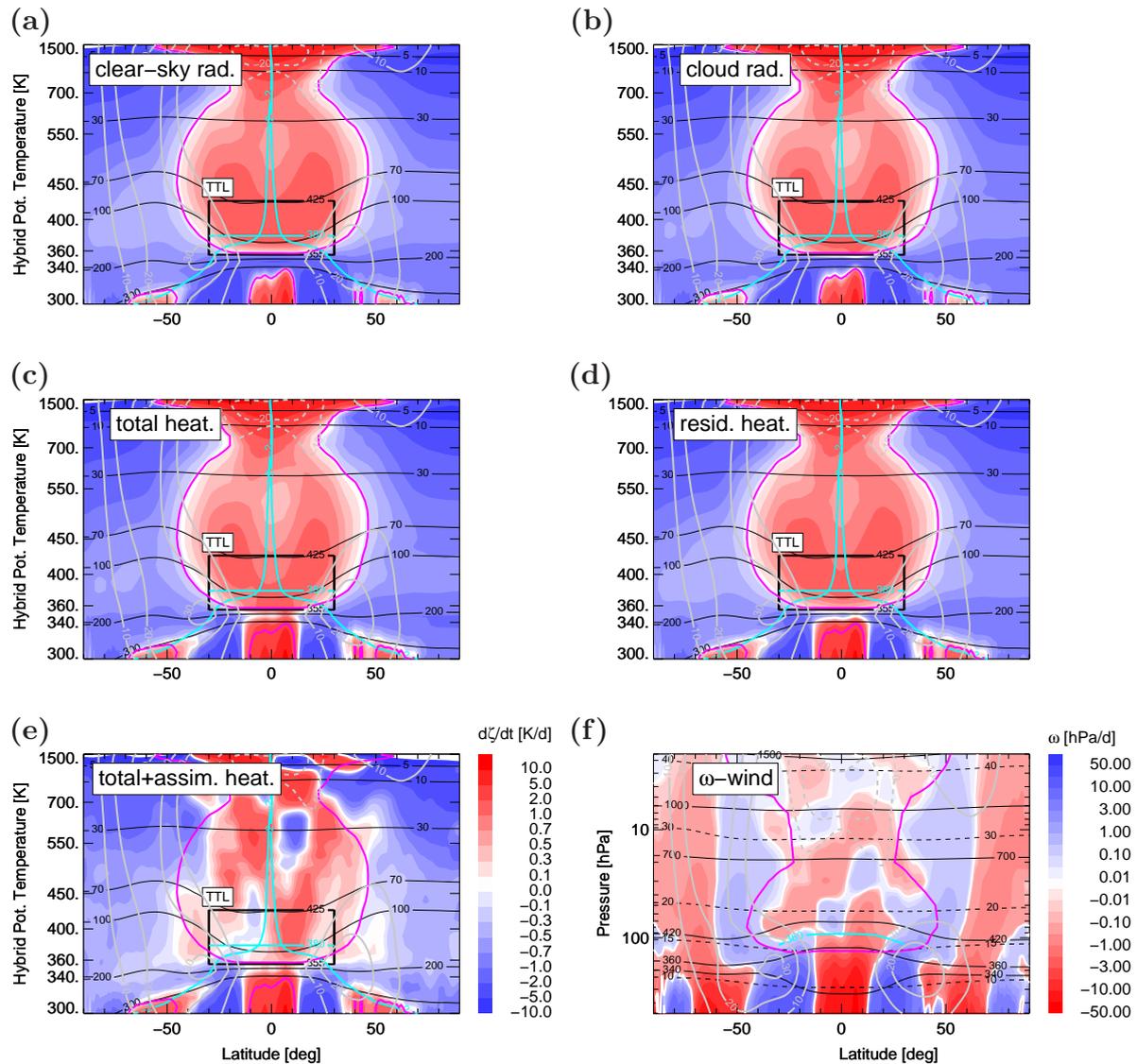
Figure 3.2: Zonal mean vertical cross isentropic velocities from the various diabatic heating rates (a: clear-sky radiation, b: radiative effects of clouds, c: total diabatic heating, d: residual heating, e: sum of total diabatic heating and assimilation increments) and the vertical ω-wind (f) for comparison, from ERA-Interim for 2002. The LZRH is in pink, the tropopause (380 K in the tropics, 2 PVU in the extratropics) in cyan, the zonal wind contours are in grey and isobars in black. In the ω-plot (f), isentropes are shown as black solid lines and lines of constant geopotential height as black dashed lines. The TTL (30°S–30°N latitude, 355–425 K potential temperature) is illustrated as a black rectangular. Note the non-linear colour code and the entropy weighted non-linear vertical axis. Hybrid potential temperature exactly equals potential temperature above 300 hPa.

two opposing effects renders estimates of LZRH altitude changes due to clouds challenging. *Gettelman et al.* (2004a) f nd a higher LZRH due to clouds, whereas *Fueglistaler and Fu* (2006) and *Corti et al.* (2006) emphasise that clouds lower the LZRH. Figure 3.1a/b shows that in ERA-

Interim clouds lower the LZRH, in agreement with *Fueglistaler and Fu* (2006) and *Corti et al.* (2006) rather than with *Gettelman et al.* (2004a).

The main effect of the residual heating term is a strong positive heating in the troposphere due to latent heat release (Fig. 3.1d), strongest in the tropics. The sum of clear-sky and cloud radiation and residual heating, hence the total diabatic heating in Fig. 3.1c, exhibits positive mean heating rates throughout the tropics from the troposphere to the stratosphere. However, a bottleneck of minimum positive heating remains above 340 K, at the lower edge of the TTL (*Fueglistaler et al.*, 2009b).

The assimilation increment contributes a rather patchy heating rate, evident from Fig. 3.1f, which is ref ected also in the sum of total diabatic and assimilation increment heating (assim) in Fig. 3.1e. Throughout the TTL, the assimilation increment has a cooling effect of about -0.2 K/day. Interpreting the assimilation increment as a term, which corrects the model diabatic heating, with respect to observations, this discrepancy indicates that diabatic heating throughout the TTL, and therefore upwelling (compare Eq. (3.2)), is slightly too strong in ERA-Interim. Above an altitude of about 20 km above the equator, where the assimilation increment contributes a positive heating rate, the model diabatic heating seems too weak (compare e.g., *Fueglistaler et al.*, 2009b).

The vertical cross-isentropic velocities $\dot{\theta}$ are calculated from the diabatic heating rates via Eq. (3.2) and plotted in Fig. 3.2 as zonal means against hybrid potential temperature ζ. Hybrid potential temperature ζ is def ned (compare App. A.1, Eq. (A.1)) according to *Mahowald et al.* (2002) and *Konopka et al.* (2007), and in the region of interest for this work it exactly equals potential temperature. In the following, ζ will be denoted potential temperature and $\dot{\zeta}$ cross-isentropic velocity for simplicity, as explained below in Sect. 3.3.2 and App. A.1.

Figure 3.2 shows cross-isentropic velocity $\dot{\zeta}$ for the diabatic heating rates $Q_{\text{clear}-\text{sky}}$, $Q_{\text{all}-\text{sky}}$, Q_{res}, Q and Q_{assim}, together with the ω-wind. Below the LZRH, cross-isentropic velocity from clear-sky, all-sky or residual heating exhibits negative values, consistent with diabatic cooling in Fig. 3.1. Only for the sum of all three terms (total diabatic heating) the tropical vertical velocity is positive from the troposphere to the stratosphere. The contributions of the various diabatic heating terms to the tropical upwelling will be further discussed in Sect. 4.2.

For the vertical velocity deduced from the sum of total diabatic and assimilation increment heating in Fig. 3.2e, the distribution looks rather patchy compared to the other four diabatic velocities. In the tropical stratosphere (30–10 hPa), the assimilation increment even causes regions of mean negative, downward velocity.

3.3 Transport modelling

This work is based on two methods to simulate transport and the distribution of trace gases in the atmosphere. The f rst, used in Chapt. 4 and Chapt. 5, is a conceptual backtrajectory approach.

The second is based on a full CTM (CLaMS) and will be used in the second part of Chapt. 5. In the following the two methods will be briefly discussed.

3.3.1 Trajectory method

A trajectory is defined as the path, which an air parcel carries out in the atmospheric flow field $v(t,x)$, with t time and x the three dimensional position vector. Therefore, trajectories $x(t)$ are determined by the differential equation

$$\frac{dx(t)}{dt} = v(t, x(t)),\tag{3.9}$$

together with the initial value $x_0 = x(t_0)$.

Releasing trajectories in the (atmospheric) flow and tracking their motion provides a simple method for studying flow properties. Because different trajectories are viewed isolated from each other, a pure trajectory approach, without any additional mixing parametrization, captures only the advective part of transport. Therefore, trajectories are reversible in time and forward and backward trajectory calculations (forward or backward in time) are both feasible. All trajectory analyses in this work are based on backward trajectories (backtrajectories, for brevity).

Because of the limited accuracy of three-dimensional analysed winds it is not feasible to follow single trajectories, and interpreting results from single trajectories over a period of months would be misleading. Therefore, large ensembles of backtrajectories are considered and statistical mean properties of ensembles are inferred, which is a reliable method (compare e.g., *Fueglistaler et al.*, 2005). Of course, even for large ensembles mean results of trajectory calculations are unreliable for long integration timescales, when mixing with air outside the ensemble becomes important.

It is elucidating to apply the method of characteristics (compare e.g., *John*, 1987, Chapt. 1) to the advective transport equation Eq. (2.1). Loosely speaking, a characteristic curve of a partial differential equation is a curve with the vector of coefficients of the differential operator as tangent. For the advective transport equation Eq. (2.1), the coefficient vector reads $(1, v)$. Hence, characteristic curves for the advective transport equation are the trajectories, defined by Eq. (3.9). Along characteristic curves the partial differential equation reduces to an ordinary differential equation. Consequently, along a trajectory the partial differential equation Eq. (2.1) reduces to $\frac{d\mu(t)}{dt} = S(t)$, with t time.

Hence, the solution of the advective transport equation along a trajectory is given by

$$\mu(t) = \mu_0 + \int_{t_0}^{t} S(t')dt',\tag{3.10}$$

with initial value $\mu_0 = \mu(t_0)$. Consequently, the mixing ratio $\mu(t)$ of a trajectory at time t consists of two parts, the mixing ratio μ_0 at t_0 and the integrated net production (production − loss) along the trajectory.

In Chapt. 5 water vapour and ozone concentrations, in Chapt. 6 also carbon monoxide concentrations are predicted from backtrajectories. The trajectory prediction method is explained in detail in Sect. 5.1 for H$_2$O and O$_3$, and in Chapt. 6 for CO .

3.3.2 The Chemical Lagrangian Model of the Stratosphere (CLaMS)

This section gives a brief overview of the Chemical Lagrangian Model of the Stratosphere (CLaMS), which was developed at the Forschungszentrum Jülich. Detailed descriptions can be found in *McKenna et al.* (2002b,a) and *Konopka et al.* (2004, 2007). CLaMS is a Lagrangian CTM, based on forward trajectories. Irreversible transport due to atmospheric mixing processes is captured via a Lyapunov exponent based mixing parametrization. The main components of the CLaMS model, the Lagrangian trajectories, the Lyapunov exponent based mixing and the Chemistry model, are separated into sub-modules, as displayed in Fig. 3.3. The sub-modules can be composed, adapted to the respective problem.

In the conf guration used for this study, at each CLaMS time step f rst the trajectories are calculated, then successively chemistry, mixing and f nally dehydration due to a simple cirrus treatment.

The trajectory calculation starts with an ensemble of points in space (CLaMS air parcels) at initial time and advects them forward for the CLaMS time step. Wind f elds are taken from meteorological analysis (here, ERA-Interim). Vertical velocities can be deduced from meteorological data, or using a CLaMS preprocessor, which calculates clear-sky diabatic heating rates, using the Morcrette-scheme (*Morcrette*, 1991). For this study, vertical velocities are always deduced from ERA-Interim data, as described in Sect. 3.2.1. The trajectory calculation is based on the fourth-order Runge-Kutta scheme.

With the CLaMS trajectory module, it is feasible to calculate trajectories either in a diabatic or in a kinematic framework (compare Sect. 3.2). For the kinematic calculations the meteorological data was interpolated from the ECMWF hybrid vertical coordinate to pressure levels with vertical velocity ω. For the diabatic calculations the meteorological data was interpolated to potential temperature levels and the vertical velocity $\dot{\theta}$ calculated as one of the f ve different diabatic heating rates (Sect. 3.2.1).

Chemistry along the trajectories is calculated based on the ASAD code (*Carver et al.*, 1997), as explained in *McKenna et al.* (2002a). For the simulations in this study a simplif ed chemistry conf guration (e.g., *Konopka et al.*, 2010; *Pommrich et al.*, 2010a) is used, described in Chapt. 7.

For the mixing algorithm, nearest neighbours of each CLaMS air parcel are determined, using Delaunay triangulation (*Preparata and Shamos*, 1985; *McKenna et al.*, 2002b). If the separation distance between two parcels falls below a critical minimum distance, the two parcels are merged together. If the separation distance exceeds a critical maximum distance, a new parcel is inserted in between. Properties of new parcels are determined as mean properties of the old parcels. Critical distances are def ned via one critical Lyapunov exponent λ_{Lyap} (compare *McKenna et al.*,
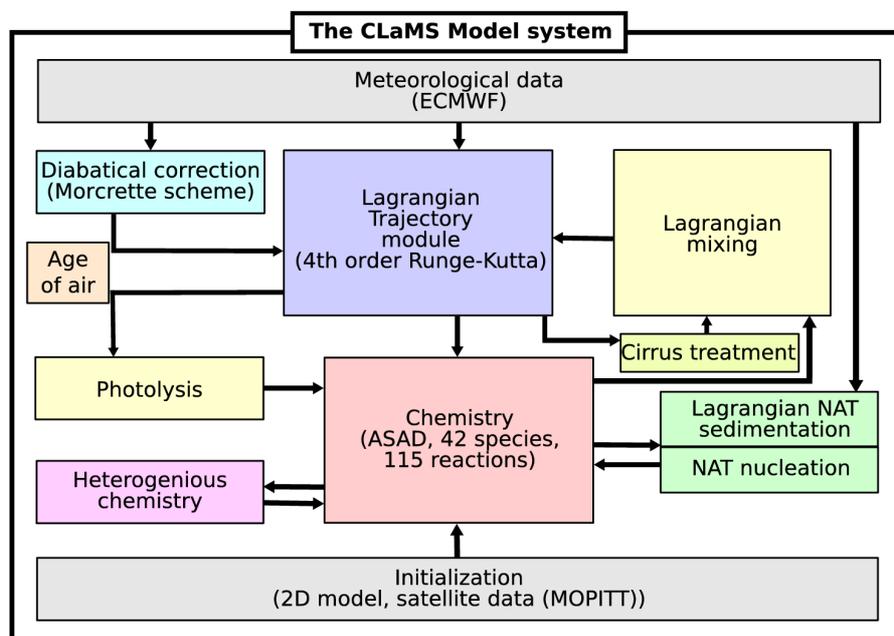
Figure 3.3: The Chemical Lagrangian Model of the Stratosphere (CLaMS).

2002b). Therefore, mixing in CLaMS is controlled by the deformation rate of the f ow. In regions of strong f ow deformations, like the subtropical jet regions (*Pan et al.*, 2006; *Konopka et al.*, 2007), strong mixing occurs. In regions of weak f ow deformations mixing is weak.

Freeze-drying of water vapour (dehydration), occurring mainly at the tropical tropopause as explained in Sect. 2.3, is calculated based on a simplif ed cirrus treatment (compare *von Hobe et al.*, 2011). If supersaturation of a CLaMS air parcel exceeds a parametrized 'nucleation barrier', the water vapour in excess of the saturation mixing ratio is instantaneously transformed to the ice phase. With respect to the parcel ice water content, a mean ice particle radius and a corresponding fall velocity are calculated. The sedimentation length for the time step is compared to a chosen characteristic length (typical cirrus thickness), and a respective fraction of ice is removed (dehydration). If the parcel is sub-saturated and ice exists, ice is instantaneously evaporated to maintain saturation.

Vertical transport in CLaMS

For the simulations of this study, the vertical transport representation in CLaMS was improved. The former representation, based on the hybrid potential temperature coordinate ζ of (*Mahowald et al.*, 2002) was introduced by *Konopka et al.* (2007). *Konopka et al.* (2007) already mentioned certain shortcomings of this representation, as too weak upwelling in the tropics around the LZRH (due to the clear-sky approximation to diabatic heating), excessive Ferrel cells in the extratropics, and lines of constant ζ intersecting the ground. All these shortcomings are resolved

by introducing a slightly changed new hybrid potential temperature coordinate, which is also denoted ζ in the following. Throughout this work, ζ always refers to the new, improved coordinate. Main characteristics of the new ζ coordinate are:

- Isentropic coordinates throughout the stratosphere, because $\zeta = \theta$ above about 300 hPa.

- Smooth transformation into $\sigma = \frac{p}{p_s}$ below about 300 hPa, with p_s surface pressure.

- Orography following coordinate (σ) in the lower troposphere.

The detailed def nition of the new hybrid potential temperature ζ is given in App. A.

It should be noted that the vertical velocity $\dot{\zeta}$ in hybrid potential temperature coordinates exactly equals cross-isentropic velocity $\dot{\theta}$ above about 300 hPa, because hybrid potential temperature equals potential temperature in this region. In the troposphere $\dot{\zeta}$ transforms into $\dot{\sigma}$. As this work focusses on the atmosphere above about 300 hPa, $\dot{\zeta}$ equals $\dot{\theta}$ in the region of interest. For simplicity, ζ will be denoted potential temperature and $\dot{\zeta}$ cross-isentropic velocity, in the following. Nevertheless, most of the results of this work were derived both in potential temperature and hybrid potential temperature space. The difference is always negligible.

4 Impact of the transport representation on modelling transport in the TTL

Several model studies of transport in the TTL have recently been presented, based on both trajectory calculations and CTMs to deduce characteristics of transport, such as transit timescales and pathways (*Fueglistaler et al.*, 2004; *Bonazzola and Haynes*, 2004; *Konopka et al.*, 2007; *Levine et al.*, 2007, 2008; *Krüger et al.*, 2008, 2009; *Kremser et al.*, 2009). Most of these studies were based on kinematic transport (*Fueglistaler et al.*, 2004; *Bonazzola and Haynes*, 2004; *Levine et al.*, 2007). However, recent analyses indicate that for diabatic transport the unrealistically high vertical dispersion due to the ω velocity is reduced (*Schoeberl et al.*, 2003) and the cold point sampling becomes more focused on regions of lower than tropical mean temperatures (*Krüger et al.*, 2008).

In this chapter, different vertical transport representations and their consequences for modelling transport in the TTL will be compared. Therefore, three-month backtrajectories are calculated in the TTL for boreal winter and summer 2002 in seven different transport representations (compare Tab. 3.1), five diabatic (clear-sky, all-sky, latent, diabatic, assim) and two kinematic (kinematic, kin-OP).

The main objective, namely the impact of the choice of transport representation on transport characteristics in the TTL, will be broken down into the following questions:

- *How is transport to the stratosphere affected by the various contributions to the diabatic heat budget (radiation, latent heat release)?*

- *How large are differences of transport characteristics in the TTL, in particular of pathways and timescales, between diabatic and kinematic transport?*

It will be investigated which modelled characteristics are sensitive, largely depending on the choice of the representation, and which emerge as a robust picture from all representations. Besides, the impact of a stronger or weaker tropical circulation on the composition of the TTL (vertically upwelling versus meridionally in-mixed air) and pathways of *troposphere-to-stratosphere transport* (TST) will be analysed.

4.1 Trajectory set-up

Backtrajectories are started on a $1° \times 1°$ horizontal grid between 30°S–30°N latitude and 0°–360° longitude on nine θ-levels in the vertical between 340 K and 420 K, with a vertical spacing of 10 K. Altogether, this yields a total of about 200 000 trajectories, which are started twice, on 1 March 2002 and on 30 August 2002, and calculated backwards for 90 days. Thus boreal winter (December, January, February, djf) and summer (June, July, August, jja) are both covered. The presented results are insensitive against slight variations of starting dates (one day/month earlier).

For the analysis of this chapter, the TTL is viewed laterally conf ned equatorwards ±30° equivalent latitude (approximately the tropical edge of the subtropical jet core) and only the subset of trajectories starting in this equivalent latitude range is considered (except for Fig. 4.6). Here, and throughout this work, equivalent latitude is def ned according to *Nash et al.* (1996). All presented results are insensitive with respect to slight variations of equivalent latitude bounds and with respect to replacing equivalent latitude by latitude bounds.

In this chapter the term *in-mixing* refers to trajectories entering the tropics from polewards ±30° equivalent latitude, irrespective of potential former crossings of these boundaries (different from irreversible mixing of air masses). The connection to in-mixing of air masses from the extratropical lowermost stratosphere into the TTL (see Sect. 2) will be discussed in Sect. 4.5.2.

4.2 Tropical upwelling

First, the tropical upwelling in the f ve diabatic transport representations is considered, to simplify the interpretation of the following results. Figure 4.1 shows prof les of the corresponding zonal mean tropical vertical velocities $\dot{\theta}$, annually averaged between ±10° latitude. The f gure is divided into a bottom (potential temperature range of 330–450 K) and a top part (450–2500 K) with different scalings of the x-axis to account for the range of magnitude of vertical velocity.

The most striking feature of the clear-sky velocity (black line) is its sharp decrease from 1.2 K/day to −1.8 K/day, crossing the zero baseline around 360 K, the LZRH. The effects of clouds and residual heating (blue and yellow lines) in the ERA-Interim dataset, respectively, displace this level to lower potential temperatures and reduce the negative values below and the positive values above, consistent with the results of *Fueglistaler and Fu* (2006). The combined effect of clouds and residual heating (total diabatic heating, red line) f nally yields a continuously positive vertical velocity.

A slight minimum of vertical velocity remains around a potential temperature level at about 350 K, between the top of the tropospheric Hadley and the lower end of the stratospheric Brewer-Dobson circulation. It remains to be shown whether this minimum is of physical origin or just an artefact of the ECMWF model. Furthermore, the assimilation increment weakens the sharpness of the minimum as it attenuates the upwelling above and amplif es the upwelling below.
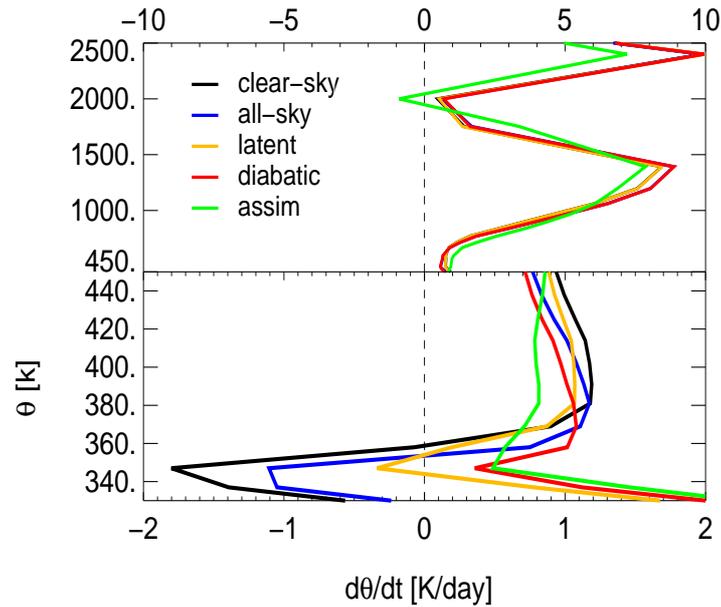
Figure 4.1: Annual mean tropical vertical velocity $\dot{\theta}$ (10°S–10°N latitude, 2002) for the different diabatic heating rates, inferred from ERA-Interim. The x- and y-axes in the top and bottom part of the panel are scaled differently. (Figure adapted from *Ploeger et al.*, 2010).

4.3 Transport into the TTL

There are two possibilities of entering the TTL, either across its vertical (from below: tropical troposphere; from above: stratospheric overworld) or across its meridional boundaries (extratropical lowermost stratosphere). To investigate these *gates to the TTL* in the various vertical transport representations, the TTL at starting time is considered as being composed of those trajectories, which are started in the range $360 \leq \theta \leq 400\,$K and between 30°S–30°N equivalent latitude (TTL trajectories). The fractions of TTL trajectories crossing a certain meridional or vertical boundary during the time of backward integration are calculated and referred to as *fractions of air* entering the TTL. To reduce the infuence of transient transport across the boundaries and the infuence of interpolation, TTL trajectories (or *air parcels*) are required to cross either the vertical boundaries 350 K/410 K, or the meridional boundaries $\pm 35°$ N (equivalent latitude) of a larger region to count for a particular fraction.

Figure 4.2 shows the probability density functions (PDFs) of the locations where the TTL trajectories crossed the boundaries of the larger region defned above. All distributions in this section are normalised to the total amount of trajectories initialised in the TTL. The plot in the middle of each panel in Fig. 4.2a displays the two-dimensional PDF for crossing the lower boundary of 350 K (the number of crossing events is binned in approximately $2° \times 6°$ latitude-longitude bins). The upper and lower plots of each panel show the one-dimensional PDFs for
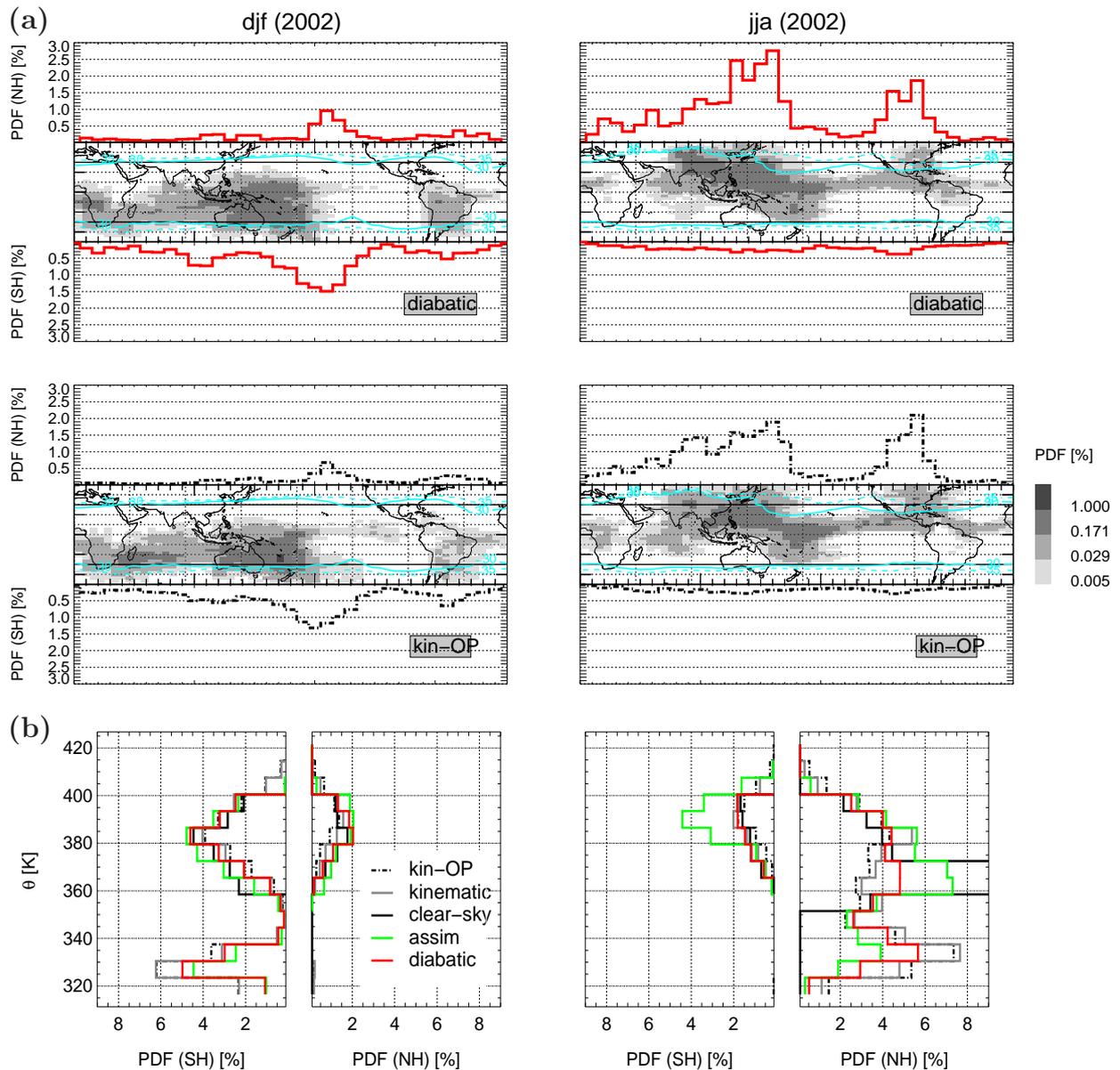
Figure 4.2: Vertical versus horizontal transport into the TTL for djf (left) and jja (right). (a) The grey colour scheme shows regions of vertical transport into the TTL (PDF of entry locations at 350 K; top: diabatic, bottom: kin-OP; note the nonlinear colour code). The thin solid black lines show the ±30° latitude, the solid/dashed cyan lines the ±30°/35° equivalent latitude contours, as averages in the 350–400 K layer for the respective period (djf, jja). The solid/dashed lines in the bottom and top parts of each panel describe PDFs of locations where the TTL trajectories crossed the meridional boundaries (±35° equivalent latitude), as functions of longitude. (b) PDFs of potential temperatures where the NH and SH meridional boundaries are crossed (the peak value for clear-sky/jja is 27.5%). All distributions are normalised to the total number of trajectories initialised in the TTL. (Figure adapted from *Ploeger et al.*, 2010).
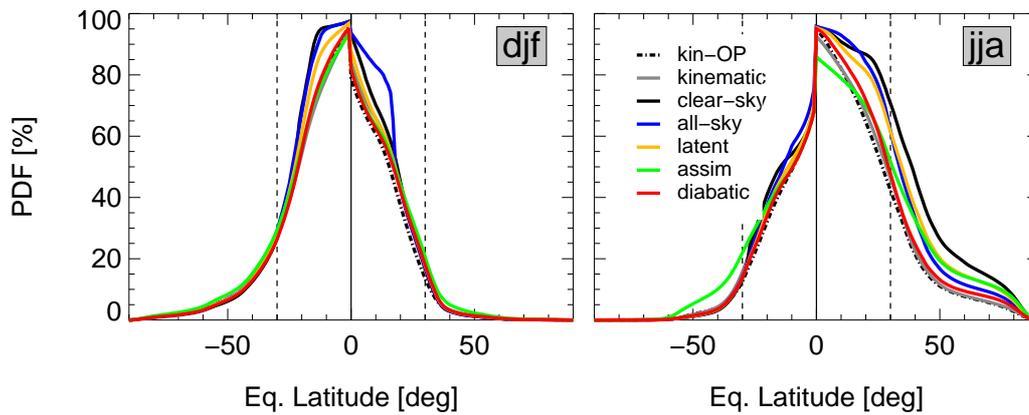
Figure 4.3: Fractions of trajectories started in the TTL, which reach regions polewards of a particular equivalent latitude (above 340 K) during winter (djf) and summer (jja). (Figure adapted from *Ploeger et al.*, 2010).

crossing the meridional boundaries, with a bin size of 10° longitude. Thus Fig. 4.2a allows vertical transport to be compared with horizontal transport into the TTL.

The effects on the locations of entry from below are less distinct (Fig. 4.2a, grey-shaded PDFs, underlaid with continents, in the middle of each panel). Nevertheless, there are differences. Thus for diabatic transport, in particular during boreal summer, the main entry region is located more to the north than for kinematic transport. In the latter cases, the peak of the distribution is more zonally symmetric. The specifc pattern with the main entry region above the Western Pacifc for boreal winter and displaced north-westward (above South China Sea/Indian Ocean/India) for boreal summer is left unaltered for all representations.

The shape of the distributions of the meridional entry locations is similar for the various representations (Fig. 4.2a, top/bottom of each panel). For all representations (only diabatic and kin-OP shown), the strongest meridional in-mixing occurs from the summer hemisphere extratropics above the Western/Central Pacifc and the Indian Ocean/India regions. For boreal summer, there is an increasing number of trajectories entering the TTL from the NH extratropics, which is even higher for diabatic than for kinematic transport. All summer distributions peak roughly at longitudes of the equatorial Western Pacifc/Northern India/Caribbean.

Figure 4.2b further elucidates the meridional in-mixing, showing the PDFs of potential temperatures of crossing the meridional boundaries. Irrespective of the transport representation, the main region of meridional in-mixing is located around 380 K. Below, the subtropical jets act as a transport barrier (strongest in the winter hemisphere, in particular during boreal summer) inhibiting exchange between tropics and extratropics (*Haynes and Shuckburgh*, 2000). Only during boreal summer, the transport barrier is less effcient and a large fraction of trajectories enters the TTL directly above the LZRH. The peak of the distribution is highest for the clear-sky representation with trajectories entering the TTL exclusively above the LZRH, at approximately 360 K.
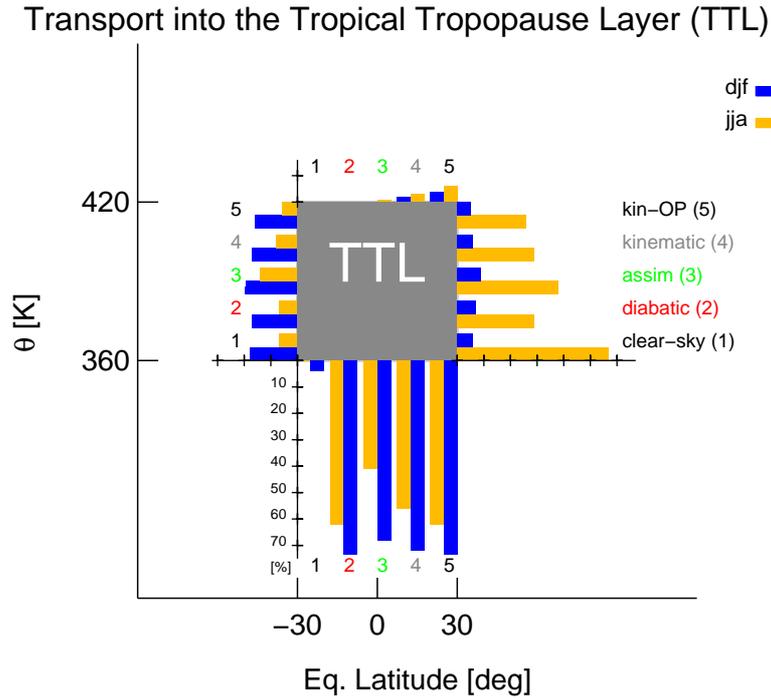
Figure 4.4: Fractions of trajectories entering the TTL across a particular vertical (from above, top; from below, bottom) or meridional (from NH, right; SH, left) boundary for boreal winter (blue) and summer (yellow) 2002. (Figure adapted from *Ploeger et al.*, 2010).

For the other diabatic and for the kinematic representations, the meridional in-mixing can happen below the LZRH as well.

Figure 4.3 shows how far the trajectories reach into the extratropics. The almost linear decrease of the fraction of TTL trajectories reaching regions polewards of a particular equivalent latitude shows that most in-mixed trajectories are only transported through subtropical regions (not reaching equivalent latitudes polewards of $\pm 50°$). But, in particular for boreal summer in the NH, many in-mixed trajectories (10–20%) are also transported through high-latitude regions.

The schematic of Fig. 4.4 shows the total fractions of trajectories entering the TTL across a certain boundary for boreal winter and summer 2002. It is evident that for clear-sky diabatic heating (clear-sky) no air enters from below the LZRH, but all from the extratropics. In this case, the negative vertical velocities below the LZRH constitute an impermeable vertical transport barrier. The fraction of trajectories entering the TTL from below increases for the all-sky and residual heating representation (about 70/35% for djf/jja, not shown) and even further for the diabatic, assim and the kinematic representation (about 75/60%). The sum of the four meridional and vertical fractions for each representation in Fig. 4.4 does not always yield 100% because a certain number of trajectories is not leaving the TTL during the three months of backward integration.

In the following, the four representations diabatic, assim, kinematic and kin-OP, which in-

volve the complete heating budget and therefore are assumed to represent the real atmosphere best, are compared in more detail. Using operational ω as vertical velocity, 21/32% of the air in the TTL enters from the extratropics for boreal winter/summer, while for interim ω these fractions increase to 23/36%, for total diabatic heating to 24/36% and for the assimilation increment representation even to 29/52%. For these four representations almost all the air in the TTL originates from outside its boundaries during three months, evident from the total of the fractions in Fig. 4.4, which almost always yields 100 percent.

Despite all the differences between the representations with respect to exact numbers, there are several properties common to all. First, for the four representations diabatic, assim, kinematic and kin-OP, there is a rather similar pattern of entry into the TTL across the vertical and meridional boundaries, respectively (Fig. 4.4). The in-mixed fraction from the extratropics is always larger for boreal summer (33-50%) than for boreal winter (approximately 25%). Second, in the summer hemisphere there is always a much larger fraction of air entering the TTL across the meridional boundary than in the respective winter hemisphere. The maximum difference between the two hemispheres arises during boreal summer, in particular above 360 K. Figure 4.4 shows more precisely that irrespective of the vertical velocity used there is at least twice as much meridional in-mixing from the summer than from the winter hemisphere. However, the absolute fractions vary, depending on the transport representation.

4.4 Transport across the TTL

The analysis of this section closely follows *Fueglistaler et al.* (2004). In particular, it will be shown how the different diabatic heating contributions cause transport from the level of the main convective outf ow to the stratosphere and determine the characteristics of the TTL as a transitional zone.

Figure 4.5a displays the fraction $f^{\leftarrow,400\text{K}}(\theta)$ of backtrajectories initialised at 400 K, which ascended from below θ during the f rst 60 days after release. In a hypothetical atmosphere with an impermeable transport barrier between troposphere and stratosphere, this curve should approximate to 1 above and 0 below the barrier. Obviously, the curve for clear-sky radiative heating (solid black) is very close to this idealised case, with the boundary exactly at the LZRH. Therefore, a large fraction of the air at 400 K ascended from around 360 K, but none from below, depicting the fact of negative vertical velocities below approximately 360 K (Fig. 4.1a). Figure 4.5a further indicates a slightly higher potential temperature of the LZRH for boreal summer compared to boreal winter.

The effects of clouds lower this level by 5–10 K. Residual heating (latent and mixing heating) yields enough upwelling to cause transport from the troposphere to the stratosphere, at least for boreal winter. The combined effect of clouds and residual heating f nally yields a transition zone, in which the amount of air reaching 400 K from below a certain potential temperature level
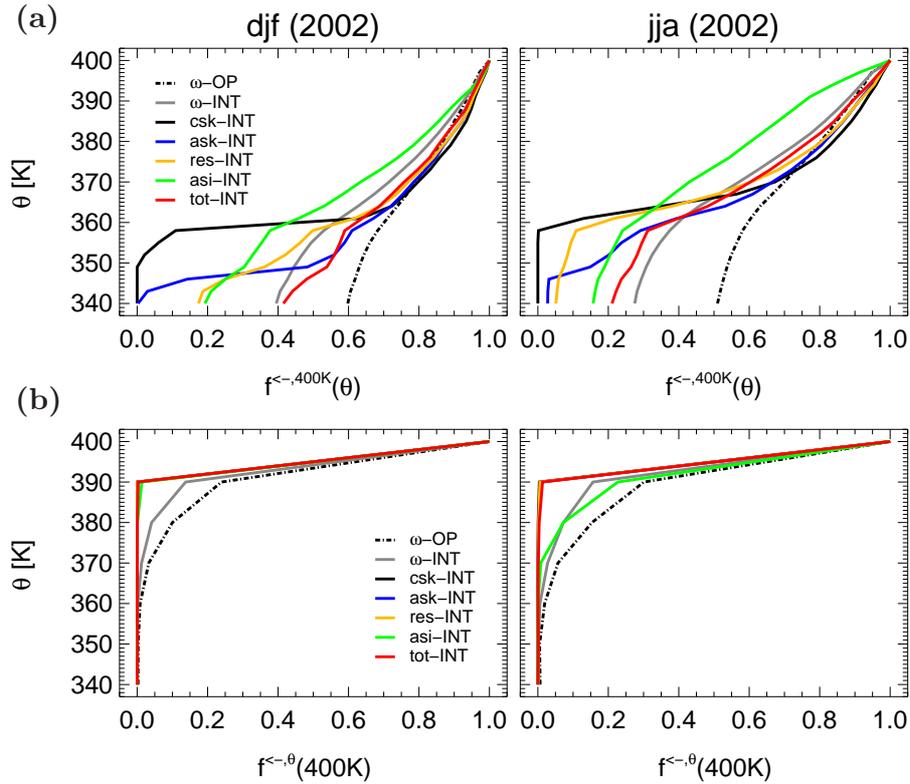
Figure 4.5: (a) Fractions $f^{\leftarrow,400K}(\theta)$ of backtrajectories starting at 400 K, which ascended from below θ during the f rst 60 days after release. (b) Fractions $f^{\leftarrow,\theta}(400K)$ of backtrajectories starting at θ, which descended from above 400 K, during the same period as in (a). Note that the other diabatic lines in (b) are covered by the diabatic (red) line. (Figure adapted from *Ploeger et al.*, 2010).

gradually increases as this level approaches 400 K, for both winter and summer.

For boreal winter as well as for summer, the tropical upwelling due to ω from operational ECMWF meteorological analysis is the strongest, with about 60/50% (for djf/jja) of the air at 400 K originating below 340 K during a period of 60 days (Fig. 4.5a). For total diabatic heating (red line) this fraction is reduced to about 40/20% for winter/summer. The ERA-Interim kinematic (solid grey) stays close to the diabatic (red) line from the same dataset. An interesting fact is the large discrepancy between diabatic and assim for boreal summer, indicating a strong impact of the assimilation increment.

Figure 4.5b further elucidates the impact of the assimilation increment. It displays the fraction of trajectories at a certain level, which descended from above 400 K during the previous 60 days. For boreal winter, the picture seems rather clear. For diabatic transport no air in the TTL below 400 K stems from above 400 K, even at the next lower level of 390 K. By contrast, for kinematic transport non-vanishing fractions of air ($\sim$25% at 390 K for kin-OP) originate at potential temperatures higher than 400 K. This property of subsidence was already mentioned by *Fueglistaler et al.* (2004) and is also evident in the assimilation increment representation (assim)
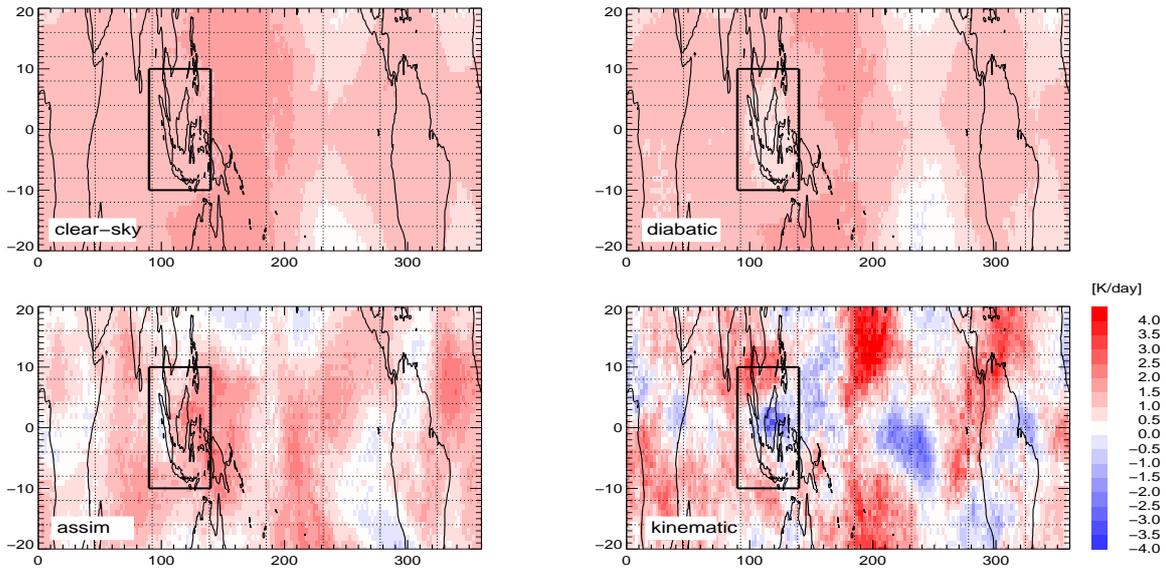
Figure 4.6: Mean cross-isentropic velocity $\dot{\theta}$ in the upper TTL (380–400 K) calculated from the cross-isentropic motion of the trajectories for NH winter (djf). The black rectangular depicts the maritime continent. (Figure adapted from *Ploeger et al.*, 2010).

for boreal summer. It will be discussed further in Sect. 4.5.1.

The reason for these rather different characteristics of air motion is hidden in the structure of the vertical velocity f elds. To elucidate this fact, average cross-isentropic velocity $\dot{\theta}$ is calculated along all the trajectories for the boreal winter ensemble between 380 K and 400 K. These net heating f elds are binned on a horizontal grid ($1° \times 1°$ latitude/longitude) and averaged over the three winter months (djf). Figure 4.6 depicts the net heating f elds and shows that they are very different for diabatic (clear-sky, diabatic) and kinematic transport (results in Fig. 4.6 are derived from all trajectories, without any equivalent latitude restriction). In a diabatic world there is almost no subsidence in the upper TTL (average $\dot{\theta}$ everywhere positive), while in a kinematic world subsidence frequently occurs. The assimilation increment yields a scenario in between, with regions of subsidence less distinct than for kinematic transport.

The picture for boreal summer changes only slightly (not shown). However, for assim the regions of subsidence increase for boreal summer (not shown), as expected from the fractions of descending trajectories at 390 K in Fig. 4.5b.

The property of subsidence in the TTL for kinematic transport also appears in the vertical dispersion of trajectories starting at 400 K in the (equivalent latitude/θ)-plane, displayed in Fig. 4.7 (similar to *Sparling et al.*, 1997, Fig. 2). For total diabatic transport the distribution of parcel locations is quite distinct, with the majority ascending from below through the lower and mid TTL. On the contrary, ω as vertical velocity leads to much higher vertical dispersion. The assimilation increment again yields a scenario in between.

The 'angel-shape' of the distribution in the two bottom panels of Fig. 4.7 for the two kine-
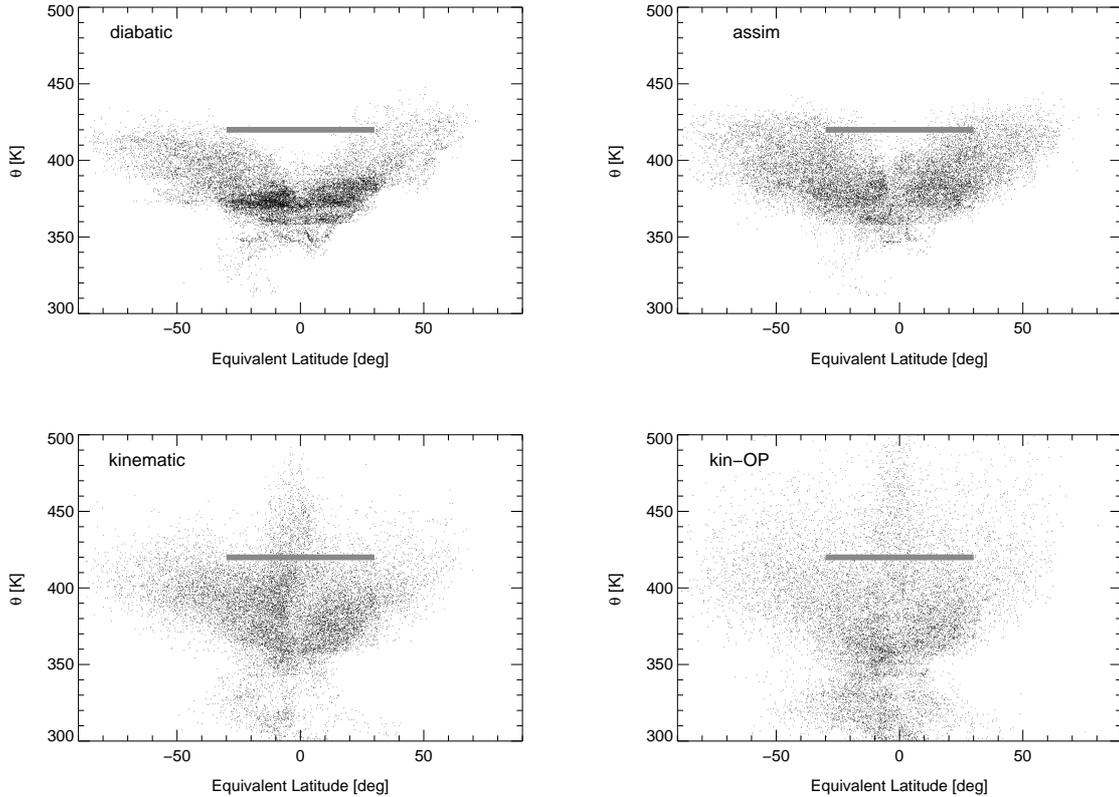
Figure 4.7: Vertical dispersion of trajectories, starting at 400 K, in the (equivalent latitude/θ)-plane after 45 days of backward integration for NH winter (djf). The grey bar displays the initialisation locations. The four scenarios diabatic, assim, kinematic and kin-OP are presented. (Figure adapted from *Ploeger et al.*, 2010).

matic representations conf rms the f nding of subsidence in Fig. 4.5b, with the trajectories located directly above their initialisation level in Fig. 4.7 subsiding to 400 K during the backward integration period.

4.4.1 Timescales of transport in the TTL

In Fig. 4.8 we consider residence times Δt_{res} for trajectories in a layer around a particular potential temperature θ. These residence times are computed by averaging the durations for leaving the layer [θ-10 K,θ+10 K] over the ensemble of trajectories initialised at θ, as was done by *Fueglistaler et al.* (2004). Figure 4.8 shows that operational ω (kin-OP) yields residence times very similar to the residence times of *Fueglistaler et al.* (2004).

A comparison of the all-sky and clear-sky lines shows that the radiative effects of clouds accelerate the upwelling below 380 K (heating in cloud layer) and retard it above (cooling above cloud layer), in agreement with *Fueglistaler and Fu* (2006). Nevertheless, for clear-sky radiative
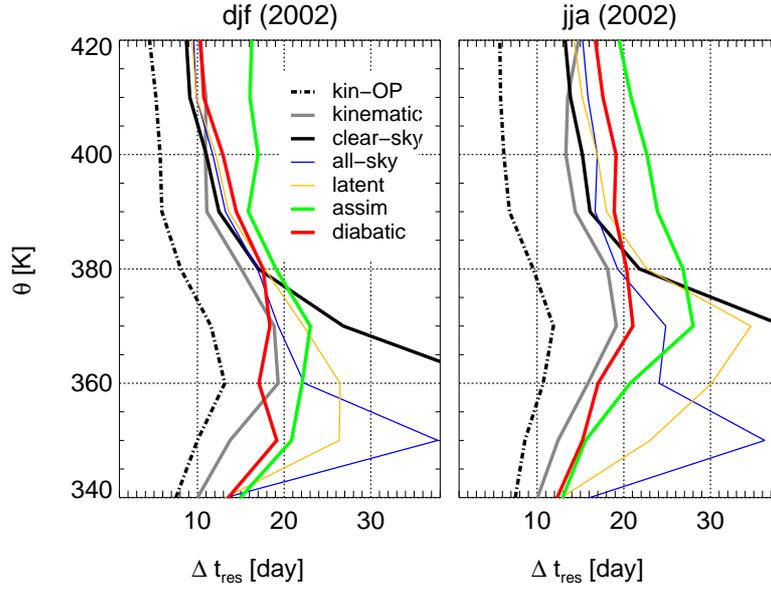
Figure 4.8: Mean residence time Δt_{res} of trajectories for staying in the $\theta \pm 10$ K layer. (Figure adapted from *Ploeger et al.*, 2010).

heating rates with either the addition of cloud effects or latent and mixing heating the ascent below 380 K remains very slow. However, the combined effect of clouds, latent and mixing heating yields residence times which are comparable to the ERA-Interim kinematic case (kinematic). Overall, residence times per 10 K for the interim total diabatic are 2-5 days longer than for the kinematic representation. The operational kinematic data exhibits the strongest tropical upwelling with shortest residence time. The effects of the assimilation increment are larger during boreal summer compared to winter, attenuating the upwelling mainly above about 360 K.

A different way to quantify transport timescales is to consider the full age distribution of trajectories. In the theory of age spectra (*Hall and Plumb*, 1994; *Waugh and Hall*, 2002), the term age corresponds to the transit time of an air parcel between two locations and age spectrum to the distribution of these ages within a given volume of air.

Transit time distributions for boreal winter for transport from 340 to 400 K (from trajectories initialised at 400 K) are presented in the top panel of Fig. 4.9. Operational kinematic transport yields a much larger number of rapidly ascending trajectories than ERA-Interim kinematic transport. Moreover, the ascent due to total diabatic heating turns out to be much slower, with the fastest trajectories lagging behind the fastest kinematic ones by $\sim$20 days.

The mean timescales for ascent from the troposphere to the stratospheric overworld are given in Tab. 4.1 as the mean ages. As noted already, the kin-OP representation yields the fastest transport to the overworld with a mean age $\overline{\Delta t}_{400 \leftarrow 340} = 33/33$ days for djf/jja. The respective timescales for kinematic and diabatic ERA-Interim transport are up to a month longer. For boreal summer (jja) in the interim representations, there are many less rapidly transported trajectories
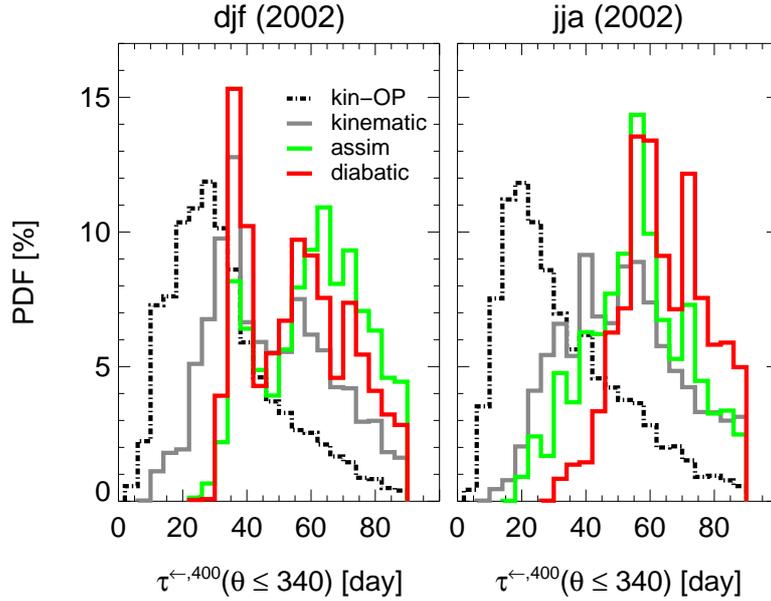
Figure 4.9: Transit time distributions at 400 K for the upward transport from 340 K. The bin size is 4 days. (Figure adapted from *Ploeger et al.*, 2010).

Table 4.1: Mean transit times for ascent across the TTL, in days (the notation is djf/jja)

	clear-sky	all-sky	latent	diabatic	assim	kinematic	kin-OP
$\overline{\Delta t}_{400 \leftarrow 340}$	-/-	77/71	64/68	56/64	61/56	47/51	33/33
$\overline{\Delta t}_{400 \leftarrow 370}$	32/42	33/42	35/46	36/46	39/37	26/33	16/17

than for winter (djf), whereas the distribution for operational data changes only slightly.

Further, the effect of adding the assimilation increment to the diabatic heating appears to be contrary in the two seasons. During boreal winter the assimilation increment reduces the amount of fast trajectories, while during summer it accelerates the fastest ones even more (bottom panel of Fig. 4.9).

There is still another difference between the transit time distributions for kinematic and diabatic transport. While for kin-OP the distribution for djf has one broad peak at short times (25 days), the diabatic distribution surprisingly shows a two-peak shape (f rst peak at ∼35, second peak at ∼60 days) indicating two separate transport pathways. The second peak can also be seen for kinematic, albeit less distinctly, and will be discussed in Sect. 4.5.1.

It should be noted that transport timescales from trajectories with a f nite integration length are always low biased, i.e. transport seems too fast. The bias arises, because trajectories with transport times longer than the integration time are not taken into account.

4.5 Discussion: Sensitive and robust transport characteristics

Transport characteristics are classif ed into either *sensitive* or *robust* with respect to the transport representation, in Tab. 4.2. Sensitive characteristics crucially depend on the choice of the transport representation. Robust characteristics, on the contrary, emerge as a robust picture, irrespective of the representation.

4.5.1 Sensitive characteristics

Subsidence in the TTL

It was suggested by *Sherwood* (2000) that air which detrains from overshooting convective turrets subsides in the region above deep convective systems. The rise into the stratosphere consequently occurs at different locations. The most important region of subsidence, the 'stratospheric drain' region, was found above the maritime continent, with positive pressure tendencies along the 85 hPa isobar, corresponding to downward motion (*Sherwood*, 2000). *Fueglistaler et al.* (2004) extended the analysis of *Sherwood* (2000), *Simmons et al.* (1999) and *Hatsushika and Yamazaki* (2003) of the vertical ω-wind f elds at the 85 hPa and 90 hPa pressure surfaces and considered changes in potential temperature along kinematic trajectories. The trajectory study of *Fueglistaler et al.* (2004), with ω taken from ECMWF analysis, also showed subsidence across isentropes above the maritime continent.

Following the line of argument of *Fueglistaler et al.* (2004), the existence of a region of subsidence in the upper TTL is found to be extremely sensitive to the chosen diabatic or kinematic representation. Figure 4.6 shows that diabatic heating processes yield a mean vertical velocity f eld, which varies in the zonal and meridional directions, but remains nonnegative throughout the range of the TTL. The local minimum in the total diabatic upward velocity above the maritime continent (black rectangle in Fig. 4.6) appears as a region of negative (downward) cross-isentropic velocity for kinematic transport, consistent with *Fueglistaler et al.* (2004). Thus, while in a diabatic world there is no mean subsidence in the upper TTL, in a kinematic world regions of mean subsidence occur. The assimilation increment also shows this subsidence, albeit much less pronounced. Therefore, within the framework of ERA-Interim the variability in the pressure tendency wind f eld cannot be traced back to structures in diabatic heating.

The consideration of the spread around the mean $\dot{\theta}$-values in each horizontal grid box of Fig. 4.6 (not shown) reveals that for kinematic and assim transport the standard deviation is similar to the mean values. For clear-sky and diabatic the standard deviation is much lower.

Furthermore, none of the transport representations contradicts the f nding of *Folkins et al.* (1999), who reported on air masses in the TTL originating from the lower stratosphere. There is only the open question, whether this air descended from the stratospheric overworld or was

Table 4.2: Sensitive versus robust characteristics of transport in the TTL with respect to the (diabatic versus kinematic) vertical transport representation

sensitive	robust
Subsidence maritime continent 'stratospheric drain'	**In-mixing** winter/summer: ~25/33-50%
Vertical dispersion	**Hemispheric asymmetry** max. in-mixing from summer hemisphere
Residence times	
Pathways trop. easterlies vs. subtrop. westerlies travelled hor. distance	**'Gates to the TTL'** vertical: W. Pac., S. China Sea, N. India meridional: W. Pac., N. India
	Residence time enhancement between 350–380 K

quasi-isentropically in-mixed from the extratropical lowermost stratosphere, which is answered differently for different vertical transport representations. Subsidence above the maritime continent will be further discussed in Sect. 5.4.3, with respect to ozone measurements and simulations.

Vertical Dispersion

Sparling et al. (1997) argued, that air parcels starting on a particular isentropic surface experience different time histories of diabatic heating, causing vertical diabatic trajectory dispersion across isentropic surfaces.

The consideration of trajectory dispersion in Fig. 4.7 confrms the occurrence of subsidence for kinematic transport. The fgure shows that only for kinematic transport and for assim there are trajectories localised above their initial θ-level after 60 days of backward integration. For kinematic transport the trajectory ensemble is less compact with much higher vertical dispersion than for diabatic transport, in agreement with *Schoeberl et al.* (2003). The dispersive characteristics of the assimilation increment representation are in between. From the two bottom panels of Fig. 4.7, a reduction of vertical dispersion for the interim compared to the operational ω-winds is evident, consistent with the results of *Monge-Sanz et al.* (2007).

Sparling et al. (1997) suggested potential temperature variance of trajectories at time t

$$\langle \delta\theta^2 \rangle = \langle (\theta(t) - \langle \theta(t) \rangle)^2 \rangle \tag{4.1}$$

as a measure to quantify diabatic cross-isentropic dispersion of the trajectory ensemble. Here, angle brackets denote the mean over the ensemble of trajectories. Potential temperature variance $\langle \delta\theta^2 \rangle$ measures the vertical spread of the trajectory ensemble at time t. In the remainder of this
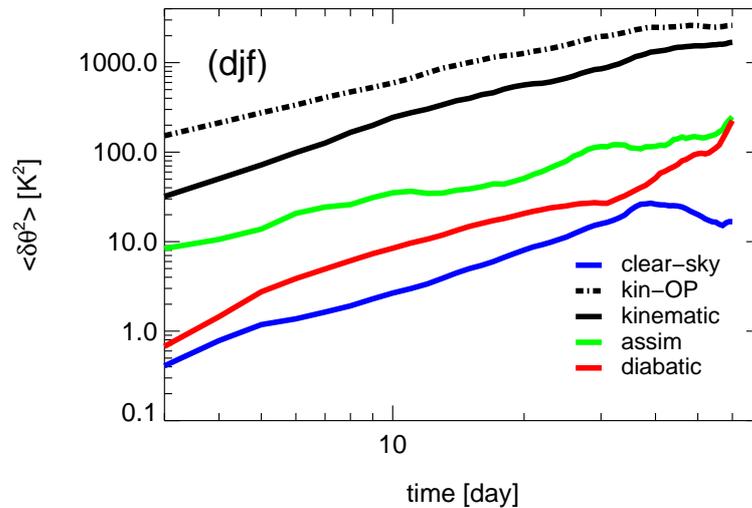
Figure 4.10: Time evolution of potential temperature variance $\langle \delta\theta^2 \rangle$ for djf tropical trajectories, not leaving $\pm 30°$ equivalent latitude.

work, the term dispersion always refers to vertical dispersion, quantified by potential temperature variance $\langle \delta\theta^2 \rangle$.

Figure 4.10 shows the time evolution of vertical dispersion $\langle \delta\theta^2 \rangle$. Dispersion is highest for the two kinematic representations during the whole period (for kin-OP even much higher than for kinematic) and about two orders of magnitude lower for the diabatic representations clear-sky and diabatic. The dispersive characteristics of the assimilation increment are in between, with vertical dispersion still almost one order of magnitude higher than for total diabatic heating.

Timescales

The speed of upward transport to the stratospheric overworld is a major determinant for propagation of tape-recorder signals (compare e.g., *Mote et al.*, 1996). Moreover, corresponding transport timescales and pathways are crucial for determining the amount of very short-lived substances (VSLS) and other trace gases in the stratosphere. *Levine et al.* (2007, 2008) emphasised that VSLS easily reach the extratropical regions of the stratosphere, when being meridionally transported out of the tropics. Below, it will be pointed out that modelling of these processes depends on the vertical transport representation.

The most striking difference when comparing the kinematic and diabatic approaches is the stronger tropical upwelling for kinematic transport, resulting in shorter residence times (Fig. 4.8 and Tab. 4.1) and larger fractions of backtrajectories ascending from lower potential temperatures (Fig. 4.5). The fastest upwelling results for operational ω. Upwelling due to ERA-Interim ω is weaker and not much stronger than for total diabatic heating. Consistent with a weaker tropical upwelling there is a smaller fraction of air entering the TTL directly from below (from the

tropical troposphere), but a larger fraction which is meridionally in-mixed from the extratropics (Fig. 4.4).

The weaker ascent of air in the tropics for diabatic transport is also ref ected in the distribution of transit times from below the TTL to its upper part, in Fig. 4.9. The time for ascent from 340 K to 400 K for total diabatic heating equals approximately two months (56/64 days for djf/jja) and is therefore about 10 days longer than for ERA-interim and about one month longer than for operational ECMWF kinematic transport. These large differences in transit timescales are likely to inf uence the results of modelling transport and chemistry of VSLS and other species.

Moreover, Tab. 4.1 reveals that heating rates for assim result in a faster circulation for boreal summer than for winter. Thus the assimilation increment results in an inverted seasonality of upwelling, compared to the other representations.

Concerning the formation of the head of the tape recorder, the timescale for ascending from the Lagrangian cold point (the minimum temperature along the trajectories) around 370 K to the stratospheric overworld is crucial. Table 4.1 shows that for ω from ERA-Interim or the total diabatic heating rate as vertical velocity, the respective timescale is more than twice as long as for operational ω.

Thus, differences in transport timescales due to the choice of vertical winds are large enough to dwarf differences between seasons, regions and different years (compare e.g., *Krüger et al.*, 2009).

Pathways

To further illustrate the evolution of the two-peak structure in the transit time distribution in Fig. 4.9, the transit time distribution is calculated separately for trajectories travelling with the subtropical westerly jet and for the remaining trajectories, for the total diabatic representation for djf.

Analogously to the analysis of *Fueglistaler et al.* (2004), trajectories with a maximum net zonal displacement during integration time of at least $\Delta\lambda = 180°\,\text{E}$ are regarded as travelling with the strong westerly jets. Of course, this separation is not perfect, as it does not account for different pathways of trajectories with $\Delta\lambda < 180°\,\text{E}$, which can be eastward or westward travelling or conf ned to large anticyclonic systems (e.g., monsoons). However, even this simplif ed separation will provide a rather clear picture of which pathways contribute to which peak.

Figure 4.11 shows that trajectories with $\Delta\lambda < 180°\,\text{E}$ (tropical easterlies; thin solid orange line) mainly contribute to the fast and trajectories with $\Delta\lambda \geq 180°\,\text{E}$ (subtropical westerlies; thin dash-dotted orange line) mainly to the second slower peak. A comparison of the horizontal distances travelled reveals large differences. On average, westward displaced trajectories travel a horizontal distance of 44 000 km, while eastward displaced trajectories (about 46% of all trajectories) almost twice as far (83 000 km). For the operational kinematic representation, eastward displaced westerly jet trajectories (35%) travel on average 65 000 km and the remaining trajecto-
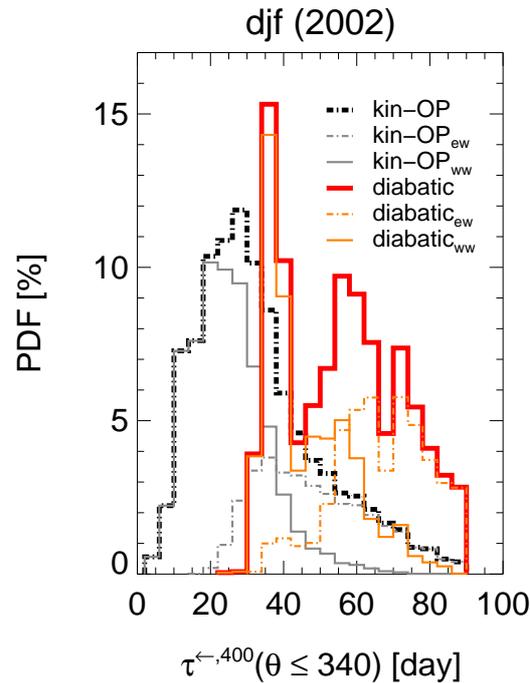
Figure 4.11: Formation of the two-peak shape of the transit time distribution of parcels at 400 K for ascending from 340 K. The thin grey and orange solid/dash-dotted lines denote the transit time distributions for net westward/eastward travelling trajectories. The bin size is 4 days. (Figure adapted from *Ploeger et al.*, 2010).

ries about 24 000 km and hence much shorter distances.

The f rst (fast) pathway across the TTL can be characterised as being tropically conf ned to the domains of fastest upwelling, with only small meridional and westward zonal displacements, mainly due to the tropical easterlies. Air which takes the second pathway rapidly ascends to ~ 350 K, where the ascent slows down because of a distinct minimum in upward velocity (enhanced residence times). Due to the slower ascent, the upwelling air is exposed to meridional drifts for a longer time and easily reaches the regions of the subtropical jets. The strong eastward horizontal f ow of the jet stream displaces the air masses very far outside the regions of fastest upwelling, resulting in even slower ascent and farther displacement. On their way to the stratospheric overworld they frequently enter the extratropics, in agreement with the results of *Levine et al.* (2007, 2008). However, parts of these air masses again enter the tropics at higher potential temperature levels and signif cantly contribute to the composition of the upper TTL. Though this second pathway is less evident in the transit time distribution of the stronger kinematic upwelling, for the slower upwelling of diabatic transport it gains in importance.

Hence, the partitioning of ascending air between different pathways in the TTL and consequently the travelled horizontal distance turns out to be extremely sensitive to the choice of the vertical transport representation.

4.5.2 Robust characteristics

Residence time enhancement

Figure 4.8 shows a large sensitivity of residence times in the TTL to the choice of the vertical transport representation, as discussed in Sect. 4.5.1. But a closer look reveals an enhancement of residence times in the layer between 350–380 K compared to layers above and below, which robustly emerges from all transport representations.

Below about 350 K upwelling is mainly due to convection, above about 380 K due to the Brewer-Dobson circulation. In the coupling region in between, the ascent slows down for all representations, resulting in residence times more than twice as long as below 350 K and above 380 K.

Gates to the TTL

The regions where air enters the TTL are very similar for the different transport representations and coincide with results from earlier studies (*Chen*, 1995; *Fueglistaler et al.*, 2004). The main vertical entry regions (across the lower TTL boundary, here 350 K) are located above the Western Pacif c for boreal winter and are displaced north-westward above the equatorial Western Pacif c, the South China Sea and Northern India for summer.

The in-mixed trajectories enter the TTL essentially at longitudes where the f ow due to the two quasi-stationary anticyclones above the Western Pacif c for boreal winter and due to the Asian/American monsoons for boreal summer is directed towards the equator (compare e.g., *Fueglistaler et al.*, 2009a, Fig. 5a).

In-mixing and hemispheric asymmetry

In-mixing from polewards of the $\pm 35°$ equivalent latitude band turns out to be an important pathway into the TTL (compare also *Konopka et al.*, 2009), irrespective of the vertical transport representation. For the four most realistic transport representations (diabatic, assim, kinematic, kin-OP), robustly about 25/33-50 % of trajectories in the TTL are in-mixed across the meridional boundaries for boreal winter/summer.

Furthermore, the hemispheric asymmetry of in-mixing, with usually more than twice as much in-mixing from the summer than from the winter hemisphere, is not dependent on the choice of the transport representation. The maximum discrepancy between the summer and winter hemisphere robustly arises for boreal summer. Irrespective of the representation, the hemispheric asymmetry of in-mixing is likely due to the strong Asian monsoon anticyclone (*Dunkerton*, 1995; *Gettelman et al.*, 2004b; *Randel and Park*, 2006), as the main in-mixing occurs for boreal summer in regions of equatorward f ow of the anticyclonic circulation (as explained in Sect. 4.5.2), in agreement with *Chen* (1995).

We term the trajectories meridionally entering the TTL from polewards $\pm 35°$ equivalent latitude in-mixed, irrespective of how far they reach into the extratropics (Fig. 4.3 provides this additional information). Hence, the ensemble of in-mixed trajectories consists of trajectories which reach deeply into the extratropical stratosphere as well as of trajectories, which are only transported through the subtropical jet core and might originate in the troposphere three months before. Even the latter encounter regions of strong mixing in the subtropical jets (*Pan et al.*, 2006) and in the real atmosphere are very likely to transport extratropical stratospheric air into the TTL. However, even if the large in-mixed fractions of 25/33-50% do not represent air masses from deep extratropical lowermost stratosphere regions, they emphasise the great importance of the subtropical jets as pathways for transport to the tropical stratospheric overworld. For a quantitative estimation of the impact of extratropical in-mixed air on the composition of the TTL, CTM studies must be employed.

Furthermore, it would be interesting to study the pattern of in-mixing by using a time-varying tropopause criterion, motivated by the work of *Haynes and Shuckburgh* (2000). As the presented analysis focusses on the sensitivity of transport study results (to the transport representation), a constant equivalent latitude value is considered to be adequate, because most studies employ a constant PV or equivalent latitude criterion to separate troposphere and stratosphere.

4.6 Chapter conclusions

Backtrajectories were started in the TTL, using different kinematic and diabatic transport representations to analyse the impact of the transport representation on transport characteristics. The results show that all contributions to the diabatic heating budget (effects due to radiation with clouds and due to latent heat release, mixing and diffusive heating) are necessary for modelling transport from the troposphere to above the LZRH. Thus, either clear-sky or all-sky radiative heating alone as diabatic heating rate misses very important processes.

Transport characteristics which sensitively depend on the choice of the transport representation are classif ed as sensitive, characteristics emerging as a robust picture from all representations as robust. A f rst sensitive characteristic is the residence time in the TTL. Kinematic transport from operational ECMWF data yields the fastest tropical upwelling and the shortest mean transit times from 340 K to 400 K of about a month. For kinematic and total diabatic transport from ERA-Interim these timescales are found to be one month longer and for all-sky diabatic and residual heating transport even longer.

Furthermore, there are differences in the pathways to the stratospheric overworld between the different representations. For kinematic transport, regions of mean downward cross-isentropic motion occur in the upper TTL (in particular above the maritime continent), while for diabatic transport air rises uniformly throughout the entire range of the TTL. The addition of assimilation increments to the total diabatic heating rate yields transport with frequent regions of mean

downward cross-isentropic motion, closer to kinematic than to diabatic transport.

For stronger upwelling (here, operational kinematic transport) rising air is mainly tropically confned to the regions of fastest ascent. For the weaker upwelling of ERA-Interim, trajectories are more likely to reach the regions of the subtropical jets and thus travel large horizontal distances before again entering the tropics above the jet core. Consequently, the travelled horizontal distance is crucially impacted by the choice of the transport representation.

A robust characteristic is the enhancement of residence time in the lower TTL, between about 350–380 K, irrespective of the transport representation. Furthermore, for all representations a large fraction of trajectories in the TTL is meridionally in-mixed into the TTL across the meridional boundaries, indicating the importance of the subtropical jets as pathways for TST and a potentially large impact of transport from the extratropical lowermost stratosphere on trace gas budgets in the TTL. Also the pronounced hemispheric asymmetry of meridional in-mixing, with enhanced in-mixing from the summer hemisphere (maximum for boreal summer), appears unaffected by the vertical transport representation.

Results from trajectory studies concerning sensitive transport characteristics are to be handled with care, as they are strongly sensitive to uncertainties arising from the method. Results referring to robust characteristics, on the contrary, are less infuenced by the method. Regarding results of transport studies in the TTL, there is a much greater reliability in robust patterns of transport than in exact numbers.

As long as the 'true velocity' of the atmosphere is unknown and provided meteorological data involves uncertainties, the results of this chapter provide a guideline for estimating the sensitivity of transport characteristics due to the choice of the vertical transport representation.

5 Insight from ozone and water vapour on transport in the TTL

The results of the previous chapter demonstrate that the choice of the vertical transport representation (diabatic versus kinematic) has a signif cant impact on certain characteristics of transport in the TTL (e.g., subsidence, dispersion). Throughout this chapter, the impact of the choice of the transport representation on simulating water vapour and ozone distributions in the TTL will be analysed. There are crucial implications regarding the validation of transport in models (CCMs, GCMs), as model transport is generally validated by comparing trace gas simulations to observations. To study the impact of differences in model transport on predicted tracer f elds, water vapour and ozone concentrations are predicted using two different vertical transport representations (diabatic and kinematic ERA-Interim, compare Tab. 3.1).

The specif c questions of this chapter can be summarised as follows:

- *Can ozone in the upper TTL be predicted by photochemical production and transport based on trajectories, and how does the quality of the prediction compare with results for water vapour?*

- *Which processes control upper TTL ozone concentrations in the model calculations?*

- *What can be learnt from ozone and water vapour predictions regarding transport in the TTL?*

- *What is the impact of diabatic versus kinematic transport on water vapour and ozone predictions?*

5.1 Backtrajectory prediction of water vapour and ozone

In the following, mean TTL concentrations from HALOE, as well as in-situ observations from the tropical SCOUT-O3 campaign (*Brunner et al.*, 2009), for water vapour and ozone will be predicted from backtrajectories. For the prediction of mean TTL concentrations, backtrajectories are started on the 15th day of each month of the year 2002 in the tropical lower stratosphere
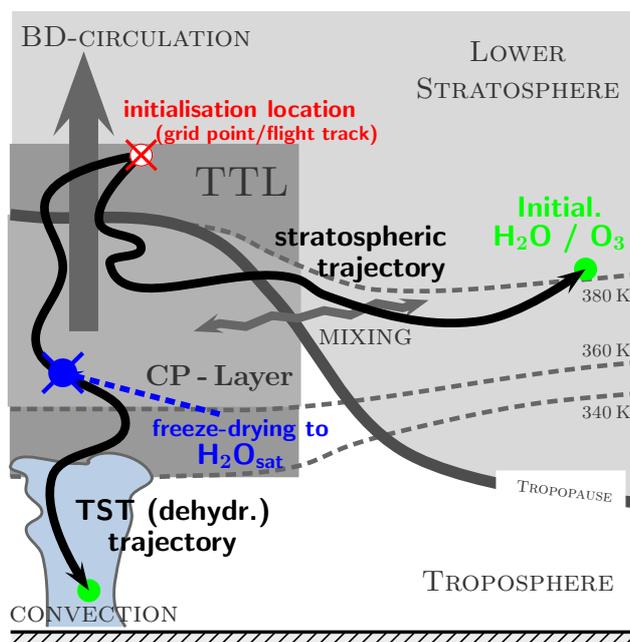
Figure 5.1: Schematic of method (see text). The f gure shows troposphere-to-stratosphere transport (TST trajectories) and purely stratospheric trajectories. The upwelling branch of the stratospheric Brewer-Dobson (BD) circulation is displayed as a thick grey arrow, horizontal (quasi-isentropic) stratosphere-troposphere exchange as a grey wavy arrow, particular isentropes as thin grey dashed, the tropopause as a grey solid line. The Cold Point (CP) layer between 360 and 380 K is coloured light grey. The black arrows characterising the typical backtrajectories point backwards in time. The blue dot illustrates the location where dehydration to the local minimum saturation water vapour mixing ratio (H_2O_{sat}) occurs along the TST backtrajectory. Green dots illustrate the initialisation of backtrajectories with ECMWF (HALOE) water vapour and ozone at the end points. (Figure adapted from *Ploeger et al.*, 2011).

on the 400 K potential temperature level on a regular grid with $1° \times 1°$ latitude/longitude spacing, between $\pm 20°$ latitude, and are integrated backwards in time for 90 days. For the comparison with in-situ measurements, the trajectories are started along the research aircraft (M55 Geophysica) f ight tracks every second and are integrated backwards in time for 60 days. All observations of both local and transfer f ights equatorwards of $\pm 20°$ latitude are included in the analysis, except for the two f ights on 30 November 2005 (11 f ights in total) when a single deep convective storm was repeatedly probed.

Sensitivity to the length of the integration period has been evaluated by comparing results obtained from f ve-month integration for the global f elds, and 90 days for the comparison with in-situ measurements. In the following, results and conclusions are shown only for those aspects of the calculations that are insensitive to trajectory length.

In order to facilitate interpretation of results, we group the model predictions of water vapour and ozone according to the pathway of the trajectories, as illustrated in Fig. 5.1. The separation

criterion is the minimum potential temperature encountered along the trajectory. The ensemble of trajectories that can be traced back to below 350 K potential temperature is called the *troposphere-to-stratosphere transport* (TST) ensemble (*Fueglistaler et al.*, 2004), the remainder the *stratospheric* ensemble. This separation proves useful because for the TST ensemble both water vapour and ozone are largely independent of initial conditions. That is, water vapour for TST is given by the minimum saturation mixing ratio. For ozone, the integrated production along trajectories is of the same order of magnitude as the initialisation ozone mixing ratio. Conversely, the tracer predictions of the non-TST ensemble strongly reflect initial conditions. That is, the minimum saturation mixing ratio encountered along trajectories that stay in the stratosphere is often 30% and higher (see below) than the initialisation value for water vapour, and hence the predicted value is the initialisation value. For ozone, production along the path of the non-TST ensemble does play a role, but because of the generally much larger ozone concentrations in the stratosphere than in the troposphere, the initial concentration often dominates the predicted concentrations.

5.1.1 Water vapour model

Water vapour in the TTL is predicted (at the end point, in forward-time, of the trajectories) based on the minimum saturation mixing ratio encountered along the trajectory. It is known that stratospheric water vapour predictions based on the minimum saturation mixing ratio from ERA-Interim data are drier than observed (*James et al.*, 2008; *Liu et al.*, 2010). Following the approach of *James et al.* (2008), a 'nucleation barrier' of 130% relative humidity is introduced. This nucleation barrier is well within the uncertainties of ice nucleation, and supersaturation with respect to ice is frequently observed (e.g., *Krämer et al.*, 2009). But the point emphasised here is simply to achieve better agreement with measurements, without any claim about cloud microphysical aspects. The effect of a higher nucleation barrier in the model is that less trajectories become dehydrated and hence more water vapour enters the stratosphere. Increasing tropical tropopause temperatures would have the same net effect. It is therefore possible, that the particular nucleation barrier value compensates for a slight cold bias in the ERA-Interim temperatures, rather than representing the nucleation barrier in the real atmosphere. A slight cold bias of ERA-Interim tropical temperatures at 100 hPa was found by *Liu et al.* (2010), from comparison with radiosonde temperatures.

The trajectories are initialised with ERA-Interim water vapour mixing ratios. Model results for TST trajectories are independent of this initialisation, but for the stratospheric ensemble, relative humidity along the trajectory frequently stays below 130%, such that the predicted water vapour for this ensemble essentially reflects initial conditions. Model results are interpreted only in terms of differences between the two trajectory methods.

5.1.2 Ozone model

For ozone, backtrajectory concentrations are predicted by initialising with ozone mixing ratios from ERA-Interim (for TST trajectories, the value at 360 K potential temperature is taken), and subsequent integration of photochemical production due to oxygen photolysis (see *Avallone and Prather*, 1996) and loss through HO_x radicals (see e.g., *Osterman et al.*, 1997). For the photolysis calculation with the CLaMS photolysis scheme (*Meier et al.*, 1982; *Becker et al.*, 2000), a climatological ozone field (*Grooß and Russell*, 2005), based on measurements from HALOE is used as background, and the HO_x fields are taken from a model (CLaMS) based climatology. All calculations shown here include the loss from reaction with HO_x (reactions (R9/10) in Tab. 7.1), but in App. B it is shown that neglecting the loss process would not change results significantly.

This simple ozone model captures the most important chemical processes controlling ozone in the tropical lower stratosphere and around tropopause levels, but not further below in the troposphere.

For those trajectories that cannot be traced back to the troposphere and which are initialised with stratospheric ozone concentrations, the initial value is often larger than the integrated production. As such, results are sensitive to initial conditions. The sensitivity to ozone initial conditions is evaluated with a calculation where a zonal mean HALOE ozone climatology (further detailed in Sect. 5.1.3), instead of the ERA-Interim ozone field, is used for initialisation. In the region of interest, ERA-Interim ozone concentrations are generally higher compared to the HALOE climatology and results based on the two initialisations yield a corresponding offset. Differences will be discussed in detail but, similarly to the case of water vapour, the emphasis here is on *differences* in model predicted ozone between the two trajectory calculations, and these differences are robust to variations in initial conditions.

5.1.3 Observations

Model predictions for water vapour and ozone are compared against observations from different sensors and platforms. For the reconstructions of tropical mean fields and profiles, the model predictions are compared with observations from the Halogen Occultation Experiment (HALOE, version 19 data) (*Russell et al.*, 1993). HALOE measurements of water vapour and ozone are binned into zonal mean, monthly means averaged over the period 2001–2005, using the method of *Grooß and Russell* (2005). For comparison with 'tropical mean' profiles and time series, data are averages between 20°S–20°N in latitude. For the sensitivity calculation with respect to initial conditions, the HALOE data is binned on a regular grid in equivalent latitude (grid spacing of 15°).

For ozone, measurements from SHADOZ, the Southern Hemisphere Additional Ozone network (*Thompson et al.*, 2007), are shown in addition, where a subset of seven stations as defined in *Randel et al.* (2007) was used to construct a 'tropical mean' profile.

For the comparison with in-situ measurements, total water measurements of the Fast In-Situ Hygrometer (FISH) (*Zöger et al.*, 1999) and O$_3$ measurements from the Fast OZone ANalyser (FOZAN) (*Ulanosvky et al.*, 2001) obtained during the SCOUT-tropical campaign (as explained above) are used. Further, a 'typical' prof le of water vapour and ozone was calculated from HALOE data for the period and region covered by the SCOUT-tropical campaign. To this end, all HALOE measurements obtained between 15 November and 15 December 2005 within the region of $80° \leq$ longitude $\leq 160°$ and $-15° \leq$ latitude $\leq 10°$ were averaged.

5.2 Ozone and water vapour in the TTL

Figure 5.2 shows the annual cycle of water vapour and ozone at 400 K, averaged between $\pm 20°$ latitude. Model predicted mean water vapour mixing ratios are in good agreement with observations. The slight phase shift between model calculations and observations is similar to that reported by *Fueglistaler et al.* (2005). Of relevance here, however, is the fact that the diabatic and kinematic model calculations give fairly similar results.

For ozone, the model predictions roughly span the range from low-biased (diabatic calculations using HALOE initialisation) to high-biased (kinematic calculations using ERA-Interim initialisation). The differences between predicted ozone concentrations follow a simple pattern: calculations initialised with HALOE yield lower concentrations than those initialised with the ERA-Interim ozone f eld, and the kinematic calculations yield higher concentrations than those based on the diabatic trajectory calculations. Importantly, the differences between kinematic and diabatic calculations (about 20% for either initialisation) are much larger for ozone than for water vapour.

The seasonality of the model predicted ozone f ts observations reasonably well, with a tendency to overestimate the amplitude in particular for the diabatic trajectory calculations. Overall, however, agreement with observations is reasonable in particular if one bears in mind the observational uncertainty between HALOE and SHADOZ estimates. The most interesting result is the difference between the calculations based on kinematic and diabatic trajectories, with kinematic predicted ozone concentrations signif cantly higher than diabatic.

Figure 5.2c shows the predicted ozone mixing ratios based solely on the initial values, i.e. the passively advected ozone. The f gure shows that the different initialisation accounts for much of the difference between the full model calculations.

Figure 5.2d shows the predicted ozone based only on chemistry along the trajectories. For all calculations, the integrated production over the three-month trajectory period is about half (and less) that of the initialisation f eld. The differences between diabatic and kinematic ozone predictions due to chemistry and passive transport are of the same order of magnitude. Also, the seasonality of predicted ozone concentrations is not a result of chemical production along these three-month trajectories, but of passive transport of the initialisation values. The chemical
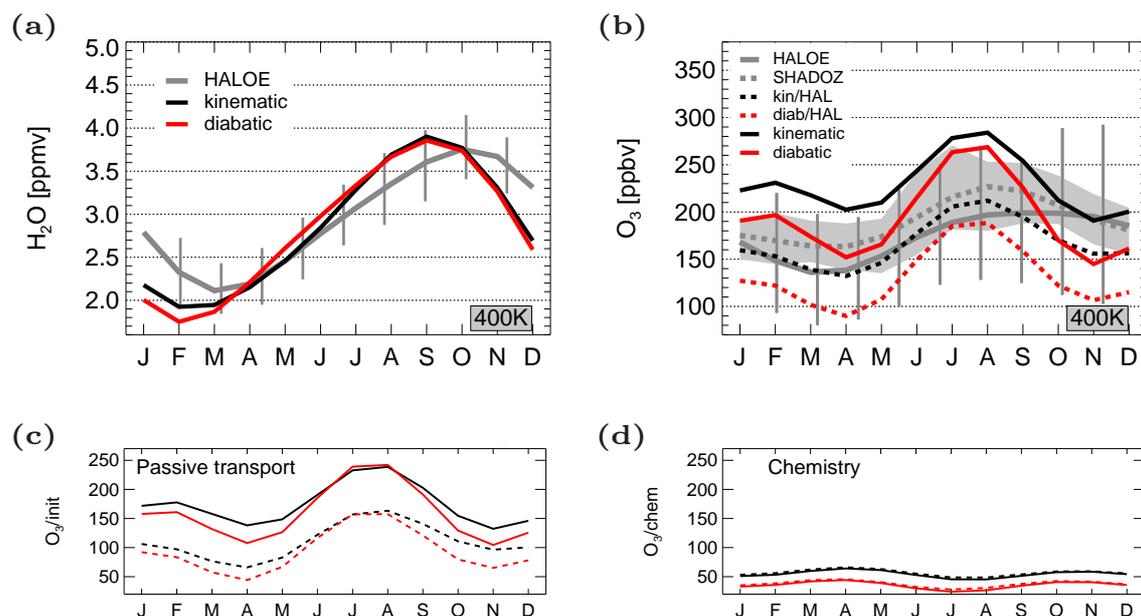
Figure 5.2: Monthly mean, tropical mean (20°S–20°N latitude) mixing ratios at 400 K for (a) water vapour and (b) ozone from HALOE (averaged for years 2001–2005; grey solid lines, with range of ±1-standard deviation as vertical bars), and from SHADOZ (1998–2006; for ozone only, grey dotted line and grey shading for range of ±1-standard deviation). The model predictions based on initialisation with ERA-Interim are shown as solid lines, and with initialisation based on HALOE as dashed lines (for ozone only); calculations based on kinematic trajectories in black, diabatic trajectories in red. (c) Predicted ozone concentrations based on initial conditions only (i.e., passively advected ozone); same conventions as in (b). (d) Predicted ozone concentrations based on chemistry along trajectories; same conventions as in (b). All lines are harmonic f ts to the monthly values, using annual and semi-annual harmonics. (Figure adapted from *Ploeger et al.*, 2011).

production along the three-month backtrajectories yields a semi-annual cycle that arises from the annual cycle of the Earth's inclination.

An integration length of 90 days for trajectories started on 400 K potential temperature in the tropics is close to the expected mean transport time from the upper troposphere to this level. Hence, one may suspect that the lack of an annual cycle in the TST-ensemble in Fig. 5.2d arises from truncation of the age-spectrum (compare *Hall and Plumb*, 1994; *Waugh and Hall*, 2002) at a value close to the mean transport timescale. However, sensitivity calculations using f ve-month instead of three-month backtrajectories give very similar results (not shown). This result supports the argument of *Konopka et al.* (2009) and *Konopka et al.* (2010) that the annual cycle in lower stratospheric ozone is a consequence of more in-mixing of stratospherically old air during the boreal summer months. The seasonality of ozone in the TTL will be further investigated in Chapt. 6.

This detailed analysis shows that for the model predictions of the annual cycle of ozone at
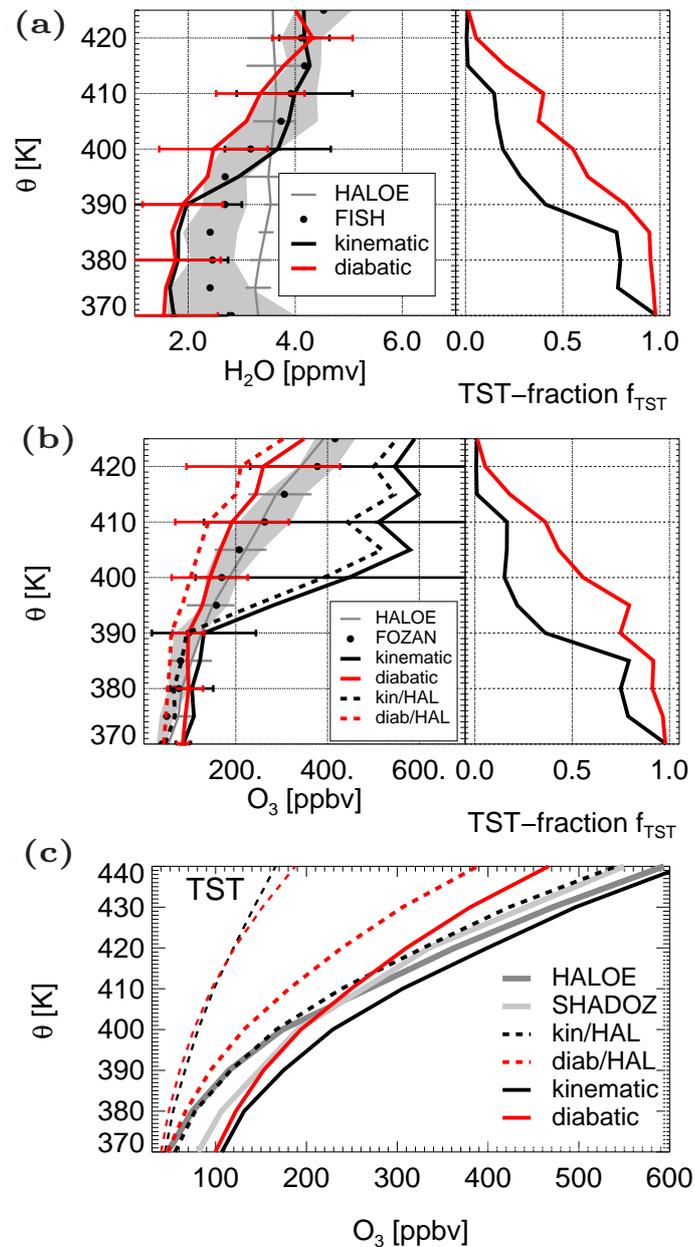
Figure 5.3: Mean water vapour (a) and ozone (b) prof les during the SCOUT-O3 campaign, binned in 5 K potential temperature bins. In-situ observations are from the FISH (total water, black dots; grey range 1-standard deviation) and FOZAN (ozone, black dots, grey range 1-standard deviation) instruments. Grey solid lines (bars show 1-standard deviation) are HALOE water vapour and ozone measurements during the SCOUT-O3 campaign (see text). Model predictions based on kinematic (black) and diabatic (red) trajectories with initialisation based on ERA-Interim are shown as solid, with ozone initialisation based on HALOE as dashed curves. Panels on righthandside show TST fractions (see text). (c) Prof les of tropical mean ozone concentrations from HALOE, SHADOZ and the 4 model calculations as labelled. Thin dashed red/black lines are ozone predictions from the TST ensemble with initialisation from HALOE ozone. (Figure adapted from *Ploeger et al.*, 2011).
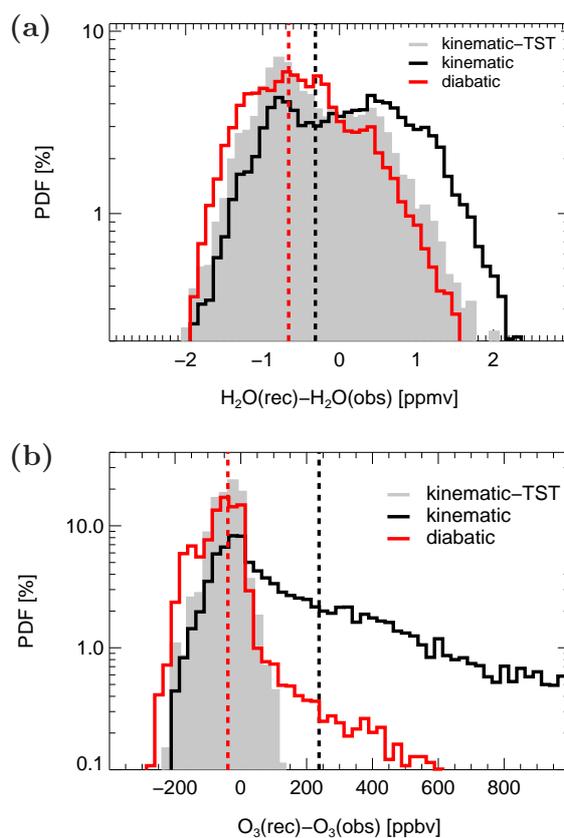
Figure 5.4: Probability distribution functions (PDFs) of differences between observed and reconstructed water vapour (a) and ozone (b) between 390 and 420 K. The bin size is 0.1 ppmv (25 ppbv) for water vapour (ozone). Dashed lines show the means of the distributions. The grey shading shows the PDF for the kinematic TST ensemble. (Figure adapted from *Ploeger et al.*, 2011).

400 K, the total difference (difference in initialisation with identical f elds, and chemical production) between kinematic and diabatic calculations is about 50 ppmv, which is similar to the difference arising from using different initialisation f elds.

Moreover, prof les of model predicted ozone and water vapour for the observations during the tropical SCOUT-O3 campaign are analysed. Figure 5.3a shows the FISH total water prof le, HALOE water vapour prof le, and the model water vapour predictions. Figure 5.3b shows the same information for ozone. The f ight track portions used for these prof les are not identical for the two species, as instruments were not always operational at the same time.

For water vapour, the in-situ measurements are drier than HALOE at tropopause levels (375 K-395 K potential temperature). The model predictions are generally within the range of in-situ observations (though a dry tendency is noted for levels below 400 K), and the difference between kinematic and diabatic model calculations around 400 K is larger than in the calculations of the annual cycle (Fig. 5.2a).

For ozone, the in-situ measurements and HALOE measurements agree quite well. For the

ozone model predictions, again the same pattern is found with respect to initialisation and trajectory type as seen in the annual cycle (Fig. 5.2b). An interesting difference between the ozone prof le prediction and those for the annual cycle at 400 K is that the differences between diabatic and kinematic calculations (i.e. red versus black lines of either initialisation) are much larger than the differences between the two initialisations (i.e. solid versus dotted of either trajectory type).

Figure 5.3c shows the same analysis for tropical mean ozone concentrations. As before, the diabatic trajectories yield lower ozone mixing ratios than the kinematic trajectories, and the calculations initialised with HALOE ozone yield lower values than those with ERA-Interim ozone. Further, the f gure shows that the model predictions of the TST ensemble are very similar between kinematic and diabatic trajectories, which conf rms that the differences in the predicted ozone f eld are driven by the stratospheric trajectory ensemble.

5.2.1 Importance of stratospheric trajectories

The separation of trajectories into TST trajectories and purely stratospheric trajectories (those that cannot be traced back to below 350 K) is used to address the question whether the differences between model predictions can be attributed to any of these two subsets. The right part of the panels of Fig. 5.3a/b shows the TST fractions for the calculations. The diabatic trajectories have generally a higher TST-fraction than the kinematic due to the higher vertical dispersion of the latter (further discussed below). Up to about 390 K potential temperature, model predictions are dominated by TST trajectories (with low initial ozone, irrespective of the initialisation f eld), while above the results are increasingly dominated by the stratospheric ensemble.

Figure 5.4 shows the probability distribution functions (PDFs) of the differences between measurements and model predictions for the in-situ prof les of water vapour (a) and ozone (b) between 390 and 420 K. The f gure shows that for water vapour, the distributions are slightly skewed, and that the shapes of the PDF are broadly similar for kinematic and diabatic trajectories, as well as for the kinematic TST ensemble (grey shading). For ozone, the f gure shows that the kinematic trajectory calculation has a distinct tail of very high biases. Comparison with the PDF of the TST ensemble shows that this tail of high biases is entirely due to stratospheric trajectories. In the case of the diabatic trajectories, no tail of very high biases is observed (note logarithmic scale).

To summarise, the analysis shows that model predictions of ozone are sensitive to initialisation and transport, and that it is in particular the stratospheric trajectory ensemble that is most sensitive to these factors. While the sensitivity to the initialisation f eld is not surprising, the much higher sensitivity to transport of ozone than water vapour suggests that ozone is a much better tracer to study important aspects of transport that observations of water vapour cannot resolve.
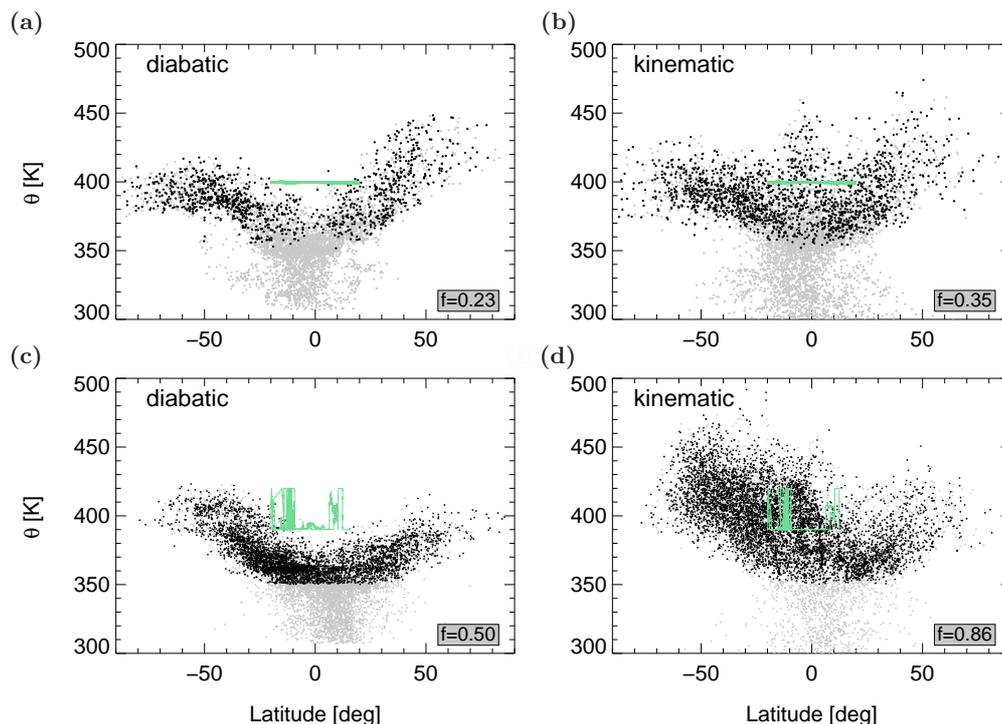
Figure 5.5: (a) Locations of backtrajectories in the latitude/potential temperature plane 60 days prior to starting time (left: diabatic; right: kinematic), started on 400 K potential temperature between $\pm 20°$ latitude. End points of stratospheric trajectories are in black, of TST trajectories (see text) in grey and the starting locations (400 K) in green. The number f denotes the fraction of stratospheric (non-TST) trajectories. (b) Same as (a), but for SCOUT-O3 backtrajectories, started along research aircraft f ight-tracks. (Figure adapted from *Ploeger et al.*, 2011).

5.3 Ozone and water vapour predictions for diabatic and kinematic transport

5.3.1 Origin of air parcels

The bulk transport characteristics for TST trajectories calculated from ERA-Interim data are quite similar for kinematic and diabatic trajectories (*Ploeger et al.*, 2010; *Liu et al.*, 2010). Figure 5.5 shows the position of the global (top panels) and SCOUT-O3 trajectories (bottom panels) when tracing them back in time for 60 days. The main differences, as already discussed in Chapt. 4, are the higher vertical dispersion and the occurrence of descent in the equatorial lower stratosphere for the kinematic trajectories. Consequently, the positions where the kinematic model calculations are initialised are more widespread than those of the diabatic calculations. The f gure shows that the differences are particularly prominent for the case study of the SCOUT-O3 tropical campaign.
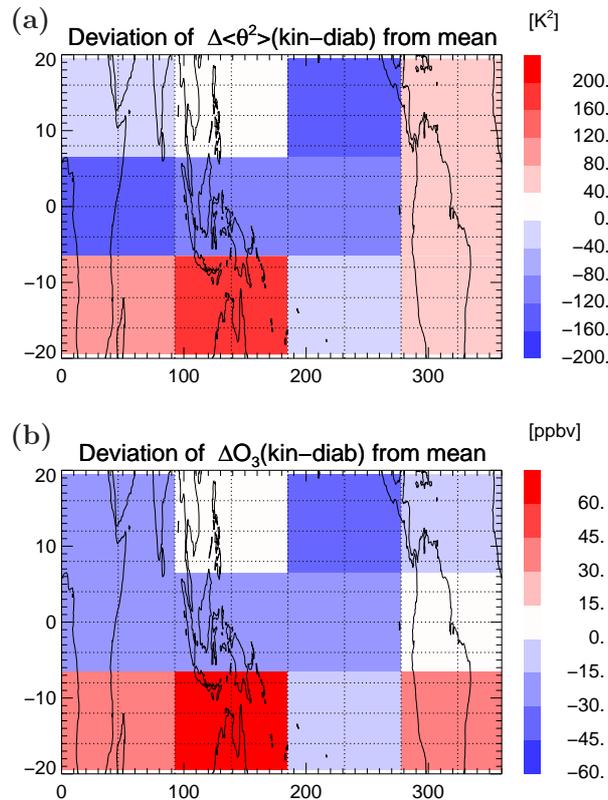
Figure 5.6: Anomaly (from tropical mean) of kinematic–diabatic dispersion $\langle \delta\theta^2 \rangle$ difference (a) and ozone difference (b) at 400 K on 20 November 2005. The data is binned into $13° \times 90°$ latitude-longitude bins. (Figure adapted from *Ploeger et al.*, 2011).

The differences in dispersion between ERA-Interim kinematic and diabatic trajectory calculations arise both from larger *noise* in the instantaneous vertical wind f eld than diabatic heating rates, and from large-scale and time-mean *systematic differences* in vertical transport (see also Fig. 4.6). For example, the inner tropics where the ERA-Interim vertical ω wind f eld reveals net subsidence show up very prominently in Fig. 5.5b.

The following paragraphs demonstrate that ozone is a remarkable tracer for dispersion of trajectories, and that much of the differences between kinematic and diabatic model predictions are a direct consequence of this sensitivity. Therefore, the 400 K isentrope is divided into horizontal bins of $13° \times 90°$ latitude/longitude bin size. For each bin, mean backtrajectory predicted ozone is calculated from all trajectories started in the respective bin. In addition, for each bin the vertical dispersion of backtrajectories is calculated in terms of potential temperature variance $\langle \delta\theta^2 \rangle$ (compare Eq. (4.1)) after three months, as explained in Sect. 4.5.1.

Figure 5.6 shows the results for a typical calculation where trajectories are started on 400 K on 20 November 2005. The f gure shows the anomalies (after subtraction of mean value over the 'tropics') of the differences between kinematic and diabatic trajectory calculations. This

calculation eliminates mean biases in ozone and dispersion, and leaves only the spatial pattern in differences between the kinematic and the diabatic calculations. The correspondence between the anomalies is very good, with larger vertical dispersion being positively correlated with larger ozone concentrations. The region over Northern Australia where the SCOUT-O3 campaign took place stands out as a region of maximum differences in both vertical dispersion and predicted ozone between kinematic and diabatic transport. In the following, it will be shown that the correlation is robust, but that the geographical locations of maxima vary with time, such that model comparisons with in-situ data as shown in Fig. 5.3b may give different results for different campaigns.

Figure 5.7 shows a similar information for trajectory calculations started once per month in 2002, expressed as a correlation plot. The x-axis is the kinematic–diabatic difference in potential temperature variance, while the y-axis is the corresponding difference for water vapour (a) and ozone (b). Each symbol represents one horizontal bin (as def ned in Fig. 5.6) for one month. The f gure shows that for water vapour no correlation is observed, whereas for ozone, the correlation coeff cient is $r = 0.84$. The red symbols are the twelve monthly data points for the area over Northern Australia. This region has always a high difference in ozone and dispersion, but is not always the location of the maximum difference. Similarly, the region of the Maritime continent (green data points) is also a region of a generally high differences although it is not the case for the calculation for 20 November 2005 (Fig. 5.6).

5.4 Discussion: Water vapour, ozone and transport in the TTL

5.4.1 Different sensitivities of water vapour and ozone to transport

The higher sensitivity of ozone than water vapour to relatively small differences in transport, as between ERA-Interim kinematic and diabatic trajectories, is primarily caused by the much larger spatial gradients of stratospheric ozone than water vapour. With current tropospheric methane concentrations the maximum increase in stratospheric water vapour is about a doubling of water vapour entry mixing ratios. Conversely, net ozone production maximises in the tropical lower stratosphere, increasing ozone entry volume mixing ratios from about 100 ppbv (parts per billion by volume) by a factor 100 to about 10 ppmv around 10 hPa. Consequently, even small differences in the initialisation positions and pathways of the stratospheric trajectory ensemble have a large impact on predicted ozone, while they have only a small effect on water vapour.

For the TST ensemble both ozone and water vapour are relatively insensitive to the choice of the transport representation. For water vapour, the insensitivity arises from the 'loss of memory' of initial conditions as a trajectory approaches the minimum saturation mixing ratios at the tropical tropopause. The difference in the distribution of the position of minimum saturation mixing
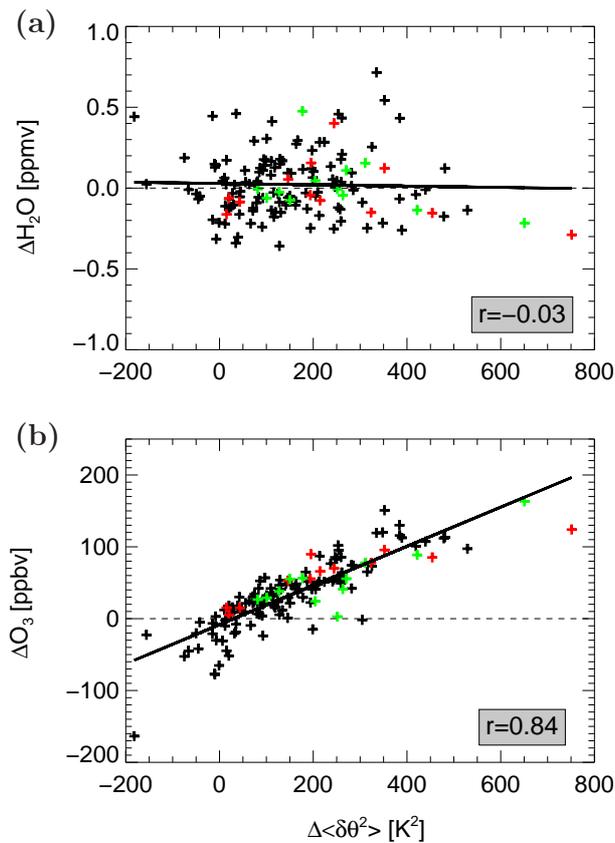
Figure 5.7: (a) Correlation between difference in backtrajectory predicted water vapour and difference in dispersion (quantif ed from potential temperature variance $\langle \delta\theta^2 \rangle$, see text) between kinematic and diabatic backtrajectories started in the tropics on 400 K potential temperature once per month over the year 2002. Each symbol represents the water vapour and dispersion difference for one grid box of $13° \times 90°$ latitude/longitude (analogous to Fig. 5.6). (b) Same as (a) but for ozone. Red/green data points in both panels refer to the grid box over Northern Australia and the Maritime continent region (see Fig. 5.6). The correlation coeff cient r is shown in each panel. (Figure adapted from *Ploeger et al.*, 2011).

ratios between kinematic and diabatic ERA-Interim trajectories induces only minor differences in model predicted entry mixing ratios. The pattern of distribution of minimum saturation mixing ratio of TST-trajectories identif ed by *Bonazzola and Haynes* (2004); *Fueglistaler et al.* (2005) is a robust feature of TST, in agreement with previous work (*Krüger et al.*, 2008).

The model ozone predictions for TST trajectories only are insensitive to the transport representation, because for ERA-Interim kinematic and diabatic trajectories the typical pathways and times to rise into the stratosphere are very similar. Also the sensitivity to initial conditions is much smaller for ozone predictions from TST than to predictions from stratospheric trajectories, because for TST the relative importance of integrated production compared to passive transport is higher than for stratospheric trajectories.

5.4.2 Mean transport and dispersion in the TTL and lower stratosphere

Variations in tropical stratospheric upwelling are a direct consequence of variations in the strength of the wave-driven stratospheric circulation (*Holton et al.*, 1995). Analysis of the atmospheric tape recorder signal of tropical stratospheric water vapour (*Mote et al.*, 1996) for estimates of upwelling, and model validation is a standard practice. *Avallone and Prather* (1996) showed that in principle the same information can be obtained from the vertical gradient in tropical lower stratospheric ozone. *Randel et al.* (2007) and *Konopka et al.* (2009) further studied the relation between upwelling and ozone, and the possible role of horizontal, quasi-isentropic in-mixing.

The presented results using the full 4-dimensional transport as represented by trajectories suggest that diabatic dispersion may play a signif cant role for tropical lower stratospheric ozone concentrations. Consequently, analyses based on a model of the timescale of mean transport may be misleading as the 'tail' of the stratospheric age-of-air distribution may have a large inf uence on tropical lower stratospheric ozone mixing ratios.

Figure 5.8 shows the tropical mean observed prof les (HALOE and SHADOZ) and the kinematic and diabatic model predictions using the ERA-Interim ozone f eld as shown in Fig. 5.3c. The f gure further shows the prof le of predicted ozone for the diabatic trajectory calculation where the model diabatic heating rates were multiplied with a factor 0.7. The main effect of this procedure is a reduction in mean upwelling by about 30% (see *Liu et al.*, 2010). The f gure shows that the diabatic calculation with 30% reduced upwelling gives an ozone prof le that is virtually identical to that of the kinematic calculation despite its much lower vertical dispersion.

Since neither true dispersion nor upwelling velocity in the TTL are known exactly, it is not possible to precisely deduce any one of the two parameters from ozone alone. Rather, it may be that the combination of phase propagation of the water vapour tape recorder signal with the annual cycle in ozone concentrations allows one to determine both mean upwelling and dispersion accurately.

5.4.3 Constraints for the lower stratospheric circulation

The above analysis suggests that a combination of ozone and water vapour may be able to constrain transport in the TTL and lower stratosphere better than water vapour alone (e.g., *Mote et al.*, 1998). In particular, the possibility that very deep convection overshooting its level of neutral buoyancy induces a diabatic downwelling over regions of intense convection (*Sherwood*, 2000) remains a subject of interest that has not yet been conclusively resolved.

The presented results are ambiguous with respect to this question. As emphasised throughout this chapter, due care should be used when interpreting absolute values of predicted ozone and water vapour concentrations. However, the following aspects are noteworthy in this context.

The ERA-Interim vertical ω wind shows net downwelling over the equatorial stratosphere
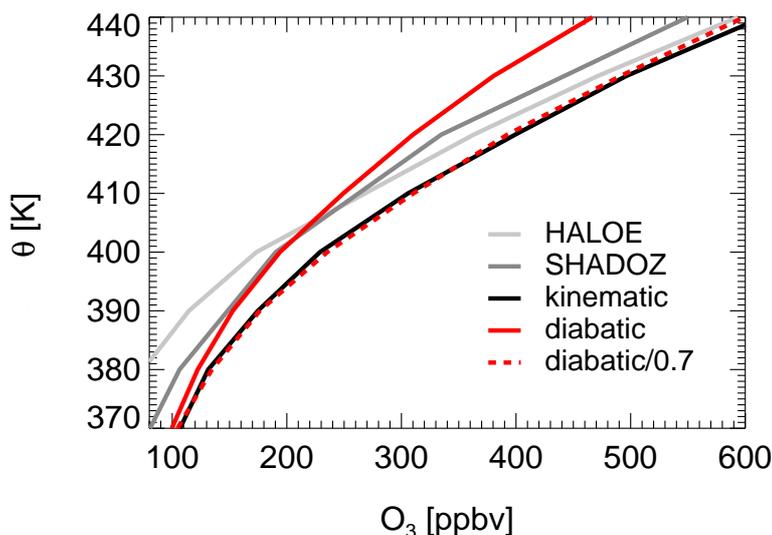
Figure 5.8: Mean tropical ozone prof les, reconstructed from backtrajectories and from HALOE and SHADOZ observations. Shown are the diabatic (red solid) and the kinematic (black) reconstructions of Fig. 5.3c and in addition the 'corrected' diabatic reconstruction with vertical velocity multiplied by a factor 0.7 (red dashed). The 'corrected' diabatic almost coincides with the kinematic reconstruction. (Figure adapted from *Ploeger et al.*, 2011).

(although over the full tropics, the net motion is ascent). It is presently not clear why there is some descent and it is, evidently, not clear whether this descent is real or an artefact of the assimilation procedure. In any case, the fact that the vertical wind f eld shows descent whereas the diabatic heating in the same reanalysis shows broad upwelling throughout the tropics, may allow some insight about the implications on ozone from comparison between the kinematic and diabatic transport calculations.

The model calculations based on diabatic trajectories and initialised with HALOE have a general tendency to give a prof le that is low biased when compared to the HALOE tropical prof le as well as to the HALOE or FOZAN prof les for the SCOUT-O3 campaign (Figs. 5.2b;5.3b,c). Conversely, the calculations initialised with HALOE and using kinematic trajectories for transport yield good agreement for the tropical mean ozone prof le (Figs. 5.2b;5.3c). However, for the SCOUT-O3 campaign, where the largest impact from downwelling would be expected, because of the proximity to the maritime continent region, the kinematic trajectories that include downwelling (Fig. 5.5b) yield a large high bias (Fig. 5.3b), which argues against the occurrence of equatorial lower stratospheric downwelling.

Hence, the presented calculations remain inconclusive with respect to this particular problem. Progress is anticipated if it were possible to constrain the timescale of troposphere-to-stratosphere transport to better than the ±30% required to bring ozone predictions of diabatic and kinematic trajectories into agreement.

5.5 Chapter conclusions

Three-month backtrajectories were combined with a simple chemical model of ozone production, and of dehydration. The annual cycle of upper TTL ozone, as well as tropical mean ozone prof les and even in-situ observed mean prof les during the tropical SCOUT-O3 campaign are reasonably well predicted. Compared to predictions of water vapour, there is a higher sensitivity of predicted absolute ozone concentrations to initialisation. Further, there is uncertainty in observed lower stratospheric ozone concentrations, with measurements from different sensors and platforms differing on the order of 10-20%. Therefore, the focus here is not on interpreting absolute values of model predictions. Rather, differences between model calculations using kinematic and diabatic trajectories are emphasised.

The results show that ozone is very sensitive to dispersion, much more so than water vapour. A robust result is that the larger the trajectory dispersion, the higher the model predicted ozone concentration. Ozone concentrations are also sensitive to the rate of tropical ascent. Consequently there exists some ambiguity between the rate of ascent and smaller-scale mixing. This ambiguity might affect the conclusions that can be drawn from comparison of observed ozone and that of CCMs. The comparison between observed and modelled ozone may provide new constraints on transport in the TTL and lower stratosphere if it were possible to determine the timescale of ascent more accurately.

Due to higher dispersion, kinematic predicted ozone concentrations are always higher, and with a larger variance around mean values, compared to diabatic. It is not clear without ambiguity, whether diabatic or kinematic predictions agree better with atmospheric observations. However, diabatic transport provides a clearer picture of the underlying transport processes. For kinematic transport, on the contrary, large dispersion blurs effects of the large-scale circulation, particularly of mean ascent, and renders the interpretation of results more complicated.

6 Impact of horizontal in-mixing on trace gas seasonality in the TTL

Several trace gases show discernible seasonal variations in the TTL. Prominent annual cycles are evident in concentrations of water vapour (*Mote et al.*, 1995), ozone (*Thompson et al.*, 2003; *Folkins et al.*, 2006; *Randel et al.*, 2007) and carbon monoxide (*Schoeberl et al.*, 2006), an irregular cycle for instance in HCN concentrations (*Pumphrey et al.*, 2008; *Randel et al.*, 2010; *Pommrich et al.*, 2010b), which potentially propagate upwards into the stratosphere with the Brewer-Dobson circulation (the so-called 'atmospheric tape recorder'). However, different mechanisms are involved in the forcing of seasonality of different species.

Generally, these forcing mechanisms are analysed from a perspective assuming the tropics as isolated against exchange with the extratropics (tropical perspective). For water vapour, the one dimensional tropical perspective works rather well, relating the annual variation in concentrations to the annual variation in tropical tropopause temperatures, which is in turn caused by the seasonality of tropical upwelling (see Sect. 2.3). Exchange with the extratropics turns out to be essential for dilution of H_2O tape recorder extrema in the lower stratosphere (*Mote et al.*, 1998), but seems of second order importance for causing the seasonality in the TTL.

The annual cycle of ozone in the TTL was recently explained both from either a pure tropical perspective (*Randel et al.*, 2007) or with in-mixing of ozone rich extratropical air during boreal summer as the main forcing mechanism (*Konopka et al.*, 2009, 2010). The relevance of in-mixing for the seasonality of ozone and other species in the TTL is currently under debate.

It was proposed by *Chen* (1995) that mainly the equatorward component of anticyclonic f ow of the Asian, American and Australian monsoons is causing in-mixing from the extratropical lowermost stratosphere into the TTL (see Sect. 2.1). The strongest monsoon system is by far the Asian monsoon, and consequently strongest in-mixing is expected to occur during summer.

This chapter provides an analysis of the link between trace gas seasonality in the TTL and meridional transport (in-mixing) into the TTL, for the three species water vapour, ozone and carbon monoxide. The questions raised are:

- *Is there a significant seasonal pattern of in-mixing into the TTL, and what is the forcing of the pattern?*

- *Is there an impact of in-mixing on the seasonality of water vapour, ozone and carbon monoxide in the TTL, and how large is this impact?*

Outline of the method

Mean water vapour, ozone and carbon monoxide concentrations in the tropical tropopause layer are predicted from three-month diabatic and kinematic backtrajectories (transport representations *diabatic*, *kinematic* in Tab. 3.1). Because it is unclear which representation yields the more realistic backtrajectory prediction (compare Chapt. 5), both diabatic and kinematic predictions are shown in the following, to indicate the uncertainty range due to the choice of the transport representation.

Backtrajectory ensembles are started in the TTL ($2° \times 2°$ latitude/longitude grid, 20°S–20°N equivalent latitude) along nine equally spaced potential temperature levels between 370 and 450 K at the 15th of each month of 2004 and 2005. Backtrajectory predicted water vapour and ozone mixing ratios are calculated as described in Sect. 5.1, hence for water vapour based on freeze-drying and instantaneous sedimentation, and for ozone mainly on photochemical production. Chemical loss due to HO_x radicals is included in the calculation, but turns out insignif cant for the shown results, as explained in App. B.

Moreover, also carbon monoxide concentrations are predicted from the backtrajectory ensembles. Backtrajectories are initialised with CO concentrations from the diabatic CLaMS long-term simulation (see Chapt. 7) at the end points (in backward time), or as soon as they encounter regions below 360 K potential temperature. Only chemical loss due to reaction with OH radicals (reaction (R1) in Tab. 7.1) is calculated along the trajectories, yielding a reasonable CO estimate in the upper TTL and tropical lower stratosphere, as shown by *Pommrich et al.* (2010a).

For the trajectory analysis, transport into the TTL is divided into tropical transport, transport from the northern hemisphere (NH) and transport from the southern hemisphere (SH) extratropics. Hence, $f_t + f_n + f_s = 1$, with f_i denoting the corresponding trajectory fractions (t tropics, n northern, s southern hemisphere). Accordingly, the mean trace gas mixing ratio μ in the TTL can be written

$$\mu = f_t \mu_t + f_n \mu_n + f_s \mu_s \,, \tag{6.1}$$

with μ_t, μ_n and μ_s the mean mixing ratios for tropical transport and for in-mixing from the NH and SH extratropics, respectively. Consequently, the seasonality of mean trace gas concentrations in the TTL results from a rather complex superposition of the seasonality of transport and concentrations. In the following, f rst the seasonality of transport is investigated by considering the fractions f_i of tropical transport and of transport from the NH and SH extratropics into the TTL (Sect. 6.1). Second, in Sect. 6.2 the seasonality of mean concentrations μ_i for each transport pathway (tropically conf ned, in-mixed from NH and SH) is analysed by calculating the relative annual anomalies $\Delta_r \mu_i = \frac{\mu_i - [\mu_i]}{[\mu_i]}$. Here, brackets [.] denote the annual mean. Finally, the superposition of both effects (terms $f_i \mu_i$) is calculated, and the contributions of the different transport pathways $f_i \mu_i$ (compare Eq. (6.1)) to the mean TTL concentration are shown and discussed in Sect. 6.2.
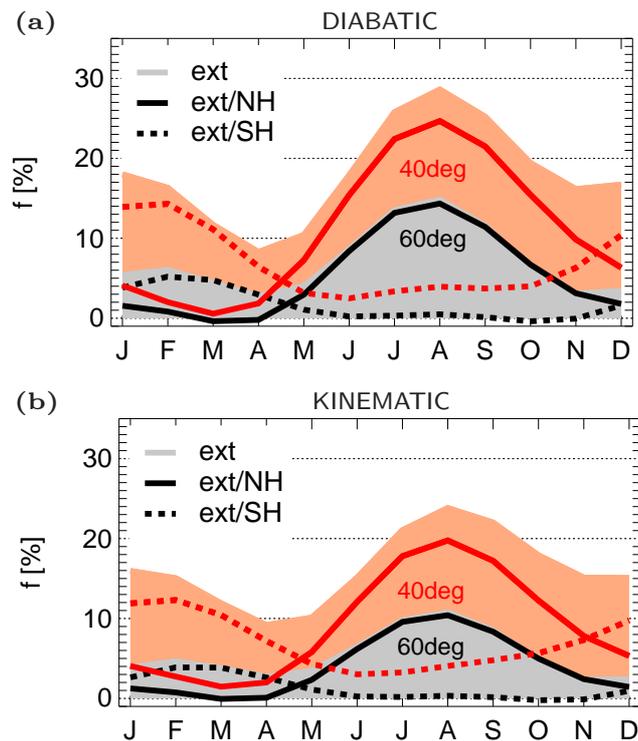
Figure 6.1: Annual cycle (2004–2005 climatology) of transport from the extratropics into the TTL (in-mixing), diagnosed as fractions of diabatic (a) and kinematic (b) backtrajectories (started at 400 K, 20°S–20°N equivalent latitude) transported from polewards 40°/60° equivalent latitude (reddish/grey shaded regions). The fractions transported from the NH are shown as red/black solid lines, for 40°/60° respectively. The SH in-mixed fractions are shown as red/black dashed lines.

6.1 Seasonality of transport into the TTL

Horizontal transport from the extratropics into the TTL (in-mixing) is quantif ed from those backtrajectories, which travel through regions polewards 40° equivalent latitude for at least f ve days (extratropical trajectories). The corresponding trajectory fraction is further divided into NH (f_n) and SH (f_s) in-mixed trajectories. The remaining trajectories represent tropical upward transport. As the separation between tropics and extratropics involves ambiguities, sensitivity calculations are performed with different boundary values (30°, 50°, 60°, and with latitude instead of equivalent latitude), with different trajectory integration lengths (5 months) and with the requirement that extratropical trajectories stay longer in the extratropical domain (20 days) and even end there. Exact numbers of in-mixed fractions are sensitive, but all conclusions of this chapter can be robustly drawn using any of these def nitions of in-mixing from the extratropics.

  Figure 6.1 shows the seasonality of tropical transport and in-mixing, as 2004–2005 climatology of fractions of NH/SH in-mixed trajectories (red solid/dashed lines), for diabatic (a) and kinematic (b) backtrajectories. The displayed lines are harmonic f ts to the monthly values (using
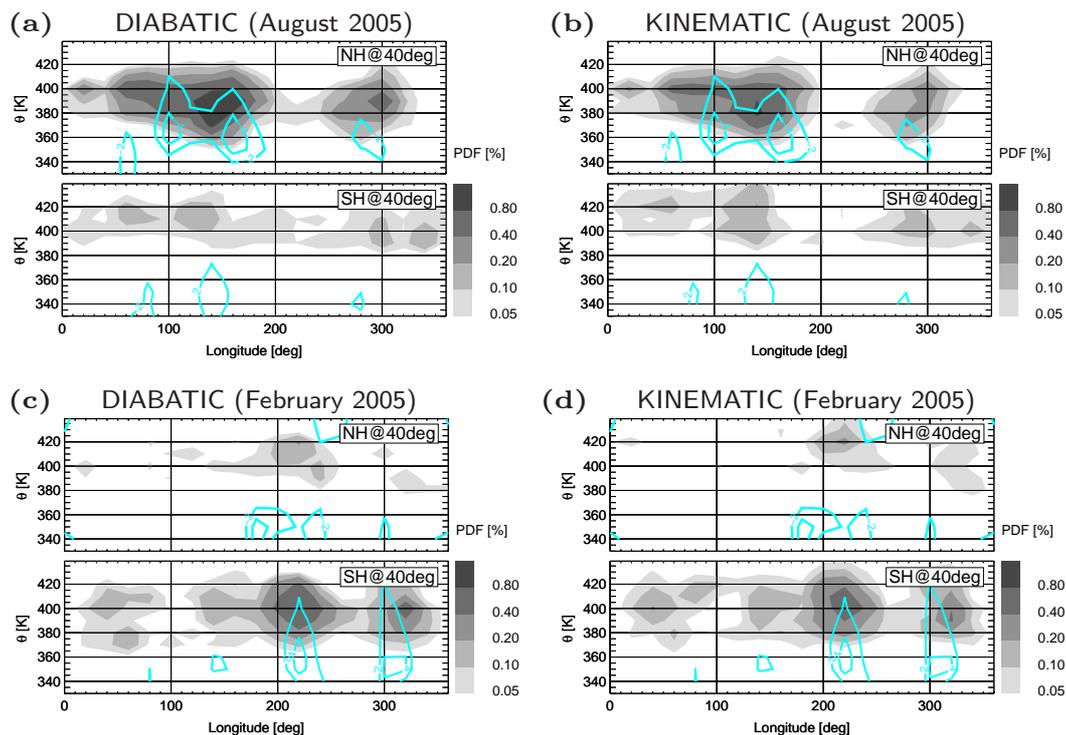
Figure 6.2: PDFs of locations of horizontal transport (in-mixing) across $40°$ equivalent latitude into the tropics for backtrajectories, started between 380 K and 430 K. (a) shows the PDFs for diabatic, (b) for kinematic backtrajectories started on 15 August 2005. (c) and (d) show the same PDFs as (a) and (b), but for starting date 15 February 2005. The cyan lines are 2004–2005 climatological summer (jja) and winter (djf) meridional wind (v) contours (NH: $-2, -4$ m/s; SH: $2, 4$ m/s).

annual and semi-annual harmonics). In-mixing from the NH and from the SH both clearly show inversely phased annual cycles, with maximum during boreal summer for in-mixing from the NH and during winter for in-mixing from the SH. Due to the stronger seasonality of in-mixing from the NH than from the SH, the superposition of both approximately yields an annual cycle of total in-mixing from the extratropics, with maximum during summer (reddish shading). During summer, about 20–30% (kinematic/diabatic transport representation uncertainty) of TTL air is transported from regions polewards $40°$ equivalent latitude. Here, there is no contradiction to the result of *Volk et al.* (1996), reporting on mid-latitude air fractions of about 10% around 400 K. The particular value of 10% was estimated from tracer in-situ observations during April and October and is in good agreement with the April/October in-mixing fractions of Fig. 6.1. However, the strong seasonality of in-mixing is not captured by the analysis of *Volk et al.* (1996).

The black lines (grey shading) show the same trajectory fractions for an extratropics boundary of $60°$ equivalent latitude. Although the fractions are reduced, the annual cycles are still distinct. The NH is less reduced than the SH maximum, and consequently transport reaches farther polewards during boreal summer compared to winter.

In Fig. 6.2 the meridional locations of in-mixing from the NH (top part of each panel) and from the SH (bottom part) are shown for diabatic/kinematic backtrajectories, started on 15 August and 15 February 2005, at the times of the NH and SH in-mixing maxima, respectively (compare Fig. 6.1). The cyan lines show 2004-2005 climatological summer (jja) and winter (djf) contours (for the August and February panels, respectively) of the equatorwards directed meridional wind v. During summer (Fig. 6.2a/b), main in-mixing occurs from the NH between about 80° and 190° and around 300° longitude, between about 370 and 420 K, at locations, where the anticyclonic f ow of the Asian and the North American ('Mexican') monsoons is directed towards the equator (compare the meridional wind contours). Similarly, during winter (Fig. 6.2c/d), maximum in-mixing occurs from the SH around 220° and 320° longitude, in the outf ow regions of the Australian and the South American ('Bolivian high') monsoons. Daily maps of trajectory positions (not shown) demonstrate that in-mixed trajectories indeed follow the anticyclonic monsoon f ow from high latitudes and enter the TTL on the eastern side of the anticyclone. Thus, the monsoons, in particular the Asian monsoon, are identif ed as the main driving factors for in-mixing from the extratropics into the TTL, in agreement with *Chen* (1995).

6.2 Seasonality of trace gas concentrations

Figure 6.3 shows the seasonality of backtrajectory predicted water vapour (a: diabatic, b: kinematic), ozone (c: diabatic, d: kinematic) and carbon monoxide (e: diabatic, f: kinematic) in the TTL at 400 K (black solid). For H_2O and O_3 a 2004–2005 climatology is shown, for CO only the year 2005. Displayed is the relative annual anomaly $\Delta_r \mu = \frac{\mu - [\mu]}{[\mu]}$, which is largely robust concerning offsets in absolute concentrations due to different instruments or different predictions (transport representation, initialisation, compare Chapt. 5). For water vapour and ozone the backtrajectory prediction is compared to 2004–2005 climatological HALOE (grey solid, with error bars showing standard deviation), and for carbon monoxide to 2005 MLS observations (also grey solid, with error bars the standard deviation). For ozone, SHADOZ observations (grey dashed, period 1998–2006) are shown in addition. All lines are harmonic f ts to the monthly values. Water vapour and ozone observations both show a distinct annual cycle, with maximum concentrations for water vapour around October, for ozone around August/September. Carbon monoxide observations show an annual cycle with minimum concentrations around September.

The trajectory prediction at 400 K is calculated as the weighted average of trajectory predictions at 380, 400, and 420 K (with weights 0.25, 0.5, 0.25), for better comparison with the coarsely resolved satellite data. The f gure shows that the observed and trajectory predicted seasonality of water vapour, ozone and carbon monoxide agrees well.

For H_2O, the main difference is a phase shift with predicted maxima occurring about one month earlier than observed maxima. This difference is most likely caused by too fast mean upwelling in the ERA-Interim reanalysis. Reducing diabatic heating rates by a factor 0.7 signif-
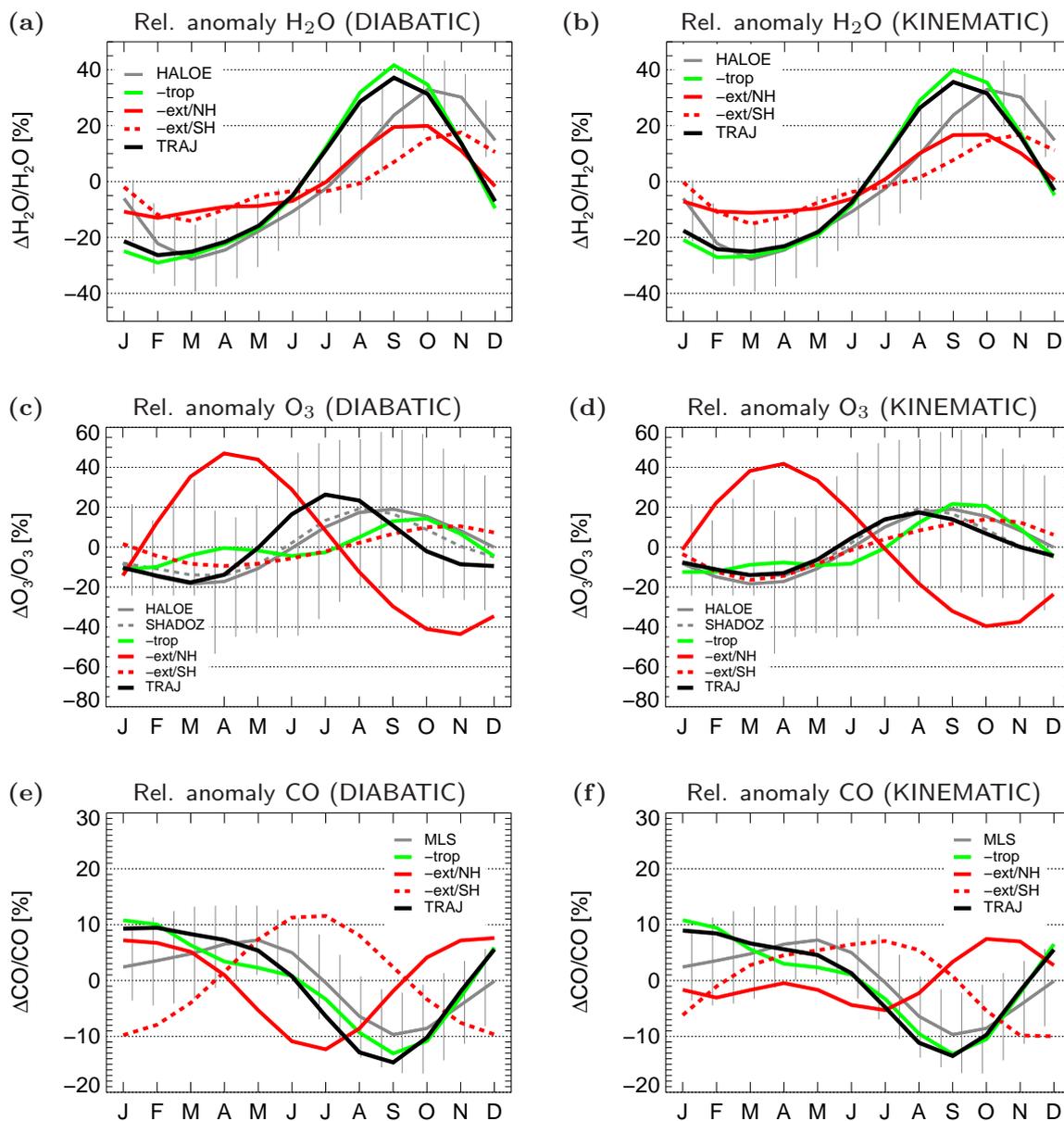
Figure 6.3: (a,b) Relative annual anomaly for water vapour (2004–2005) at 400 K (20°S–20°N equivalent latitude) predicted from backtrajectories (black line, a: diabatic, b: kinematic) and observed by HALOE (grey, with error bars standard deviation). The relative anomalies for tropical trajectories are shown as green, for NH/SH in-mixed as red solid/dashed lines (see text). (c,d) same as (a,b), but for ozone. In the case of ozone, also SHADOZ observations are shown (grey dashed). (e,f) same as (a,b), but for CO , and only for the year 2005 (instead of 2004–2005) and MLS instead of HALOE observations. All lines are harmonic f ts to the monthly values, using annual and semi-annual harmonics.
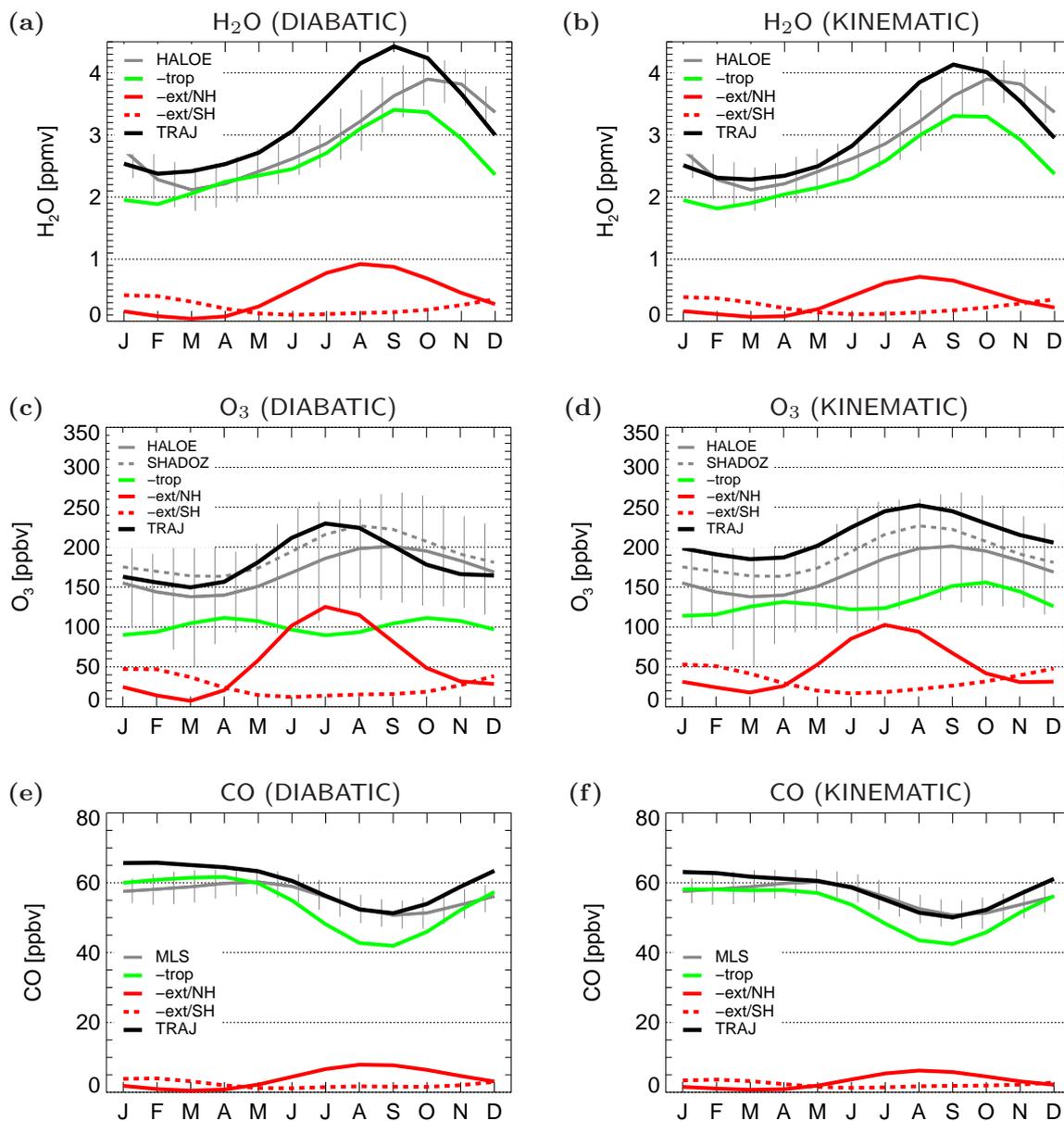
Figure 6.4: Same as in Fig. 6.3, but for the tropical/NH/SH contributions $f_i \mu_i$ to the mean TTL concentration (black line), instead of relative anomalies. Here, f_i is the trajectory fraction, μ_i the mean concentration, see Eq. (6.1). The green line shows the contribution from tropically conf ned transport $f_t \mu_t$, the red solid line the NH in-mixed contribution $f_n \mu_n$, the red dashed line the SH in-mixed contribution $f_s \mu_s$.

icantly reduces the phase difference between prediction and observation (not shown). For O_3, the kinematic prediction agrees well with HALOE and even better with SHADOZ observations, whereas the diabatic prediction maximum appears signif cantly too early, with a too high maximum concentration. However, this is not interpreted in the sense that kinematic transport is more realistic, due to reasons discussed in Chapt. 5 (much better agreement of the diabatic prediction with SCOUT-O3 observations). Rather, the kinematic–diabatic difference shows the range of uncertainty in the transport representation. Of importance below is that for both ozone predictions the processes forcing the seasonality are the same.

Hence, apart from a mean upwelling error, the backtrajectory approach seems to capture the key processes controlling the seasonality of water vapour, ozone and carbon monoxide in the TTL.

The relative annual anomaly predicted from the tropical trajectory ensemble is shown as green solid, predicted from the NH/SH in-mixed ensembles as red solid/dashed lines, in Fig. 6.3. The respective seasonality would have resulted if all the air in the TTL had been either transported tropically conf ned, or in-mixed from the NH/SH extratropics.

For water vapour (Fig. 6.3a/b) the picture is rather clear. Tropical, NH and SH in-mixed concentrations all show annual cycles. The three annual cycles are nearly in-phase, with maximum concentrations during autumn, and interfere constructively. However, the rather small difference between total (black solid) and tropical (green dashed) concentrations demonstrates that the annual cycle of upper TTL water vapour can be understood from the seasonality of tropically conf ned transport alone. The impact of in-mixing from the extratropics is a second-order effect.

For carbon monoxide (Fig. 6.3e/f) both tropical transport and in-mixing from the NH show annual cycles with minimum values during summer, interfering constructively to the observed annual cycle. In-mixing from the SH contributes an annual cycle in phase opposition. Similar to the case of water vapour, the mean seasonality in the TTL is explained in f rst order by tropically conf ned transport. However, in-mixing has the potential to modify the position of the summer minimum (compare the shift between the green and the black line in Fig. 6.3e/f) and is not negligible.

For ozone the situation is more complex. Ozone concentrations in the NH (SH) extratropics are subject to annual cycles with maxima during boreal winter (summer), due to the seasonality of the Brewer-Dobson circulation. Consequently, NH and SH in-mixed concentrations (red solid and red dashed) both show annual cycles, but in phase opposition. Finally, ozone concentrations for tropically conf ned transport (green solid) reveal a semi-annual cycle. The two maxima during equinox (April and October) are caused by minimum solar zenith angles and maximum overhead ozone columns, causing maximum ozone production during these seasons. In contrast to water vapour, neither tropical nor in-mixed concentrations of ozone alone show the observed seasonality in the TTL.

Figure 6.4 demonstrates how the observed water vapour, ozone and carbon monoxide seasonality results from the superposition of tropically conf ned and NH/SH in-mixed concentrations

μ_i, weighted with the respective transport fractions f_i. The f gure shows the three terms $f_i \mu_i$ of Eq. (6.1) which add up to the predicted concentrations (black lines).

The HALOE observed water vapour seasonality (grey) in Fig. 6.4a/b is reasonably well explained by tropical upward transport alone (green). The NH in-mixed proportion is superposed in-phase and amplif es the predicted annual oscillation by contributing to the amplitude about half as much as tropical transport. The SH in-mixed proportion is superposed in phase opposition and therefore attenuates the annual oscillation. The situation for carbon monoxide in Fig. 6.4e/f is similar, with in-mixing contributing to a slight modif cation of tropically conf ned concentrations.

For ozone (Fig. 6.4c/d), the annual cycle of predicted concentrations is clearly attributed to in-mixing from the NH extratropics. During boreal winter, NH in-mixing contributes a vanishing proportion to the predicted ozone concentration, but during summer this proportion increases to about 50%. The proportion due to tropical transport shows a slight semi-annual oscillation, as explained above. Hence, tropical transport effectively broadens the summer ozone maximum caused by NH in-mixing. The SH proportion is again superposed in phase opposition and slightly attenuates the annual cycle.

6.3 Discussion: The annual ozone cycle in the TTL

Recently, *Randel et al.* (2007) and *Konopka et al.* (2009) proposed two different mechanisms of forcing of the annual ozone cycle in the upper TTL. *Randel et al.* (2007) proposed that the annual cycle in O_3 concentrations results from the annual cycle in tropical Brewer-Dobson circulation upwelling acting on the strong O_3 background gradient. On the contrary, *Konopka et al.* (2009) emphasised the role of monsoon driven in-mixing of high O_3 concentrations from the extratropics during summer. The above presented backtrajectory analysis corroborates the mechanism proposed by *Konopka et al.* (2009), with in-mixing causing the annual cycle, and tropical upward transport showing only a slight semi-annual cycle. In the following, it will be investigated whether upwelling seasonality has the potential to cause an annual cycle of O_3 in the TTL, at all.

Therefore, a simple one-dimensional model is used, based on zonal mean tropical ($10°S$–$10°N$) ERA-Interim data in isentropic coordinates. A (time) mean vertical velocity prof le $\langle \dot{\theta} \rangle$ is calculated by averaging the zonal mean tropical vertical velocity over the 2004–2005 period. An idealised annual upwelling variation is added via

$$\dot{\theta}(t,\theta) = \langle \dot{\theta} \rangle + \alpha \langle \dot{\theta} \rangle \cos\left(\frac{2\pi t}{T}\right), \tag{6.2}$$

with $T = 365$ days. Here, the parameter α is introduced to vary the strength of the annual amplitude. The relative anomaly of the upwelling velocity at $400\,K$, namely

$$\Delta_r \dot{\theta} = \alpha \cos\left(\frac{2\pi t}{T}\right), \tag{6.3}$$
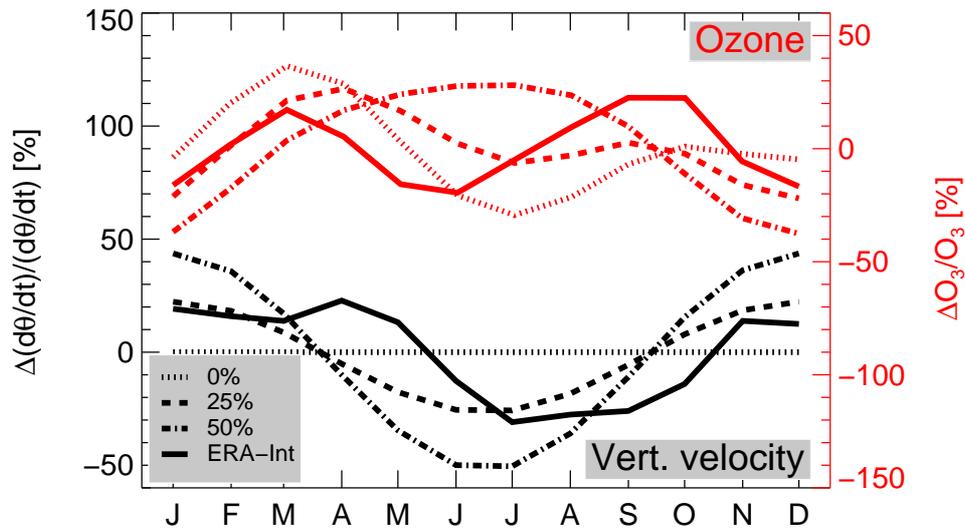
Figure 6.5: Sensitivity of the seasonality of tropical (10°S–10°N latitude) ozone (red) at 400 K to the seasonality in mean tropical upwelling (black), diagnosed from one dimensional tropical trajectories (constant upwelling: dotted; 25% amplitude: dashed; 50% amplitude: dash-dotted, see text). The seasonalities of tropical mean (10°S–10°N latitude) ERA-Interim upwelling and corresponding ozone are illustrated as solid lines, for comparison.

is shown in the bottom part of Fig. 6.5 (corresponding y-axis on the left). For $\alpha = 0$ (dotted black), upwelling is constant in time, for $\alpha = 0.25$ and 0.5 the relative annual amplitude is 25 and 50% (black dashed, dash-dotted), respectively. The black solid line shows the tropical mean (10°S–10°N) ERA-Interim diabatic upwelling, for comparison.

In the top part of Fig. 6.5 (corresponding y-axis on the right), the relative anomaly of predicted ozone at 400 K is shown (red lines). Predicted O_3 concentrations are calculated by integrating the O_3 production rate along one-dimensional backtrajectories in the vertical velocity f eld, def ned by Eq. (6.2), analogously to the O_3 prediction for the three-dimensional backtrajectories in the previous section, but without chemical loss included. For upwelling constant in time ($\alpha = 0$), predicted O_3 shows a semi-annual cycle, due to the semi-annual cycle in O_3 production rates (see above). As the annual upwelling amplitude increases, the semi-annual cycle of predicted O_3 gradually changes into an annual cycle. For an upwelling amplitude of 50%, predicted O_3 shows a clear annual cycle (red dash-dotted). The red solid line shows predicted O_3 for the tropical mean ERA-Interim diabatic upwelling velocity, revealing a semi-annual cycle.

To summarise, the forcing mechanism proposed by *Randel et al.* (2007), namely that an annual seasonality in upwelling velocity causes an annual cycle in ozone, works out. However, the annual upwelling amplitude has to be rather large to predominate the semi-annual cycle in O_3 production rates. The about 25% relative amplitude of tropical upwelling in 'ECMWF (ERA-Interim) world', is not suff cient to cause an annual ozone cycle.

6.4 Chapter conclusions

The above backtrajectory analysis demonstrates that the three leading transport pathways into the TTL, tropically conf ned upwelling, meridional in-mixing from the NH and from the SH extra-tropics, all show an annual variation. For tropical upward transport, maximum transport occurs during boreal winter, for in-mixing from the NH during summer, and for SH in-mixing again during winter. In-mixing from the NH is dominant compared to SH in-mixing, and total in-mixing from the extratropics reveals an approximate annual cycle with maximum in-mixing during summer. The monsoon anticyclones, particularly the Asian summer monsoon, are identif ed as the main drivers for in-mixing.

The transported concentrations are subject to trace gas specif c seasonalities, resembling the dynamical and chemical control processes. Therefore, in general, trace gas variations in the TTL result from a rather complex superposition of the seasonality of all different transport pathways.

Horizontal in-mixing from the extratropics has a crucial impact on seasonal variations of ozone and a much weaker impact on variations of water vapour and carbon monoxide. The annual cycle of ozone in the upper TTL turns out to result, at least in 'ECMWF world', from the superposition of two annual cycles, due to in-mixing from the two hemispheres, and one semi-annual cycle, due to tropical upwelling. For water vapour, in contrast, all three pathways contribute annual cycles, which are superposed in-phase. Thus, although for certain species tropically conf ned transport may provide the correct seasonality, in general, exchange between tropics and extratropics is an important inf uencing factor for seasonality in the tropics. It is therefore crucial for model development, to correctly formulate meridional exchange between tropics and extratropics.

7 CLaMS simulations based on ERA-Interim

In the previous chapters trajectory studies were presented to investigate transport uncertainties and their impact on model predictions. The analysis showed that for modelling tropical transport from the troposphere to the stratosphere all terms in the diabatic heat budget (all-sky radiation and latent heat release) have to be taken into account (compare Chapt. 3 and Chapt. 4). Consequently, for model simulations using the full CLaMS model, vertical velocity based on all contributions to the diabatic heat budget seems best suited. Therefore, the vertical transport representation of the CLaMS model was improved as explained in Sect. 3.3.2, compared to the earlier transport representation which was based on clear-sky radiative heating and the vertical ω-wind below the LZRH (compare *Konopka et al.*, 2007).

In this chapter, f rst results of CLaMS simulations based on the diabatic ERA-Interim transport representation (*diabatic*, as def ned in Chapt. 3) are presented, with cross-isentropic vertical velocity deduced from the total diabatic heating rate. It should be noted that the presented results are yet preliminary, in the sense that the CLaMS simulation is based on a rather coarse resolution and not yet optimised (see below). Therefore, differences to observations should not be overrated. The presented CLaMS simulation will be improved in the future, as explained in Sect. 7.3.

7.1 Model configuration

CLaMS simulations based on the total diabatic ERA-Interim transport representation (compare Chapt. 3) were carried out for the period from 1 October 2001 to 31 December 2008. The CLaMS conf guration has a horizontal resolution around the tropical tropopause (380 K) of about 200 km. The vertical resolution at the tropical tropopause is adapted via an aspect ratio $\alpha = 250$ (*Haynes and Anglade*, 1997), expressing the ratio between horizontal and vertical scales, equalling about 800m (compare *Konopka et al.*, 2004, 2007). Starting with the horizontal and vertical resolution at the tropical tropopause, using a mean atmospheric entropy and an idealised static stability prof le, the other vertical layers are def ned such that the entropy per air parcel is constant (*Konopka*, 2010). Chemistry, freeze-drying and mixing, controlled by a critical Lyapunov exponent $\lambda_{\mathrm{Lyap}} = 1.5$, are calculated every 24 hours. The tracers and chemical reactions included in the simulation are summarised in Tab. 7.1.

The focus here is on water vapour, ozone and carbon monoxide, but other species yield rea-

Table 7.1: Species and chemical reactions included in the long-term CLaMS simulation (compare *Pommrich et al.*, 2010a)

$CO + OH$	$\rightarrow$	CO_2 + products	(R1)
$CH_4 + OH$	$\rightarrow$	$2H_2O + CO$	(R2)
$CH_4 + O(^1D)$	$\rightarrow$	$2H_2O + CO$ + products	(R3)
$CH_4 + Cl$	$\rightarrow$	$2H_2O + CO$ + products	(R4)
$N_2O + O(^1D)$	$\rightarrow$	products	(R5)
$N_2O + h\nu$	$\rightarrow$	products	(R6)
$CCl_3F + h\nu$	$\rightarrow$	products	(R7)
$O_2 + h\nu$	$\rightarrow$	$2O_3$	(R8)
$O_3 + OH$	$\rightarrow$	$HO_2 + O_2$	(R9)
$O_3 + HO_2$	$\rightarrow$	$OH + 2O_2$	(R10)

Table 7.2: Boundary values for CLaMS simulated species (lower/upper boundary refer to the bottom/top model layer, unless explicitly stated)

species	lower boundary	upper boundary
H_2O	ECMWF (≤ 340 K)	HALOE
O_3	0	HALOE ($\theta \geq 500$ K)
CO	CMDL (lowest layer – 500 hPa: MOPITT)	MAINZ-2d
CH_4	CMDL	HALOE
N_2O	CMDL	0

sonable results as well (not shown). CLaMS simulated ozone is subject to the same chemistry as in the trajectory reconstruction in Sect. 5.1, namely photochemical production and chemical loss due to HO_x-radicals. The calculation of water vapour is slightly more sophisticated for the full CLaMS simulation (compare *von Hobe et al.*, 2011) than for the backtrajectories. Freeze-drying occurs as soon as relative humidity exceeds a temperature dependent effective 'nucleation barrier' (*Koop et al.*, 2000) and ice sedimentation is controlled by the fall velocity of the ice particles.

At the model boundaries, tracer concentrations are prescribed from observation and model data. The boundary value data is summarised in Tab. 7.2. It should be noted that ozone in the lowest layer is set to zero and above 500 K potential temperature to HALOE climatological values, using the climatology of *Grooß et al.* (2005). Tropospheric water vapour below 340 K is set to ERA-Interim concentrations. The simplif ed chemistry and initialisation for long-term CLaMS simulations, which is adopted here, is discussed in more detail by *Pommrich et al.* (2010a).
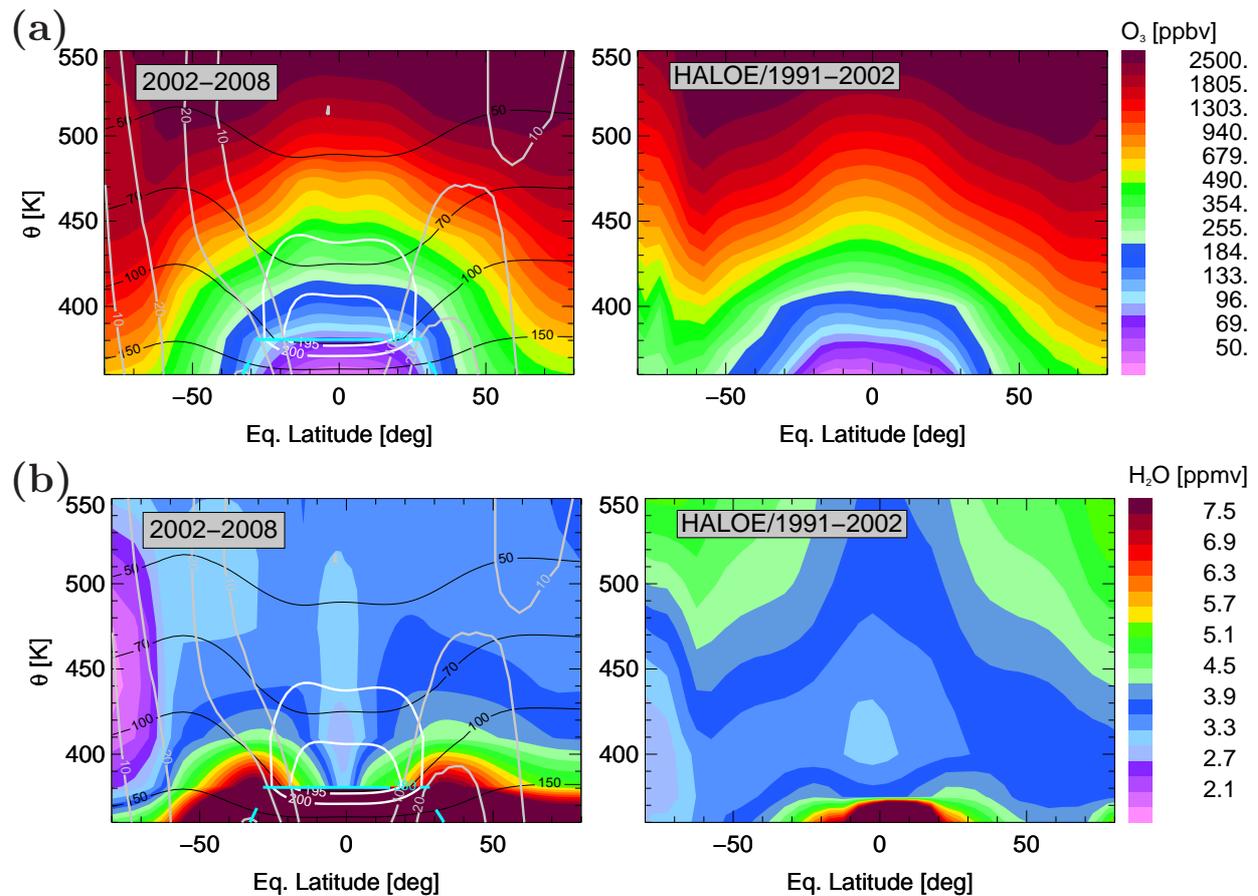
Figure 7.1: Zonal mean climatology of ozone (a) and water vapour (b), from the long-term CLaMS simulation (left), and from HALOE (right). The CLaMS simulation is for the period 2002–2008, the HALOE observations for 1991–2002. In the left panels, thin black lines are isobars, grey lines zonal wind contours and white lines temperature contours. The cyan lines illustrate the tropopause (380 K between $\pm 30°$ latitude and 4 PVU in the extratropics). For CLaMS simulated water vapour, 2 ppmv are subtracted to f t into the range of HALOE observations (see text). Note the non-linear colour code for ozone.

7.2 Comparison between CLaMS simulation and satellite observations

In Fig. 7.1, CLaMS ozone and water vapour are compared to HALOE observations from a climatological zonal mean perspective. The CLaMS species are averaged over the simulation period 2002–2008, HALOE observations over the period 1991–2002.

Simulated ozone, in Fig. 7.1a, agrees reasonable well with HALOE observations, in both absolute values and the pattern of vertical and meridional gradients. The most obvious difference are the too high simulated ozone concentrations in the SH high latitudes. For the long-term simulation a simplif ed ozone chemistry is adopted (compare Tab. 7.1). Polar ozone chemistry is
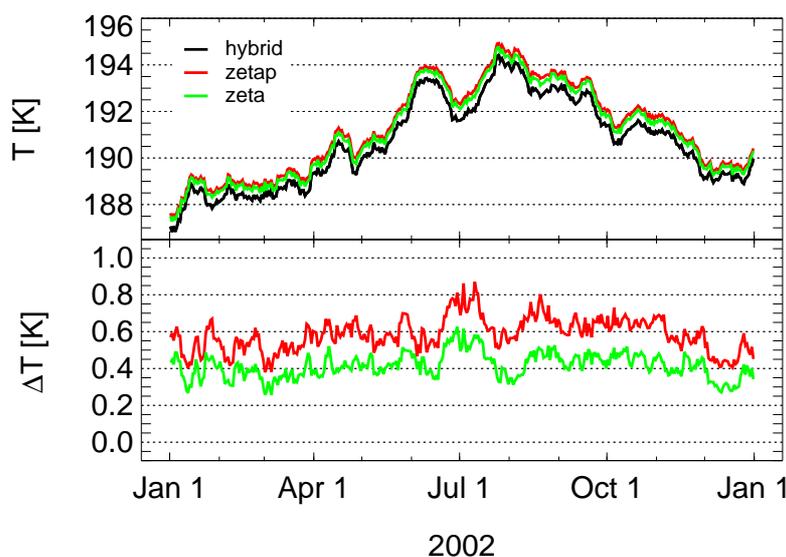
Figure 7.2: (top) Mean tropical cold point temperatures for 2002 (10°S–10°N) from ERA-Interim temperatures on hybrid ECMWF levels (black), and interpolated to isentropic (ζ) levels (green). Temperatures in the former ζ-coordinate system (compare Sect. 3.3.2) are shown for comparison (red). (bottom) As in (top), but for differences between temperatures in isentropic and ECMWF coordinates.

not included and no ozone hole may develop. Therefore, the long-term ozone simulation is only valid in the tropical and mid-latitude stratosphere below 500 K (above HALOE O_3, see Tab. 7.2).

Also, zonal mean simulated water vapour compares reasonable well to HALOE (Fig. 7.1b). At the tropical tropopause and in the SH high latitudes effective freeze-drying to low concentrations occurs, due to extremely low temperatures in these regions. Above the subtropical jets, H_2O concentrations are slightly elevated. However, there is one main discrepancy between the simulation and HALOE. Simulated water vapour concentrations have a signif cant moist bias of about 1–2 ppmv (note the subtraction of 2 ppmv for the displayed CLaMS H_2O in Fig. 7.1b/left).

This moist bias is likely due to the linear temperature interpolation, the coarse time resolution and the coarse spatial resolution of the simulation. First, the linear interpolation of temperature data from hybrid ECMWF model levels to isentropic levels (compare App. A.1) causes a warm bias of temperatures. Figure 7.2/top shows mean tropical cold point temperatures for 2002 (10°S–10°N) for ERA-Interim temperatures on ECMWF levels (black), and interpolated to isentropic (ζ) levels (green). The difference is illustrated in Fig. 7.2/bottom and is about 0.4 K throughout the year (green). The red line denotes temperatures in the earlier ζ-coordinate version (compare Sect. 3.3.2), for which the mean bias was even larger, of about 0.2 K. Second, due to the coarse time resolution the dehydration calculation fails to resolve lower temperatures during the 24 hour time step, amplifying the moist bias of simulated water vapour. Moreover, the horizontal resolution of 200 km (and the corresponding vertical resolution) is rather coarse and together with the mixing parametrization with a critical Lyapunov exponent $\lambda_{\mathrm{Lyap}} = 1.5$

(a)

(b)
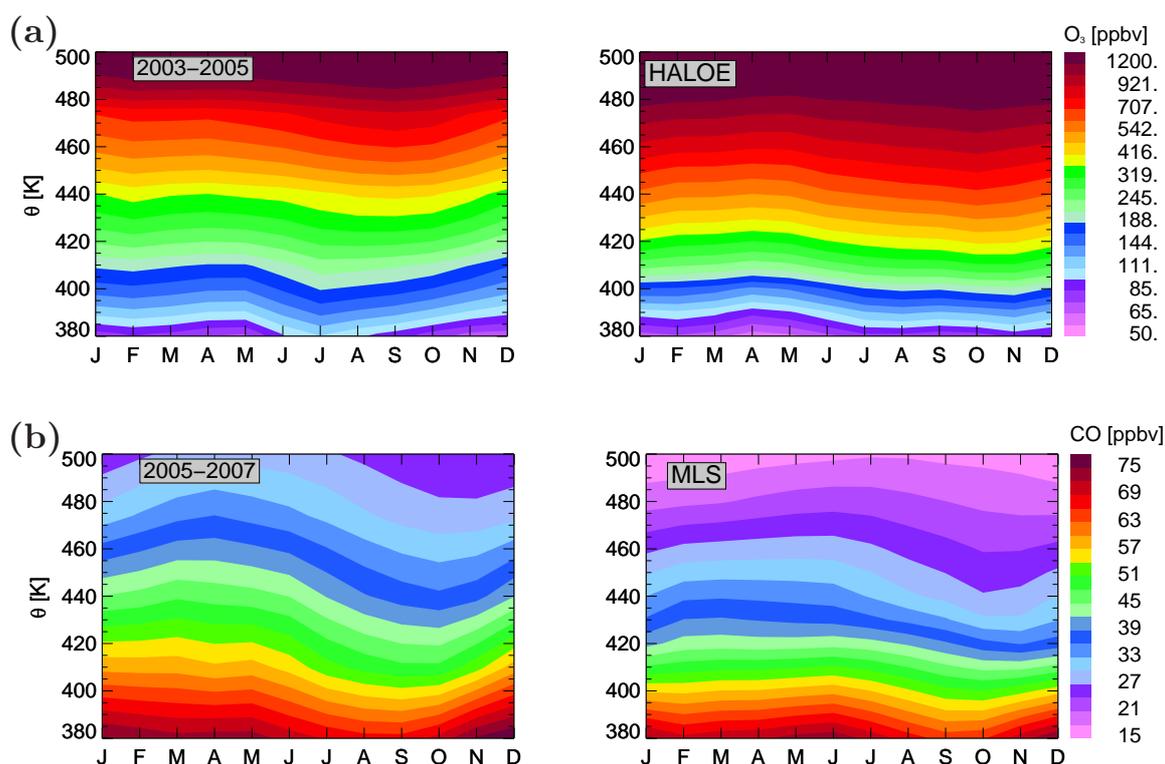
Figure 7.3: Vertical sections in the tropics (20°S–20°N) of climatological ozone (a) and carbon monoxide (b) from the CLaMS simulation (left) and oserved from HALOE (for O_3) and MLS (for CO). The periods for the climatologies are 2003–2005 for O_3 and 2005–2007 for CO.

likely yields excessive numerical diffusion. Reducing mixing by setting the mixing parameter $\lambda_{Lyap} = 3$, reduces diabatic water vapour concentrations in the TTL at 400 K by about 1.5 ppmv (not shown). Therefore, diffusion due to the coarse spatial resolution and the CLaMS mixing parametrization has a noticeable effect on simulated H_2O. It is most likely a combination of all three effects (temperature interpolation, coarse time resolution and coarse spatial resolution), which causes the moist bias in the H_2O simulation.

In Fig. 7.3, the seasonality in the tropics (20°S-20°N) of CLaMS climatological O_3 and CO is compared to HALOE (for O_3) and MLS (for CO) observations. For O_3, the climatology is for the period 2003–2005, for CO for the period 2005–2007, due to the different observational periods of the two satellites. The seasonality of both simulated species agrees well with the observations. For both species the annual cycle in the upper TTL and tropical lower stratosphere is clearly evident, with maximum/minimum concentrations during boreal summer and autumn for O_3/CO. The simulated O_3 maximum and CO minimum occur earlier than observed. Furthermore, the vertical gradients for CLaMS O_3 and CO are too weak. Hence, simulated concentrations for O_3 in the tropical lower stratosphere (400–500 K) are too low compared to HALOE, in agreement with the backtrajectory result in Fig. 5.3. Simulated concentrations for CO are too high.
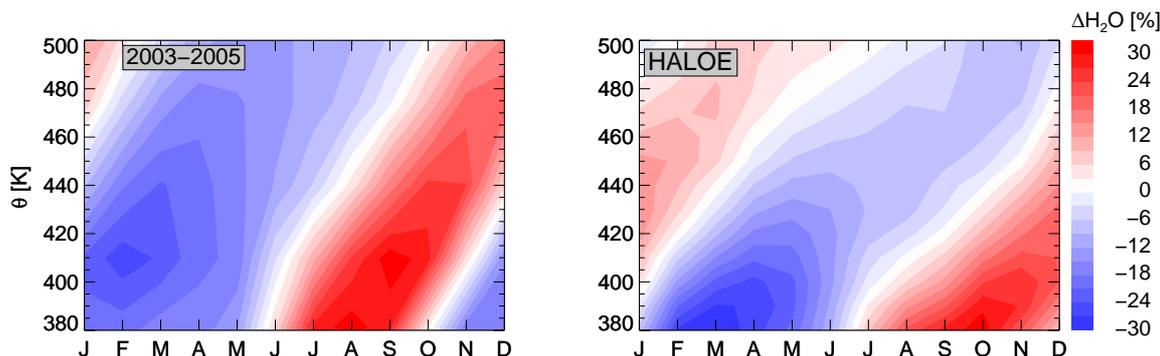
Figure 7.4: Vertical sections in the tropics (20°S–20°N) of the climatological water vapour relative annual anomaly from the CLaMS simulation (left) and observed from HALOE (right), for the period 2003–2005.

Due to the systematic moist bias of simulated water vapour, in Fig. 7.4/left the CLaMS simulated relative annual anomaly in the tropics is shown instead of absolute concentrations, and compared to the HALOE relative anomaly (right). The patterns of both simulated and observed anomalies are similar. However, for the simulated tape recorder the phase attenuation is too weak and in particular the upward phase propagation is too fast.

7.3 Chapter conclusions

The agreement between the diabatic ERA-Interim CLaMS long-term simulation and global observations (HALOE, MLS) is reasonable well. It is expected that the differences between simulation and observations will signif cantly reduce for a future optimised CLaMS simulation, with a f ner spatial resolution (horizontal resolution 100 km) and a shorter dehydration time step.

At this stage, the main improvement of the ERA-Interim based new CLaMS long-term simulation, compared to former simulations, is not better agreement with observations, but a conceptual simplif cation, regarding the vertical transport representation. Due to the use of the total diabatic heating rate for the vertical velocity calculation, no transformation of isentropic vertical velocity into the ω-wind at 100 hPa is necessary to overcome clear-sky diabatic cooling below about 360 K. In the new CLaMS simulation, tropical upward transport from the troposphere into the stratosphere is possible due to the sum of all-sky radiative heating and latent heat release.

However, there seem to be problems inherent in the ERA-Interim data. Too fast upward propagation of H_2O tape recorder phases and too weak O_3 and CO vertical gradients all indicate too strong tropical upwelling in the upper TTL and lower tropical stratosphere. A too strong tropical upwelling in ERA-Interim data is consistent with recent studies proposing a cold bias in tropical tropopause temperatures (*Liu et al.*, 2010) and a cooling effect of assimilation increments (*Fueglistaler et al.*, 2009b). This has to be considered for future transport simulations based on ERA-Interim reanalysis.

8 Summary and conclusions

This thesis presents an analysis of transport in the TTL based on backtrajectories and Lagrangian CTM (CLaMS) simulations. For the backtrajectory approach, a conceptual model was developed to predict water vapour and ozone concentrations in the upper TTL and in the tropical lower stratosphere, on the basis of instantaneous freeze-drying and photochemical ozone production. The backtrajectory prediction yields reasonable well agreement with satellite observed mean TTL concentrations of both water vapour and ozone and even with high-resolution airborne in-situ measurements. The results confirm that tropical water vapour is to first order controlled by freeze-drying and ozone by both photochemical production in slowly rising air masses and transport from the stratosphere.

To study the sensitivity of trajectory and CTM results to the choice of the vertical transport representation, simulations were carried out using different diabatic and kinematic transport representations (based on ECMWF ERA-Interim reanalysis and operational analysis data).

In the first part of the thesis, the focus is on characteristics of transport, in particular timescales and pathways in the TTL. The main results are formulated to answer the following questions:

- *What is the relative importance of the various terms in the diabatic heat budget (e.g., radiation, latent heat release) for tropical troposphere-to-stratosphere transport?*
  In the tropics, clear-sky radiative heating rates are negative below about 360 K (the Level of Zero Radiative Heating LZRH). Radiative effects due to clouds cause additional heating slightly below the clear-sky LZRH, latent heat release causes heating throughout the tropical troposphere. However, for upward transport from the troposphere to the stratosphere in the tropics, neither the heating due to clouds nor due to latent heat release alone is sufficient. Only for the sum of both, the total diabatic heating rate, heating rates are positive throughout the tropics and upward transport is possible.

- *Is there a significant impact of the choice of the transport representation on estimates of transport characteristics (e.g., timescales and pathways) in the TTL?*
  Certain transport characteristics are found to depend very sensitively on the choice of the transport representation, others emerge robustly from all representations. Therefore, transport characteristics are classified into either *sensitive* or *robust*, with respect to the transport representation. Residence time and pathways in the TTL, as well as potential subsidence above the maritime continent and the magnitude of diabatic dispersion (diagnosed from trajectories) are identified as sensitive characteristics. As an example, residence time for

ascent from 340 K to 400 K varies between about one and three months, depending on the choice of the transport representation. In contrast, a strong impact of meridional (quasi-isentropic) in-mixing, a pronounced hemispheric asymmetry of in-mixing (with maximum in-mixing from the summer hemisphere, in particular during boreal summer), the locations of main transport into the TTL and an enhancement of residence times around the LZRH turn out as robust characteristics, independent of the transport representation.

In the second part of the thesis, the focus is on backtrajectory predictions of water vapour and ozone. The following questions lead through the results:

- *Is there a significant impact of the choice of the transport representation on model predictions of water vapour and ozone in the TTL?*
  Similar to the case of transport characteristics (see above), also trace gas species are grouped into sensitive and insensitive with respect to the transport representation. Water vapour turns out as a largely insensitive species. Due to the high degree of temperature control and the weak spatial gradients above the tropopause there is a strong impact of the temperature f eld, relative to transport, on upper TTL water vapour concentrations. Consequently, results concerning mean stratospheric entry water vapour (e.g., *Fueglistaler et al.*, 2005; *Fueglistaler and Haynes*, 2005) are only weakly sensitive to the choice of the transport representation. Ozone concentrations, on the contrary, are highly sensitive to transport uncertainties in the upper TTL and tropical lower stratosphere, due to the rather large spatial, both horizontally and vertically, ozone gradients in this region.

- *What can be learnt from the answers to the previous questions regarding the validation of transport in models?*
  The fact that there are trace gas species which are largely insensitive to transport uncertainties, emphasises the importance to choose suitable tracers for model transport validation. Otherwise, signif cant transport errors are likely to remain undetected. In particular, using only water vapour to validate transport in the TTL and tropical lower stratosphere is insuff cient, as it keeps no memory about transport pathways above the tropopause. Complementary information, for instance from ozone, is needed.

- *What can be learnt regarding the deduction of atmospheric parameters (e.g., mean ascent rates, descent) from ozone profiles?*
  The backtrajectory analysis reveals a large ambiguity between the effects of mean upwelling and dispersion on ozone concentrations in the upper TTL and tropical lower stratosphere. Slower upwelling and larger dispersion both lead to higher ozone concentrations. Therefore, it is not possible to unambiguously estimate any one of the two parameters from ozone alone.

The results of the f rst and the second part of the thesis are combined to assess the last main question:

- *Does diabatic or kinematic transport provide a more realistic view of the atmosphere?*
  The results of this thesis are not without ambiguity regarding the above question. Clearly, a much higher noise and large-scale variability in the kinematic wind f eld, leads to higher trajectory dispersion and higher variation of predicted ozone for kinematic compared to diabatic transport. In the upper TTL and in the tropical lower stratosphere, ozone concentrations are robustly higher for kinematic than for diabatic transport, due to the higher kinematic dispersion. The backtrajectory ozone prediction for the tropical SCOUT-O3 campaign yields an extremely high bias for kinematic ozone compared to observations, arguing against subsidence above the maritime continent as a realistic scenario. From a tropical mean perspective, on the contrary, the kinematic ozone prediction seems more consistent with observations. Trajectory predicted ozone for diabatic transport reveals a slightly low bias.

  However, recent studies suggest that diabatic upwelling for ERA-Interim is too strong, involving an attenuating effect of assimilation increments (*Fueglistaler et al.*, 2009b), a cold bias of tropical tropopause temperatures (*Liu et al.*, 2010) and a corresponding phase shift of the water vapour tape recorder (see Fig. 5.2 and Fig. 7.4). Therefore, the residence time for ozone production in the upper TTL is too short and a slightly low bias of diabatic predicted ozone is expected, and is indeed noticeable in the diabatic prediction. For kinematic transport, the larger dispersion compensates for this low bias. From the tropical large-scale mean perspective this compensation leads to simulated ozone f elds that reasonably agree with observations. But the more localised view of the SCOUT-O3 campaign reveals that the high kinematic dispersion has the potential to cause extremely large errors. Hence, although it is not unambiguously clear whether diabatic or kinematic transport provides a more realistic view of the atmosphere, a diabatic representation seems better suited for transport analyses, as it provides a clearer picture of the underlying processes. For kinematic transport, on the contrary, large dispersion blurs effects of the large-scale circulation, particularly of mean ascent, and renders the interpretation of results more complicated.

Outlook

The presented analysis demonstrates that the uncertainty in the representation of transport in models, here as diabatic versus kinematic transport, may severely affect the model predictions. Different numerics as well as data assimilation are likely to contribute to the differences between diabatic and kinematic transport. But a precise quantif cation of how much of the discrepancy is due to one of these factors, is so far not available. Further progress is anticipated from transport studies using diabatic and kinematic GCM winds, both not inf uenced by the assimilation procedure.

The large sensitivity of certain model results to the choice of the transport representation emphasises the need to better constrain transport in the TTL and in the tropical lower stratosphere.

As long as this goal is not achieved, a deduction of reliable estimates of exact numbers for transport characteristics (e.g., for TTL residence times) from transport models seems not feasible. Only an approximate range of values may be derived.

However, robust transport patterns can be deduced from simulations based on different transport representations. The results of this work show that meridional in-mixing from the extratropical lower stratosphere has a signif cant inf uence on the composition of the TTL irrespective of the choice of the transport representation. Moreover, the strong seasonality of in-mixing, with largest in-mixing from the northern hemisphere during boreal summer, is a robust pattern, largely affecting ozone concentrations in the TTL, in particular their annual variability. Therefore, although exact fractions of in-mixed mid-latitude air in the TTL deduced from trajectory and CTM simulations are sensitive to the choice of the transport representation, the robustness of in-mixing patterns enhances conf dence in a signif cant impact of monsoon circulations on the composition of the TTL.

A Vertical transport in CLaMS

A.1 Hybrid potential temperature coordinate ζ

In analogy to the definition of *Mahowald et al.* (2002), the new hybrid vertical coordinate ζ for CLaMS is defined by

$$\zeta = \theta\, f(\sigma)\,. \tag{A.1}$$

Here, θ is potential temperature and σ an orography following, monotonically decreasing coordinate, defined by $\sigma = p/p_s$, with p pressure and p_s surface pressure, and thus varying between $\sigma = 1$ at the surface and $\sigma = 0$ at the top of the atmosphere (*Phillips*, 1957). The function f is chosen as

$$f(\sigma) = \begin{cases} \sin(\frac{\pi}{2}\frac{1-\sigma}{1-\sigma_r}) & \sigma > \sigma_r \\ 1 & \sigma \le \sigma_r\,, \end{cases} \tag{A.2}$$

and hence hybrid potential temperature ζ exactly equals potential temperature θ above the reference surface σ_r (for $\sigma \le \sigma_r$) and smoothly transforms into σ below. For the CLaMS preprocessor, σ_r has to be defined via $\sigma_r = \frac{p_r}{p_0}$ (with $p_0 = 1000\,\mathrm{hPa}$), by choosing a reference pressure p_r.

Consequently, vertical velocity in ζ coordinates is given by

$$\dot\zeta = f\,\dot\theta + \theta\,(\partial_\sigma f)\dot\sigma\,, \tag{A.3}$$

with

$$\partial_\sigma f = \begin{cases} -\frac{\pi/2}{1-\sigma_r}\cos(\frac{\pi}{2}\frac{1-\sigma}{1-\sigma_r}) & \sigma > \sigma_r \\ 0 & \sigma \le \sigma_r\,. \end{cases} \tag{A.4}$$

The first term on the right-hand side of Eq. A.3 is deduced from diabatic heating rates, as explained in Sect. 3.2.1. Thus, above the reference surface σ_r and therefore throughout the stratosphere, the vertical velocity exactly equals vertical velocity in isentropic coordinates ($\dot\zeta = \dot\theta$) and is determined by diabatic heating rates alone. For the second term, $\dot\sigma$ has to be calculated first via

$$\dot\sigma = \frac{\omega}{p_s} - \frac{p}{p_s^2}\dot p_s\,. \tag{A.5}$$

Pressure tendency ω is provided by analysis and reanalysis data products, surface pressure tendency $\dot p_s$ generally not. Therefore, $\dot p_s$ has to be calculated by vertically integrating the continuity

equation, as explained in *Simmons and Burridge* (1981) and *ECMWF* (2009), and below in App. A.2.

The original ECMWF data is provided on hybrid η levels, with η the ECMWF generalised vertical coordinate (compare *Simmons and Burridge*, 1981). The CLaMS preprocessor f rst calculates σ and $\dot{\sigma}$ on η levels (*grib2ncdf.f90*), second calculates ζ and $\dot{\zeta}$ (*add_theta.f90*) also on η levels, and f nally interpolates to ζ levels (*isentropic.f90*).

A.2 Calculation of the surface pressure tendency

This section summarises the calculation of surface pressure tendency given by *Simmons and Burridge* (1981) and *ECMWF* (2009). The ECMWF η coordinate is def ned in such a way that it assigns two numbers $A_{i+1/2}, B_{i+1/2}$ and $A_{i-1/2}, B_{i-1/2}$ to the upper and lower boundary of each layer i around the ith level. From these coeff cients the mean pressure at level i can be calculated as

$$p_i = \frac{1}{2}\left(p_{i-1/2} + p_{i+1/2}\right). \tag{A.6}$$

For the following calculations, it is useful to def ne $\Delta A_i = A_{i+1/2} - A_{i-1/2} \left(\Delta B_i = B_{i+1/2} - B_{i-1/2}\right)$ as the difference of the $A_i(B_i)$ values at the upper and lower boundary of the ith layer. The continuity equation in η coordinates reads

$$\partial_t(\partial_\eta p) + \nabla^h \cdot (v^h \partial_\eta p) + \partial_\eta(\dot{\eta}\partial_\eta p) = 0, \tag{A.7}$$

with ∇^h the horizontal gradient and $v^h = (u,v)$ the horizontal velocity. Vertical integration of Eq. (A.7) from the surface ($\eta = 1$) to the top of the atmosphere ($\eta = 0$), using the fact that the vertical velocity vanishes at the boundaries ($\dot{\eta}(0) = 0 = \dot{\eta}(1)$), yields an expression for the surface pressure tendency

$$\dot{p}_s = -\int_0^1 \nabla^h \cdot (v^h \partial_\eta p)\, d\eta. \tag{A.8}$$

For N discrete vertical layers Eq. (A.8) reads

$$\dot{p}_s = -\sum_{i=1}^{N} \nabla^h \cdot (v_i^h \Delta p_i), \tag{A.9}$$

with $\Delta p_i = \Delta A_i + p_s \Delta B_i$ the pressure thickness of the ith layer. Using the divergence in spherical coordinates $\nabla^h \cdot x = \frac{1}{a\cos\varphi}(\partial_\lambda x_\lambda + \partial_\varphi(x_\varphi \cos\varphi))$, with λ longitude, φ latitude (here, $x = (x_\lambda, x_\varphi)$ is an arbitrary two dimensional vector), and a redef ned horizontal velocity $\tilde{v}_i \equiv v_i^h \cos\varphi$,

Eq. (A.9) can be written as

$$
\begin{aligned}
\dot{p}_s &= -\frac{1}{a\cos\varphi}\sum_{i=1}^{N}\left[\partial_\lambda(u_i\Delta p_i)+\partial_\varphi(v_i\Delta p_i\cos\varphi)\right]\\
&= -\frac{1}{a\cos^2\varphi}\sum_{i=1}^{N}\left[(\partial_\lambda\tilde{u}_i+\cos\varphi\,\partial_\varphi\tilde{v}_i)\Delta p_i+\tilde{u}_i\partial_\lambda\Delta p_i+\tilde{v}_i\cos\varphi\,\partial_\varphi\Delta p_i\right]\\
&= -\sum_{i=1}^{N}\left[D_i\Delta p_i+\frac{1}{a\cos^2\varphi}(\tilde{u}_i\Delta B_i\partial_\lambda p_s+\tilde{v}_i\cos\varphi\,\Delta B_i\partial_\varphi p_s)\right],
\end{aligned}
$$

with $D_i=\frac{1}{a\cos^2\varphi}(\partial_\lambda\tilde{u}_i+\cos\varphi\,\partial_\varphi\tilde{v}_i)$ the horizontal wind divergence.

Writing the last two terms as a scalar product, using the gradient $\nabla^h=(\frac{1}{a\cos\varphi}\partial_\lambda,\frac{1}{a}\partial_\varphi)$, f nally yields

$$
\dot{p}_s=-\sum_{i=1}^{N}\left[D_i\Delta p_i+(\mathbf{v}^h\cdot\nabla^h p_s)\Delta B_i\right]. \tag{A.10}
$$

The calculation of surface pressure tendency is integrated into the *grib2ncdf.f90* program. The horizontal derivatives ∂_λ, ∂_φ are calculated as centred differences, e.g.,

$$
\partial_\lambda u_i(\lambda_l,\varphi_j)=\frac{1}{2\Delta\lambda}\left[u_i(\lambda_{l+1},\varphi_j)-u_i(\lambda_{l-1},\varphi_j)\right], \tag{A.11}
$$

with $\Delta\lambda=\lambda_{l+1}-\lambda_{l-1}$.

B Effect of production, loss and transport on ozone in the TTL

This appendix provides a brief analysis of the effect of production, loss and transport on back-trajectory predicted ozone in the upper TTL and lower tropical stratosphere. In Fig. B.1a the effect of chemical loss $\Delta O_3(\text{loss})$ is shown for diabatic February/August (black/red) backtrajectory ensembles (see Chapt. 5 for the exact trajectory set-up). 'Chemical loss' here refers to the following loss cycle due to HO_x-radicals (compare reactions (R9/R10) in Tab. 7.1)

$$
\begin{aligned}
O_3 + OH &\longrightarrow HO_2 + O_2 \\
O_3 + HO_2 &\longrightarrow OH + O_2 \\
\hline
2\,O_3 &\longrightarrow 3\,O_2
\end{aligned}
$$
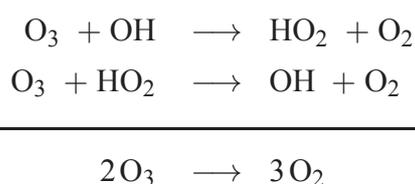
providing the only signif cant loss reaction in the upper TTL and tropical lower stratosphere (see *Osterman et al.*, 1997). Conclusions based on kinematic trajectories are identical.

The effect of chemical loss is calculated from the difference between reconstructed ozone without chemical loss included, and reconstructed ozone (initialisation + production + loss). Figure B.1a shows the frequency of occurrence distribution of chemical loss for the February/August trajectory ensembles (black/red). The distributions for TST trajectories only are shown as grey (February) and red (August) shadings. There is a short tail of the distributions at larger positive values, which is not present in the TST distributions. Thus, chemical loss has a larger effect on in-mixed (stratospheric trajectories) compared to tropical (TST trajectories) air. However, the peaks are narrow and centred near zero, showing that the additional effect of ozone loss reactions is negligible.

The net effect of chemistry $\Delta O_3(\text{chem})$, calculated as frequency of occurrence of the difference between reconstructed ozone and passively transported ozone (initialisation mixing ratios) for the same trajectory ensembles as above, is shown in Fig. B.1b. 'Net chemistry' here refers to photochemical production (compare Eq. (2.2)) and the above HO_x-loss cycle. Obviously, for tropical air (TST) production (net chemistry $\approx$ production, as seen above) strongly modif es the initialisation values, in many cases by more that 50%. For in-mixed air (stratospheric trajectories; difference between lines for all and for TST) production accounts for only a few percent of the f nal mixing ratios, which therefore almost equal the large stratospheric initialisation values.
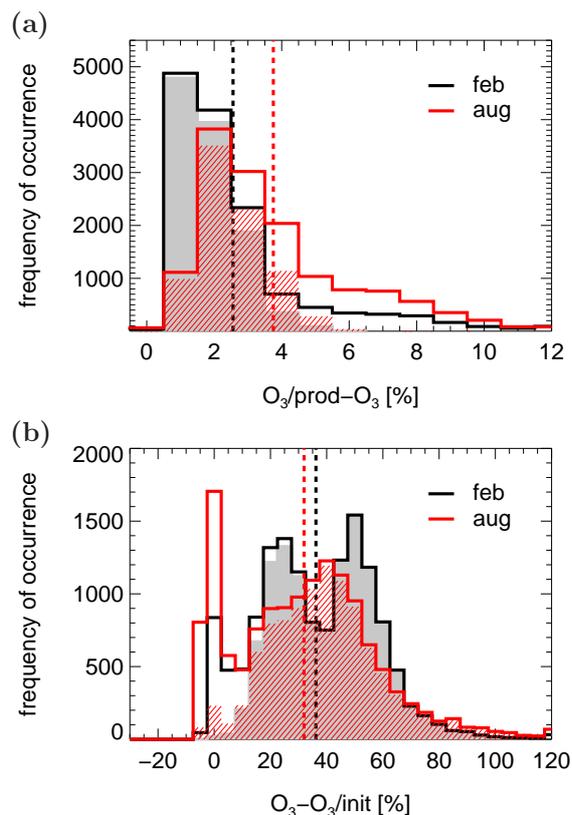
Figure B.1: (a) Effect of chemical ozone loss, calculated from the difference between trajectory reconstructed ozone at 400 K from photolytical production only (O_3/prod) and from both photolytical production and HO_x-loss (top), for February (black) and August (red). Frequency of occurrence for TST trajectories only is shown as grey shaded/red dashed area for February/August. (b) Net effect of chemistry, calculated as difference between trajectory reconstructed and passively transported (initialisation, O_3/init) ozone. The bin size is 1 and 5% in (a) and (b), respectively. Black/red dashed lines show the means of the distributions. (Figure adapted from *Ploeger et al.*, 2011).

To summarise, the effect of chemical loss in the upper TTL and tropical lower stratosphere is negligible. Photochemical production and transport both contribute signif cantly to ozone concentrations.

Symbols and abbreviations

Symbol	Description	unit, value
x	3d position vector	°E/N, K
λ	longitude	°E
φ	latitude	°N
θ	potential temperature	K
p	pressure	hPa
σ	orography following vertical coordinate	
ζ	hybrid potential temperature coordinate	K
η	ECMWF hybrid vertical coordinate	
v	3d wind	$m \cdot s^{-1}, K \cdot d^{-1}$
u	zonal wind	$m \cdot s^{-1}$
v	meridional wind	$m \cdot s^{-1}$
$\dot{\theta}$	vertical velocity in isentropic coordinates	$K \cdot d^{-1}$
ω	vertical velocity in isobaric coordinates	$Pa \cdot s^{-1}$
$\dot{\zeta}$	vertical velocity in ζ coordinates	$K \cdot d^{-1}$
p_s	surface pressure	hPa
ω_s	isobaric surface vertical velocity	$Pa \cdot s^{-1}$
T	temperature	K
Q	diabatic heating term	$K \cdot d^{-1}$
J	diabatic heating rate per unit mass	$K \cdot (kg \cdot d)^{-1}$
c_p	specif c heat at constant pressure	$J \cdot K^{-1} \cdot mol^{-1}$
μ	mixing ratio	
S	net chemical source term	
$\langle \theta^2 \rangle$	potential temperature variance (vert. dispersion)	K^2
λ_{Lyap}	Lyapunov exponent	
f	trajectory fraction	
v^h	2d horizontal wind vector	$m \cdot s^{-1}$
∇^h	horizontal gradient	

Acronym	Description
AMMA	African monsoon multidisciplinary analysis
CCM	Chemistry climate model
CLaMS	Chemical Lagrangian model of the stratosphere
CMDL	Climate monitoring & diagnostics laboratory
CTM	Chemistry transport model
djf	boreal winter (December, January, February)
ECMWF	European centre for medium-range weather forecasts
FISH	Fast in-situ stratospheric hygrometer
FOZAN	Fast-response chemiluminescent airborne ozone analyzer
HALOE	Halogen Occultation Experiment
jja	boreal summer (June, July, August)
LZRH	Level of zero radiative heating
MLS	Microwave limb sounder
MOPITT	Measurements of pollution in the troposphere
NH	Northern hemisphere
PDF	Probability density function
ppmv	parts per million by volume
ppbv	parts per billion by volume
SCOUT-O3	Stratospheric-climate links with emphasis on the upper troposphere and lower stratosphere
SH	Southern hemisphere
SHADOZ	Southern hemisphere additional ozonesonde network
TST	Troposphere-to-stratosphere transport
TTL	Tropical tropopause layer
UTC	Universal time coordinated
VSLS	Very short-lived substances

List of Figures

List of Tables

Bibliography

Andrews, D. G., J. R. Holton, and C. B. Leovy (1987), *Middle Atmosphere Dynamics*, Academic Press, San Diego, USA.

Avallone, L. M., and M. J. Prather (1996), Photochemical evolution of ozone in the lower tropical stratosphere, *J. Geophys. Res.*, *101*(D1), 1457–1461.

Becker, G., J.-U. Grooß, D. S. McKenna, and R. Müller (2000), Stratospheric photolysis frequencies: Impact of an improved numerical solution of the radiative transfer equation, *J. Atmos. Chem.*, *37*, 217–229, doi:10.1023/A:1006468926530.

Bonazzola, M., and P. H. Haynes (2004), A trajectory-based study of the tropical tropopause region, *J. Geophys. Res.*, *109*(D20), 20112, doi:10.1029/2003JD004356.

Brewer, A. W. (1949), Evidence for a world circulation provided by the measurements of helium and water vapour distribution in the stratosphere, *Q. J. R. Meteorol. Soc.*, *75*, 351–363.

Brunner, D., et al. (2009), The SCOUT-O3 Darwin aircraft campaign: rationale and meteorology, *Atmos. Chem. Phys.*, *9*, 93–117.

Butchart, N., et al. (2006), Simulations of anthropogenic change in the strength of the Brewer-Dobson circulation, *Clim. Dyn.*, *27*, 727–741.

Carver, G. D., P. D. Brown, and O. Wild (1997), The ASAD atmospheric chemistry integration package and chemical reaction database, *Computer Physics Communications*, *105*, 197–215.

Chen, P. (1995), Isentropic cross-tropopause mass exchange in the extratropics, *J. Geophys. Res.*, *100*, 16,661–16,673.

Corti, F., B. P. Luo, Q. Fu, H. Vömel, and T. Peter (2006), The impact of cirrus clouds on tropical troposphere-to-stratosphere transport, *Atmos. Chem. Phys.*, *6*, 1725–1747.

Corti, T., et al. (2008), Unprecedented evidence for deep convection hydrating the tropical stratosphere, *Geophys. Res. Lett.*, *35*, L10810, doi:10.1029/2008GL033641.

Danielsen, E. F. (1982), A dehydration mechanism for the stratosphere, *Geophys. Res. Lett.*, *9*, 605–608.

96   **Bibliography**

Dessler, A. E. (2000), *The chemistry and physics of stratospheric ozone*, *International Geophysics Series*, vol. 74, Academic Press, London, San Diego.

Dethof, A., A. O'Neill, J. M. Slingo, and H. G. J. Smit (1999), A mechanism for moistening the lower stratosphere involving the Asian summer monsoon, *Q. J. R. Meteorol. Soc.*, *125*, 1079–1106.

Dobson, G. M. B., A. W. Brewer, and B. M. Cwilong (1946), Meteorology of the lower stratosphere, *Proc. R. Soc. London A*, *185*, 144–175.

Dunkerton, T. J. (1995), Evidence of meridional motion in the summer lower stratosphere adjacent to monsoon regions, *J. Geophys. Res.*, *100*(D8), 16,675–16,688.

ECMWF (2009), *IFS Documentation Cy33r1*, European Centre for Medium-Range Weather Forecasts ECMWF, www.ecmwf.int/research/ifsdocs/CY33r1/DYNAMICS/.

Engel, A., et al. (2008), Age of stratospheric air unchanged within uncertainties over the past 30 years, *Nature*, *2*, 28–31, doi:10.1038/NGEO388.

Folkins, I., M. Loewenstein, J. Podolske, S. J. Oltmans, and M. Proff tt (1999), A barrier to vertical mixing at 14 km in the tropics: Evidence from ozonesondes and aircraft measurements, *J. Geophys. Res.*, *104*, 22,095–22,102.

Folkins, I., P. Bernath, C. Boone, G. Lesins, N. Livesey, A. M. Thompson, K. Walter, and J. C. Witte (2006), Seasonal cycles of O_3, CO, and convective outf ow at the tropical tropopause, *Geophys. Res. Lett.*, *33*, L16802, doi:10.1029/2006GL026602.

Fueglistaler, S., and Q. Fu (2006), Impact of clouds on radiative heating rates in the tropical lower stratosphere, *J. Geophys. Res.*, *111*(D23), D23202, doi:10.1029/2006JD007273.

Fueglistaler, S., and P. H. Haynes (2005), Control of interannual and longer-term variability of stratospheric water vapor, *J. Geophys. Res.*, *110*(D24), D24108, doi:10.1029/2005JD006019.

Fueglistaler, S., H. Wernli, and T. Peter (2004), Tropical troposphere-to-stratosphere transport inferred from trajectory calculations, *J. Geophys. Res.*, *109*(D3), D03108, doi:10.1029/2003JD004069.

Fueglistaler, S., S. Bonazzola, P. H. Haynes, and T. Peter (2005), Stratospheric water vapor predicted from the Lagrangian temperature history of air entering the stratosphere in the tropics, *J. Geophys. Res.*, *110*(D8), D08107, doi:10.1029/2004JD005516.
"
Hwgi rkuvcrgt. "U0 "C0 'G0 F guungt. "V0 L0 F wpmgtvqp. "K0 Hqmkpu. "S 0 'Hw. "cpf "R0 Y 0 O qvg "*422; c+.
""" "Vtqr kecn\tqr qr cwug "nc{gt. "T gx0 I gqr j {u0 "69. "TI 3226. "f qk<320 B24; 422: TI 2224890

Fueglistaler, S., B. Legras, A. Beljaars, J. J. Morcrette, A. Simmons, A. M. Tompkins, and S. Uppala (2009b), The diabatic heat budget of the upper troposphere and lower/mid stratosphere in ECMWF reanalysis, *Q. J. R. Meteorol. Soc.*, *135*, 638, doi:10.1002/qj.361.

Gettelman, A., and P. M. Forster (2002), Def nition and climatology of the tropical tropopause layer, *jmsj*, *80*(4B), 911–924.

Gettelman, A., P. M. de F. Forster, M. Fujiwara, Q. Fu, H. Vömel, L. K. Gohar, C. Johanson, and M. Ammerman (2004a), Radiation balance of the tropical tropopause layer, *J. Geophys. Res.*, *109*(D7), D07103, doi:10.1029/2003JD004190.

Gettelman, A., D. E. Kinnison, and T. J. Dunkerton (2004b), Impact of monsoon circulations on the upper troposphere and lower stratosphere, *J. Geophys. Res.*, *109*(D22), D22101, doi: 10.1029/2004JD004878.

Gettelman, A., et al. (2009), The tropical tropopause layer 1960-2100, *Atmos. Chem. Phys.*, *9*, 1621–1637.

Gill, A. E. (1980), Some simple solutions for heat-induced tropical circulation, *qjrms*, *106*, 447–462.

Grooß, J.-U., and J. M. Russell (2005), Technical note: A stratospheric climatology for O_3, H_2O, CH_4, NO_x, HCl and HF derived from HALOE measurements, *Atmos. Chem. Phys.*, *5*, 2797–2807.

Grooß, J.-U., P. Konopka, and R. Müller (2005), Ozone chemistry during the 2002 Antarctic vortex split, *J. Atmos. Sci.*, *62*, 860–870.

Hall, T. M., and R. A. Plumb (1994), Age as a diagnostic of stratospheric transport, *J. Geophys. Res.*, *99*(D1), 1059–1070.

Hatsushika, H., and K. Yamazaki (2003), Stratospheric drain over Indonesia and dehydration within the tropical tropopause layer diagnosed by air parcel trajectories, *J. Geophys. Res.*, *108*(D19), 4610, doi:10.1029/2002JD002986.

Haynes, P., and J. Anglade (1997), The vertical scale cascade in atmospheric tracers due to large-scale differential advection, *J. Atmos. Sci.*, *54*, 1121–1136.

Haynes, P., and E. Shuckburgh (2000), Effective diffusivity as a diagnostic of atmospheric transport 2. Troposphere and lower stratosphere, *J. Geophys. Res.*, *105*(D18), 22,795–22,810.

Haynes, P., C. J. Marks, M. E. McIntyre, T. G. Shepherd, and K. P. Shine (1991), On the downward control of extratropical diabatic circulations by eddy-induced mean zonal forces, *J. Atmos. Sci.*, *48*, 651–679.

Highwood, E. J., and B. J. Hoskins (1998), The tropical tropopause, *Q. J. R. Meteorol. Soc.*, *124*, 1579 – 1604.

Holton, J. R. (1992), *An Introduction to Dynamic Meteorology*, Academic Press, London.

Holton, J. R., and A. Gettelman (2001), Horizontal transport and the dehydration of the stratosphere, *Geophys. Res. Lett.*, *28*(14), 2799–2802.

Holton, J. R., P. Haynes, M. E. McIntyre, A. R. Douglass, R. B. Rood, and L. Pf ster (1995), Stratosphere-troposphere exchange, *Rev. Geophys.*, *33*, 403–439.

James, R., M. Bonazzola, B. Legras, K. Surbled, and S. Fueglistaler (2008), Water vapor transport and dehydration above convective outf ow during Asian monsoon, *Geophys. Res. Lett.*, *35*, L20810, doi:10.1029/2008GL035441.

John, F. (1987), *Partial Differential Equations*, Springer-Verlag, New York, USA.

Kasahara, A. (1974), Various vertical coordinate systems used for numerical weather prediction, *Mon. Wea. Rev.*, *102*, 509–522.

Konopka, P. (2010), Lagrangian simulation of trace gas distributions, in preparation.

Konopka, P., J.-U. Grooß, F. Ploeger, and R. Müller (2009), Annual cycle of horizontal in-mixing into the lower tropical stratosphere, *J. Geophys. Res.*, *114*, D19111, doi:10.1029/2009JD011955.

Konopka, P., J. U. Grooß, G. Günther, F. Ploeger, R. Pommrich, R. Müller, and N. Livesey (2010), Annual cycle of ozone at and above the tropical tropopause: observations versus simulations with the Chemical Lagrangian Model of the Stratosphere (CLaMS), *Atmos. Chem. Phys.*, *10*, 121–132.

Konopka, P., et al. (2004), Mixing and ozone loss in the 1999-2000 Arctic vortex: Simulations with the 3-dimensional Chemical Lagrangian Model of the Stratosphere (CLaMS), *J. Geophys. Res.*, *109*, D02315, doi:10.1029/2003JD003792.

Konopka, P., et al. (2007), Contribution of mixing to upward transport across the tropical tropopause layer (TTL), *Atmos. Chem. Phys.*, *7*, 3285–3308.

Koop, T., B. P. Luo, A. Tsias, and T. Peter (2000), Water activity as the determinant for homogeneous ice nucleation in aqueous solutions, *Nature*, *406*, 611–614.

Krämer, M., et al. (2009), Ice supersaturations and cirrus cloud crystal numbers, *Atmos. Chem. Phys.*, *9*, 35053522.

Kremser, S., I. Wohltmann, M. Rex, U. Langematz, M. Dameris, and M. Kunze (2009), Water vapour transport in the tropical tropopause region in coupled Chemistry-Climate Models and ERA-40 reanalysis data, *Atmos. Chem. Phys.*, *9*, 2679–2694.

Krüger, K., S. Tegtmeier, and M. Rex (2008), Long-term climatology of air mass transport through the tropical tropopause layer (TTL) during NH winter, *Atmos. Chem. Phys.*, *8*, 813–823.

Krüger, K., S. Tegtmeier, and M. Rex (2009), Variability of residence time in the tropical tropopause layer during northern hemisphere winter, *Atmos. Chem. Phys.*, *9*, 12,597–12,614.

Levine, J. G., P. Braesicke, N. R. P. Harris, N. S. Savage, and J. A. Pyle (2007), Pathways and timescales for troposphere-to-stratosphere transport via the tropical tropopause layer and their relevance for very short-lived substances, *J. Geophys. Res.*, *112*(D4), D04308, doi:10.1029/2005JD006940.

Levine, J. G., P. Braesicke, N. R. P. Harris, and J. A. Pyle (2008), Seasonal and inter-annual variations in troposphere-to-stratosphere transport from the tropical tropopause layer, *Atmos. Chem. Phys.*, *8*, 3689–3703.

Liu, S., S. Fueglistaler, and P. Haynes (2010), *J. Geophys. Res.*, *in press*, doi:10.1029/2010JD014352.

Mahowald, N. M., R. A. Plumb, P. J. Rasch, J. del Corral, and F. Sassi (2002), Stratospheric transport in a three-dimensional isentropic coordinate model, *J. Geophys. Res.*, *107*(D15), 4254, doi:10.1029/2001JD001313.

Marcy, T. P., et al. (2007), Measurements of trace gases in the tropical tropopause layer, *Atmos. Environ.*, *41*(34), 7253–7261, doi:10.1016/j.atmosenv.2007.05.032.

McKenna, D. S., J.-U. Grooß, G. Günther, P. Konopka, R. Müller, G. Carver, and Y. Sasano (2002a), A new Chemical Lagrangian Model of the Stratosphere (CLaMS): 2. Formulation of chemistry scheme and initialization, *J. Geophys. Res.*, *107*(D15), 4256, doi:10.1029/2000JD000113.

McKenna, D. S., P. Konopka, J.-U. Grooß, G. Günther, R. Müller, R. Spang, D. Offermann, and Y. Orsolini (2002b), A new Chemical Lagrangian Model of the Stratosphere (CLaMS): 1. Formulation of advection and mixing, *J. Geophys. Res.*, *107*(D16), 4309, doi:10.1029/2000JD000114.

Meier, R. R., J. Anderson, D. E., and M. Nicolet (1982), Radiation Field in the Troposphere and Stratosphere from 240-1000 nm -I: General Analysis, *Planet Space Sci*, *30*, 923–933.

Monge-Sanz, B. M., M. P. Chipperfeld, A. J. Simmons, and S. M. Uppala (2007), Mean age of air and transport in a CTM: Comparison of different ECMWF analyses, *Geophys. Res. Lett.*, *34*, L04801, doi:10.1029/2006GL028515.

Morcrette, J.-J. (1991), Radiation and cloud radiative properties in the European Centre for Medium-Range Weather Forecasts forecasting system, *J. Geophys. Res.*, *96*(D5), 9121–9132.

Mote, P. W., K. H. Rosenlof, J. R. Holton, R. S. Harwood, and J. W. Waters (1995), Seasonal variations of water vapor in the tropical lower stratosphere, *Geophys. Res. Lett.*, *22*, 1093–1096, doi:10.1029/95GL01234. 7,

Mote, P. W., T. J. Dunkerton, M. E. McIntyre, E. A. Ray, P. H. Haynes, and J. M. Russell III (1998), Vertical velocity, vertical diffusion, and dilution by midlatitude air in the tropical lower stratosphere, *J. Geophys. Res.*, *103*, 8651 – 8666.

Mote, P. W., et al. (1996), An atmospheric tape recorder: The imprint of tropical tropopause temperatures on stratospheric water vapor, *J. Geophys. Res.*, *101*(D2), 3989 – 4006.

Nash, E. R., P. A. Newman, J. E. Rosenfeld, and M. R. Schoeberl (1996), An objective determination of the polar vortex using Ertel's potential vorticity, *J. Geophys. Res.*, *101*, 9471–9478.

Newell, R. E., and S. Gould-Stewart (1981), A stratopheric fountain ?, *J. Atmos. Sci.*, *38*, 2789 – 2796.

Osterman, G. B., R. J. Salawitch, B. Sen, G. C. Toon, R. A. Stachnik, H. M. Pickett, J. J. Margitan, and D. B. Peterson (1997), Balloon-borne measurements of stratospheric radicals and their precursors: Implications for the production and loss of ozone, *Geophys. Res. Lett.*, *24*, 1107–1110, doi:10.1029/97GL00921.

Pan, L. L., P. Konopka, and E. V. Browell (2006), Observations and model simulations of mixing near the extratropical tropopause, *J. Geophys. Res.*, *111*(D5), D05106, doi:10.1029/2005JD006480.

Park, M., W. J. Randel, A. Gettelman, S. T. Massie, and J. H. Jiang (2006), Transport above the Asian summer monsoon anticyclone inferred from Aura Microwave Limb Sounder tracers, *J. Geophys. Res.*, *112*, D16309, doi:10.1029/2006JD008294.

Park, M., W. J. Randel, L. K. Emmons, P. F. Bernath, K. A. Walker, and C. D. Boone (2008), Chemical isolation in the Asian monsoon anticyclone observed in Atmospheric Chemistry Experiment (ACE-FTS) data, *Atmos. Chem. Phys.*, *8*, 757–764.

Phillips, N. A. (1957), A coordinate system having some special advantages for numerical forecasting, *J. Meteor.*, *14*, 184–185, doi:10.1029/93GL03020.

Ploeger, F., P. Konopka, G. Günther, J.-U. Grooß, and R. Müller (2010), Impact of the vertical velocity scheme on modeling transport in the tropical tropopause layer, *J. Geophys. Res.*, *115*, D03301, doi:10.1029/2009JD012023.

Ploeger, F., et al. (2011), Insight from ozone and water vapour on transport in the tropical tropopause layer (TTL), *Atmos. Chem. Phys.*, *11*, 407–419.

Plumb, R. A. (1996), A "tropical pipe" model of stratospheric transport, *J. Geophys. Res.*, *101*, 3957–3972.

Pommrich, R., R. Müller, J. U. Grooß, P. Konopka, G. Günther, H.-C. Pumphrey, S. Viciani, L. Emmons, and M. Riese (2010a), Carbon monoxide as a tracer for tropical troposphere-to-stratosphere transport in the Chemical Lagrangian Model of the Stratosphere (CLaMS), *Geosci. Model Dev.*, in preparation.

Pommrich, R., et al. (2010b), What causes the irregular cycle of the atmospheric tape recorder signal in HCN?, *Geophys. Res. Lett.*, *37*, L16805, doi:10.1029/2010GL044056.

Preparata, F. P., and M. Shamos (1985), *Computational Geometry. An Introduction*, Springer-Verlag.

Pumphrey, H. C., C. Boone, K. A. Walker, P. Bernath, and N. J. Livesey (2008), Tropical tape recorder observed in HCN, *Geophys. Res. Lett.*, *35*, L05801, doi:10.1029/2007GL032137.

Randel, W. J., and M. Park (2006), Deep convective infuence on the Asian summer monsoon anticyclone and associated tracer variability observed with Atmospheric Infrared Sounder (AIRS), *J. Geophys. Res.*, *111*, D12314, doi:10.1029/2005JD006490.

Randel, W. J., F. Wu, S. J. Oltmans, K. Rosenlof, and G. E. Nedoluha (2004), Interannual changes of stratospheric water vapor and correlations with tropical tropopause temperatures, *J. Atmos. Sci.*, *61*, 2133–2148.

Randel, W. J., F. Wu, H. Vömel, G. E. Nedoluha, and P. Forster (2006), Decreases in stratospheric water vapor after 2001: Links to changes in the tropical tropopause and the Brewer-Dobson circulation, *J. Geophys. Res.*, *111*(D12), D12312, doi:10.1029/2005JD006744.

Randel, W. J., M. Park, F. Wu, and N. Livesey (2007), A large annual cycle in ozone above the tropical tropopause linked to the Brewer-Dobson circulation, *J. Atmos. Sci.*, *64*, 4479–4488.

Randel, W. J., M. Park, L. Emmons, D. Kinnison, P. Bernath, K. A. Walker, C. Boone, and H. Pumphrey (2010), Asian monsoon transport of pollution to the stratosphere, *Science*, *328*(5978), 611–613, doi:10.1126/science.1182274.

Ricaud, P., et al. (2007), Impact of land convection on troposphere-stratosphere exchange in the tropics, *Atmos. Chem. Phys.*, *7*, 5639–5657.

Russell, J. M., L. L. Gordley, J. H. Park, S. R. Drayson, A. F. Tuck, J. E. Harries, R. J. Cicerone, P. J. Crutzen, and J. E. Frederick (1993), The Halogen Occultation Experiment, *J. Geophys. Res.*, *98*, 10,777–10,797.

Salby, M. L. (1996), *Fundamentals of atmospheric physics*, Academic Press, San Diego.

Schiller, C., J.-U. Grooß, P. Konopka, F. Ploeger, F. H. S. dos Santos, and N. Spelten (2009), Hydration and dehydration at the tropical tropopause, *Atmos. Chem. Phys.*, *9*, 9647–9660.

Schoeberl, M. R., A. R. Douglass, Z. X. Zhu, and S. Pawson (2003), A comparison of the lower stratospheric age spectra derived from a general circulation model and two data assimilation systems, *J. Geophys. Res.*, *108*(D3), 4113, doi:10.1029/2002JD002652.

Schoeberl, M. R., B. Duncan, A. R. Douglass, J. Waters, N. J. Livesey, W. Read, and M. Filipiak (2006), The carbon monoxide tape recorder, *Geophys. Res. Lett.*, *33*, L12811, doi:10.1029/2006GL026178.

Schoeberl, M. R., et al. (2008), QBO and annual cycle variations in tropical lower stratosphere trace gases from HALOE and Aura MLS observations, *J. Geophys. Res.*, *113*(D5), D05301, doi:10.1029/2007JD008678.

Seidel, D. J., Q. Fu, W. J. Randel, and T. J. Reichler (2008), Widening of the tropical belt in a changing climate, *Nature*, *1*, 21–24, doi:10.1038/ngeo.2007.38.

Sherwood, S. C. (2000), A stratospheric 'drain' over the maritime continent, *Geophys. Res. Lett.*, *27*(5), 677–680.

Simmons, A., S. Uppala, S. Dee, and S. Kobayashi (2006), ERA-Interim: New ECMWF reanalysis products from 1989 onwards, *ECMWF Newsletter*, *110*, 25–35.

Simmons, A. J., and D. M. Burridge (1981), An energy and angular-momentum conserving vertical f nite-difference scheme and hybrid vertical coordinates, *Month. Weather Rev.*, *109*, 758–766.

Simmons, A. J., A. Untch, C. Jakob, P. Kållberg, and P. Unden (1999), Stratospheric water vapour and tropical tropopause temperatures in ECMWF analyses and multi-year simulations, *Q. J. R. Meteorol. Soc.*, *125*, 353 – 386.

Sparling, L. C., J. A. Kettleborough, P. H. Haynes, M. E. McIntyre, J. E. Rosenf eld, M. R. Schoeberl, and P. A. Newman (1997), Diabatic cross-isentropic dispersion in the lower stratosphere, *J. Geophys. Res.*, *102*(D22), 25,817–25,829.

Thompson, A., J. C. Witte, C. Jacquelyn, H. G. J. Smit, S. J. Oltmans, B. J. Johnson, V. W. J. H. Kirchhoff, and F. J. Schmidlin (2007), Southern hemisphere additional ozonesondes (SHADOZ) 1998-2004 tropical ozone climatology: 3. instrumentation, station-to-station variability, and evaluation with simulated f ight prof les, *J. Geophys. Res.*, *112*(D3), 3304, doi: 10.1029/2005JD007042.

Thompson, A. M., et al. (2003), Southern hemisphere additional ozonesondes (SHADOZ) 1998-2000 tropical ozone climatology - 2. tropospheric variability and the zonal wave-one, *J. Geophys. Res.*, *108*(D2), doi:10.1029/2002JD002241.

Tompkins, A. M., K. Gierens, and G. Rädel (2007), Ice supersaturation in the ECMWF integrated forecast system, *Q. J. R. Meteorol. Soc.*, *133*, 53–63, doi:10.1002/qj.14.

Tuck, A. F., et al. (1997), The Brewer-Dobson circulation in the light of high altitude in situ aircraft observation, *Q. J. R. Meteorol. Soc.*, *123*, 1–69.

Ulanosvky, A. E., V. A. Yushkov, N. M. Sitnikov, and F. Ravegnani (2001), The FOZAN-II fast-response chemiluminescent airborne ozone analyzer, *Instrum. Exp. Tech.*, *44*, 249–256.

Uppala, S., S. Dee, S. Kobayashi, P. Berrisford, and A. Simmons (2008), Towards a climate data assimilation system: status update of ERA-Interim, *ECMWF Newsletter*, *115*, 12–18.

Uppala, S. M., et al. (2005), The ERA-40 re-analysis, *Q. J. R. Meteorol. Soc.*, *131*, 2961–3012, doi:10.1256/qj.04.176.

Volk, C. M., et al. (1996), Quantifying transport between the tropical and mid-latitude lower stratosphere, *Science*, *272*, 1763–1768.

von Hobe, M., J.-U. Grooß, G. Günther, and et. al. (2011), Evidence for heterogeneous chlorine activation in the tropical UTLS, *11*, 241–256.

Wang, B. (2006), *The Asian monsoon*, Springer, Heidelberg, Germany.

Waugh, D. W., and T. M. Hall (2002), Age of stratospheric air: Theory, observations, and models, *Rev. Geophys.*, *40*(4), 1–27.

Webster, P. J., V. O. Magana, T. N. Palmer, J. Shukla, R. A. Tomas, M. Yanai, and T. Yasunari (1998), Monsoons: Processes, predictability, and the prospects for prediction, *J. Geophys. Res.*, *103*, 14,451–14,510.

Wohltmann, I., and M. Rex (2008), Improvement of vertical and residual velocities in pressure or hybrid sigma-pressure coordinates in analysis data in the stratosphere, *Atmos. Chem. Phys.*, *8*, 265–272.

Yulaeva, E., J. R. Holton, and J. M. Wallace (1994), On the cause of the annual cycle in tropical lower-stratospheric temperatures, *J. Atmos. Sci.*, *51*, 169–174.

Zöger, M., C. Schiller, and N. Eicke (1999), Fast in situ hygrometers: A new family of balloon-borne and airborne Lyman-α photofragment f uorescence hygrometers, *J. Geophys. Res.*, *104*, 1807 – 1816.

Acknowledgements